ABSTRACT

Title of Thesis: COMPUTATIONAL AEROACOUSTICS OF VARIOUS PROPELLER DESIGNS FOR eVTOL APPLICATIONS

Bernadine Passe
Master of Science in Aerospace Engineering, 2019

Thesis Directed by: Professor James Baeder
A. James Clark School of Engineering
Department of Aerospace Engineering

An in-house CFD solver, GPU-Accelerated Rotorcraft Flow-Field (GARFIELD), was coupled to an acoustic code for a computational aeroacoustic framework to analyze low aspect ratio propellers in hover such as those found on typical eVTOL aircraft. Various design parameters including twist, planform, number of blades, RPM, sweep, and disk loading were varied to evaluate their effect on aerodynamic performance as well as the overall average sound pressure level (OASPL) experienced by an observer. A nearby boom geometry was added to investigate the impact of the unsteady airloads on the aeroacoustic performance. Aerodynamic loads were also calculated by a BEMT analysis for comparison to the results predicted by CFD in GARFIELD. The main drivers to reduce the OASPL were found to be RPM and blade count. It was found that the boom geometry and all other design parameters for the propellers did not have a significant impact on the aeroacoustic performance.

COMPUTATIONAL AEROACOUSTICS OF VARIOUS PROPELLER DESIGNS FOR EVTOL APPLICATIONS

by

Bernadine Passe

Thesis submitted to the Faculty of the Graduate School of the
University of Maryland, College Park in partial fulfillment
of the requirements for the degree of
Master of Science
2019

Advisory Committee:
Dr. James Baeder, Chair/Advisor
Dr. Roberto Celi
Dr. Anubhav Datta

Acknowledgments

First and foremost I would like to thank my advisor, Dr. James Baeder for giving me the incredible opportunity to work on a challenging and interesting project over the past two years. His guidance and advice were invaluable during my graduate school experience. I would also like to thank Dr. Roberto Celi and Dr. Anubhav Datta for agreeing to serve on my thesis committee and for their feedback on this research.

I would also like to thank Ashish Bagai and Martin Kearney of Aurora Flight Sciences for their early mentorship and guidance for this project.

I owe my deepest thanks to my family - to my mother and father who have always supported me in my endeavors and to my brother who continues to inspire me throughout my career. I would not have gotten to this point without their constant love and encouragement. Words can never express the gratitude I owe them.

Table of Contents

List of Tables

List of Figures

List of Abbreviations

ACUM	Acoustic Code University of Maryland
AFS	Aurora Flight Sciences
BEMT	Blade Element Momentum Theory
CFD	Computational Fluid Dynamics
dB	Decibels
dBA	Decibels A-weighted
DES	Detached Eddy Simulation
EPNL	Effective Perceived Noise Level
eVTOL	Electric Vertical Take-off and Landing
FM	Figure of Merit
FFT	Fast Fourier Transform
FSTI	Free Stream Turbulence Intensity
FWH	Ffowcs Williams & Hawkings
GARFIELD	GPU Accelerated Rotor Flow Field Solver
GPU	Graphics Processing Unit
Hz	Hertz
LES	Largy Eddy Simulation
OASPL	Overall Average Sound Pressure Level
Pa	Pascals
PAV	Passenger Air Vehicle
N	Newtons
NIHL	Noise Induced Hearing Loss
RANS	Reynolds Averaged Navier Stokes
RMS	Root Mean Square
RPM	Revolutions Per Minute
SA-DES	Spalart Allmaras Detached Eddy Simulation
SPL	Sound Pressure Level
UMD	University of Maryland
WENO	Weighted Essentially Non-Oscillatory

Chapter 1: Introduction

1.1 Motivation

Urban air taxi transport is currently of extremely high interest in the vertical flight community. The ability to forego the use of a traditional ground based vehicle would greatly change how we perceive transportation as a whole. Hours of productivity are lost by sitting in traffic, not to mention how a single interruption can cause serious delays.

Figure 1.1: Aurora Flight Sciences eVTOL aircraft prototype [1]

An on-demand electric vertical take-off and landing (eVTOL) vehicle, such as that shown in Figure 1.1 that was proposed by Aurora Flight Sciences, would greatly improve the convenience of travel [1]. With an aim to eventually have a fully autonomous vehicle, flying taxis are on their way to becoming reality.

Other companies such as Bell Flight and Uber Elevate have teamed up to create their own on-demand urban air taxi prototype called the Nexus, which is shown in Figure 1.2 [2].

Figure 1.2: Bell Flight Nexus eVTOL aircraft [2]

The Boeing Company, after pairing up with Aurora Flight Sciences, just revealed its Passenger Air Vehicle (PAV), shown in Figure 1.3. The PAV took its first flight on January 22nd, 2019 [3]. The PAV is being designed for a single passenger, whereas Bell Flight's vehicle is designed to hold multiple passengers.

All of these companies are striving for the same ultimate goal of making these

Figure 1.3: Boeing Passenger Air Vehicle (PAV) eVTOL aircraft [3]

urban air taxis a reality in the near future. Uber Elevate has stated they aim to begin commerical operations as early as 2023 [4].

To illustrate just how much an urban air taxi eVTOL vehicle is capable of revolutionizing travel, Uber Elevate provided an example of a commute comparing a traditional uberX vehicle with a VTOL aircraft. Shown in Figure 1.4, Uber Elevate promises to transform a 2 hour drive from the San Fransisco Marina to San Jose into just 15 minutes.

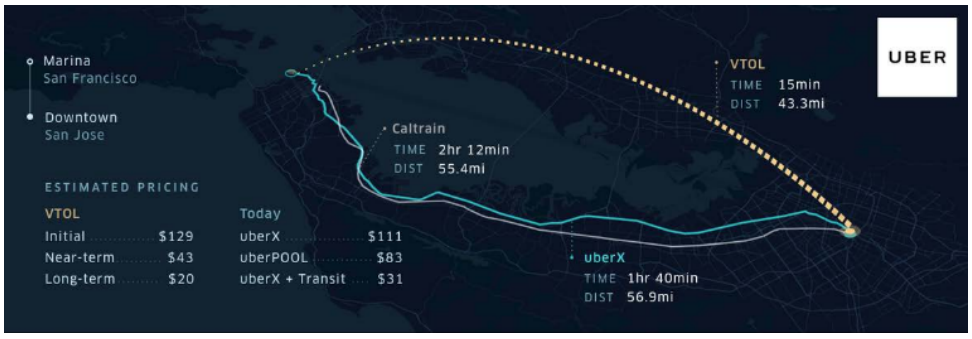

Figure 1.4: Uber Elevate sample eVTOL route from the San Fransisco Marina to San Jose [4]

Incorporating on-demand air travel in cities would increase mobility since fixed routes would no longer need to be followed. Transportation congestion on the ground would also be alleviated, which suggests safer commutes with potentially fewer traffic accidents. A VTOL aircraft also promises traveling at higher speeds from one destination to another. If the above commute was taken in just 15 minutes, the VTOL aircraft would be traveling close to 170 mph. In traffic, cars can often be stopped or traveling far less than the speed limit. By opening the transportation network into the third dimension, a lot of opportunities become possible. However, designing such a vehicle to operate in an urban environment raises some challenges [4].

In order for an urban air taxi to operate in a city, the aircraft needs to be widely accepted by the public. The first priority and primary concern is the safety of the vehicle. If the eVTOL aircraft is not proven to be safe for a passenger or multiple passengers, then the public will not accept the idea. However, once safety is ensured, another main concern that should be considered is the noise produced by the aircraft and how that can effect every day life. Large scale helicopters are perceived as very loud, but often don't operate consistently over large cities. If these urban air taxis will be constantly operating in the skies, the main goal is to design an aircraft that is as quiet as possible, but still efficient, to acheive widespread public acceptance of this future technology.

1.2 Background

A brief background of the sources of noise and how noise can be measured is provided. These areas of acoustics are important to understand for complete understanding of the aeroacoustic performance of various propellers analyzed in this thesis.

The main sources of noise considered in this thesis were thickness and loading noise and will be discussed separately.

1.2.1 Thickness Noise

Thickness noise is the noise that results from the displacement of air by the volume of the blade element. Thickness noise can be optimized by adjusting the blade's geometry such as thin blade sections or planform sweep.

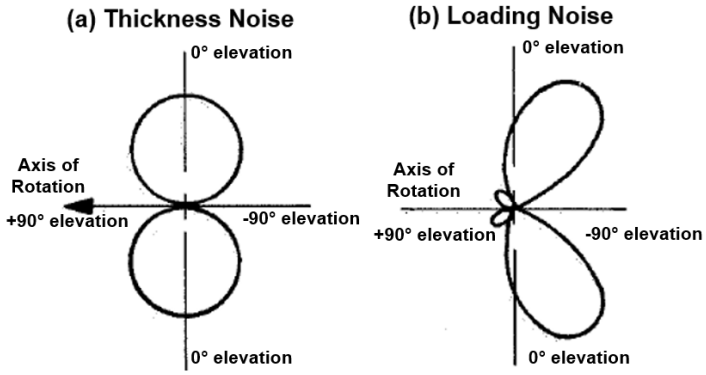

Figure 1.5: Polar plot of thickness (a) and loading noise (b) distributions [5]

Thickness noise is represented by a monopole source distribution and is important at higher speeds. A sample thickness noise polar plot distribution is shown

in Figure 1.5a. The maximum sound levels are experienced in-plane.

1.2.2 Loading Noise

Loading noise is the noise that results from the thrust and torque forces acting on the blade from pressure differences across the surface. Loading noise is represented by dipole sources and can be optimized by decreasing the aerodynamic loads experienced by a blade [6]. A sample polar plot loading noise distribution is also shown in Figure 1.5b. Loading noise is dominant out of plane and at low to moderate speeds, which is what is focused on in this thesis. Noise predictions are only as accurate as the aerodynamic interactions modeled, so great care must be taken with the aerodynamics to produce reliable and accurate acoustic results.

1.2.3 Other Sources of Noise

Since these vehicles are assumed to be powered by batteries, engine noise is not considered. Another source of noise is broadband noise. Broadband noise consists of a broad range of frequencies and often occurs due to turbulent flows and boundary layer noise. Broadband noise can be solved using empirical methods, but are not considered reliable as of yet. Broadband noise is difficult to predict by first principles and properly measuring broadband noise is a future area of research [7]. Therefore, broadband noise was not included in the analysis of the propeller test cases considered in this thesis. Only thickness and loading noise were considered, summed together to equal the total noise experienced by an observer.

It is also noted that an observer will experience a lot of different noises when walking in an urban environment. An eVTOL aircraft operating in the skies may be drowned out when considering the many different background noises that occur in a city. The street traffic noise, conversations, construction, and other disturbances may sound louder than the noise coming from the eVTOL vehicle. This illustrates that quantifying noise from one person to the next is not just a science. There is a psychological component to the study of acoustics that one should be aware of. Different people may view a different level of noise as "annoying". There still is not a consensus on what is considered the acceptable level of noise coming from an aircraft or any other source. However, an acoustic analysis can still be performed and analyzed using the most popular methods of measuring noise.

1.2.4 Measuring Noise

Three different methods of measuring noise are used through out this thesis: sound pressure level, overall average sound pressure level, and A-Weighted Decibels.

The sound pressure level (SPL) is what most people are familiar with. SPL is measured in decibels (dB) and is the logarithmic ratio of the root mean square (RMS) pressure to the reference pressure. Ultimately, sound is the result of pressure fluctuations. The decibel scale is calculated as follows, where p is the pressure fluctuation from ambient pressure and p_{ref} is the reference pressure, which is the minimum pressure difference that can be heard by humans (20 μPa):

$$dB = 20\ log_{10}\left(\frac{p}{p_{ref}}\right) \tag{1.1}$$

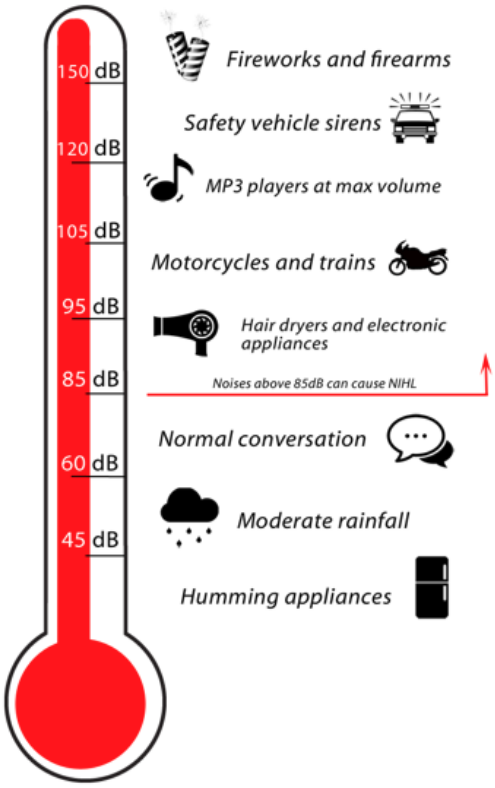

Figure 1.6: Decibel scale against common sounds heard by a human

For reference, common sounds experienced by a human are put onto a decibel scale in Figure 1.6. Any long-term exposure above 85 dB can cause noise induced hearing loss (NIHL). Around 70 dB would be the noise experienced by a normal conversation.

The SPL occurs at a particular frequency, whereas the overall average sound pressure level (OASPL) is the overall energy contained in the complete spectrum. The OASPL considers all frequencies that make up the pressure fluctuation time signal from a source. This is accomplished by performing a Fast Fourier Transform (FFT) that will be described in more detail in Chapter 2. Once all the frequenices are broken up, the SPL experienced at each frequency can be summed up to give

an OASPL. It is the equivalent SPL you would obtain by integrating across all frequencies.

Finally, A-Weighted Decibels (dBA) can also be used to measure noise. Since loudness is subjective, the decibel value measured is corrected using an "A-weight" factor to attempt to weight frequencies that are more annoying to the human ear. The weighted function and detailed calculation are discussed in Chapter 2.

All three of these noise measurements will be referenced and discussed throughout the thesis. Other noise measurements, such as the effective perceived noise level (EPNL), are more suitable for determining the noise at a site over a period of time with possibly many flights; as such it will not be examined in this thesis.

1.3 Thesis Contributions

The purpose of this thesis was to investigate different propeller designs that would not only be aerodynamically efficient, but also acoustically efficient. Various low aspect ratio propellers in hover were modeled, such as those found on the Aurora Flight Sciences eVTOL aircraft, to evaluate which specific design parameters effect the noise. This thesis looks at various propeller designs by varying planform, twist, number of blades, tip speed, and disk loading to reduce the OASPL experienced by an observer.

Aeroacoustic analysis for eVTOL vehicles has just begun to be investigated in the vertical flight community. The sources of noise had been rigorously studied in the 1990s by NASA Langley, but it is not yet widely known how exactly to optimize

aeroacoustic performance [8].

There are a few examples of earlier attempts of designing quieter aircraft. In 1948, an army liaison type aircraft that was unmodified was compared to a modified aircraft to reduce noise. The unmodified aircraft contained a propeller with two blades that were 85 inches in diameter. The modified aircraft used a propeller with five blades and an increased diameter of 96 inches, shown in Figure 1.7. The modified aircraft was measured to be 22 dB quieter than the unmodified aircraft at a distance of 50 feet from the center of the propeller [9]. The increased number of blades and lower disk loading proved to make a difference in the sound pressure level. However, there is still not a metric for what noise levels are considered acceptable by an observer.

Figure 1.7: Modified Army Liaison type aircraft to reduce noise [9]

In the Vietnam era, the Lockheed YO-3A, called the "Quiet Star" was one of the first designed stealth aircraft, shown in Figure 1.8. Instead of being designed to be invisible to radar detection, it was designed to be acoustically undetectable. The Quiet Star accomplished this by a slower turning propeller and a modified exhaust.

Figure 1.8: Lockheed Quiet Star aircraft [10]

The muffler was very large in length to allow the noise to be largely dampened. The lower revolutions per minute (RPM) engine also helped to keep the aircraft quiet. The Quiet Star was often used for observing troop movement in Vietnam [10].

The data produced from this thesis aims to further advance these early efforts of designing quiet aircraft, towards designing an eVTOL vehicle that can be used in the near future in urban environments. This thesis contributes to the vertical flight community by understanding how to design a quieter, efficient aircraft using computational methods and principles of sound reduction, rather than experimental results. Specifically, this thesis will help determine which design parameters contribute to an aeroacoustically efficient aircraft. Identifiying these parameters and using them to design a quieter, efficient aircraft will help gain wide spread acceptance from the public on this new on-demand urban air taxi concept, in hopes of this idea becoming a reality in the 2020's.

1.4 Research Outline

This thesis is focused on identifying design parameters to maximize the aerodynamic performance while minimizing the noise. The rest of the thesis is organized as follows:

- Chapter 2 discusses the methodology used for both the aerodynamic solvers and the acoustic solver. The computational fluid dynamics (CFD) solver chosen and the accompanying blade element momentum theory (BEMT) analysis are covered in detail. The details of the CFD simulation are discussed on all propeller test cases. The acoustic solver and the observer locations chosen are presented. Chapter 2 outlines the complete computational aeroacoustic framework used for this thesis.

- Chapter 3 provides a summary of the propeller test cases considered in hover. This chapter introduces the various test cases evaluated in BEMT and how certain cases were chosen to be further evaluated in CFD. Chapter 3 discusses in detail the design parameters that were analyzed to investigate their impact on minimizing the noise.

- Chapter 4 discusses the aerodynamic results from all the propeller test cases. The isolated propeller cases are presented first, followed by the propeller cases implemented with a nearby boom geometry. The design parameters to improve aerodynamic performance are analyzed and identified.

- Chapter 5 discusses the acoustic results from all the propeller test cases. Just as

in Chapter 4, the isolated propeller test cases are presented first. The OASPL and the A-weighted OASPL for each propeller design is presented. The design parameters to improve acoustic performance are analyzed and identified.

- Chapter 6 summarizes all of the work conducted in this study, identifying the design parameters most important in improving the aeroacoustic performance. Chapter 6 discusses recommendations for future analysis to further characterize aeroacoustic performance.

Chapter 2: Methodology

2.1 Overview of Computational Aeroacoustic Framework

The normal and chordwise forces (actually $C_n M^2$ and $C_c M^2$ since proportional to these forces) along the propeller blade at various spanwise locations were calculated through one of the aerodynamic solvers - either BEMT or CFD. These forces were input into the acoustic solver to solve the Ffowcs Williams Hawkings (FWH) equation to calculate pressure fluctuations, and then were changed into sound pressure levels that could be used to understand the relative loudness of certain propeller designs. This overall computational aeroacoustic framework is discussed in detail below, starting with the two different aerodynamic solvers used followed by the acoustic solver of choice.

2.2 Aerodynamic Solvers

2.2.1 Computational Fluid Dynamics (CFD) - GARFIELD

The solver chosen for performing 3D aerodynamic analysis was a Graphics Processing Unit (GPU) Accelerated Rotor Flow Field Solver (GARFIELD) that was created at the University of Maryland. It is a structured, three-dimensional Reynolds-

Averaged-Navier Stokes (RANS) solver and has been widely tested. GARFIELD contains viscous and turbulence models and works on an overset framework so that individual meshes from the blades, background, etc. can overlap [11].

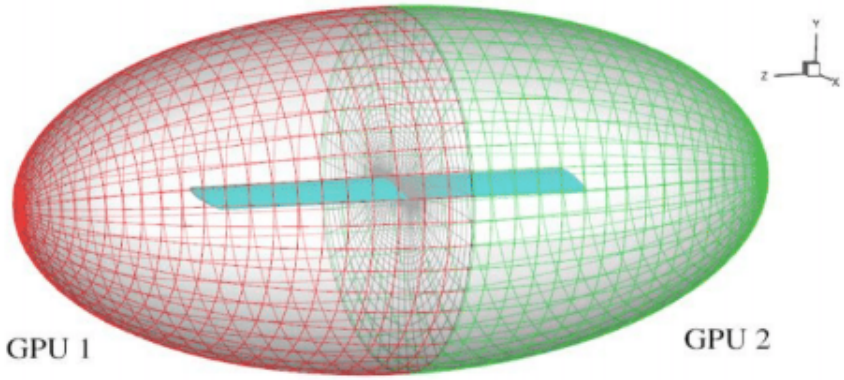

Figure 2.1: Example parallelization of multiple GPUs in GARFIELD

GARFIELD is parallelized across multiple GPUs as seen in Figure 2.1. In this case the rotor blade is split between two GPUs. The parallelization of multiple GPUs makes GARFIELD a quicker solver than other CFD codes [11]. The CFD simulations were run on two different supercomputers located at the University of Maryland and the Johns Hopkins University, called Deepthought 2 and Bluecrab respectively.

2.2.2 GARFIELD Strengths

GARFIELD has no limitation on the chosen propeller geometry, unlike that of BEMT that will be discussed in the next section. Chord, taper, twist, sweep, variation of airfoil section, etc. can all be considered. All flow conditions can be

simulated and the overset meshing generation allows for nearby geometries to be included with the propeller to capture the true aeroacoustics. As mentioned above, since GARFIELD is GPU accelerated test cases can run much faster than many other CFD solvers [11]. CFD is a higher fidelity solver than BEMT and allows for a more accurate representation for aerodynamic and acoustic performance.

2.2.3 GARFIELD Limitations

GARFIELD has a lot of strengths and potential for many uses, but it is important to note that running different propeller test cases takes a long time using CFD. This is true for all CFD solvers. On average in GARFIELD it takes about 6-8 hours per rotor revolution for the isolated propeller cases when using twelve GPU's. Once other nearby geometries are added, thus adding even more mesh points, this process takes even longer, sometimes up to 12 hours per rotor revolution. In order to ensure a solution is converged and the root vortex is completely blown down for a proper power prediction, these cases were often run out to 12 revolutions. Therefore, most propeller cases took up to 96 hours of run time for convergence, with some maximum run times of 144 hours.

2.2.4 Simulation Details

The airfoil section chosen for all of the propeller cases analyzed was an SC1095. This airfoil was chosen arbitrarily, known for having relatively good aerodynamic

performance and a common airfoil used in vertical flight applications. An O-mesh was created for the SC1095 airfoil and can be seen in Figure 2.2.

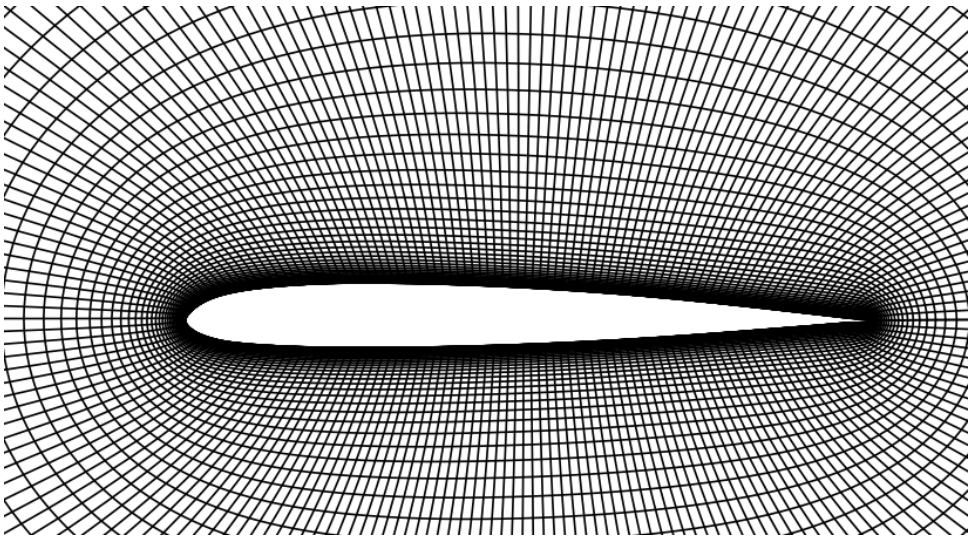

Figure 2.2: 2D SC1095 blade mesh

Great care was taken at the trailing edge of the airfoil to make sure that the cells of the mesh were not too skewed. Once satisfied with the 2D mesh, and a chord distribution was decided upon, a 3D O-O mesh was created. The 3D blade mesh can be seen in Figure 2.3 with the tip cap added to close the end of the blade. The chord distribution chosen for the various propeller cases is explained in more detail in Chapter 3. The 3D blade mesh in Figure 2.3 shows the elliptic planform, used in the majority of the propeller cases analyzed.

All isolated propeller cases (except one test case run with transition modeling) were run fully turbulent using the Spalart-Allmaras Detached Eddy Simulation (SA-DES) turbulence model. DES combines the best features of the RANS and Large Eddy Simulation (LES) methodologies in a single solution hybrid technique. A RANS approach is used for the near wall regions, whereas an LES approach is

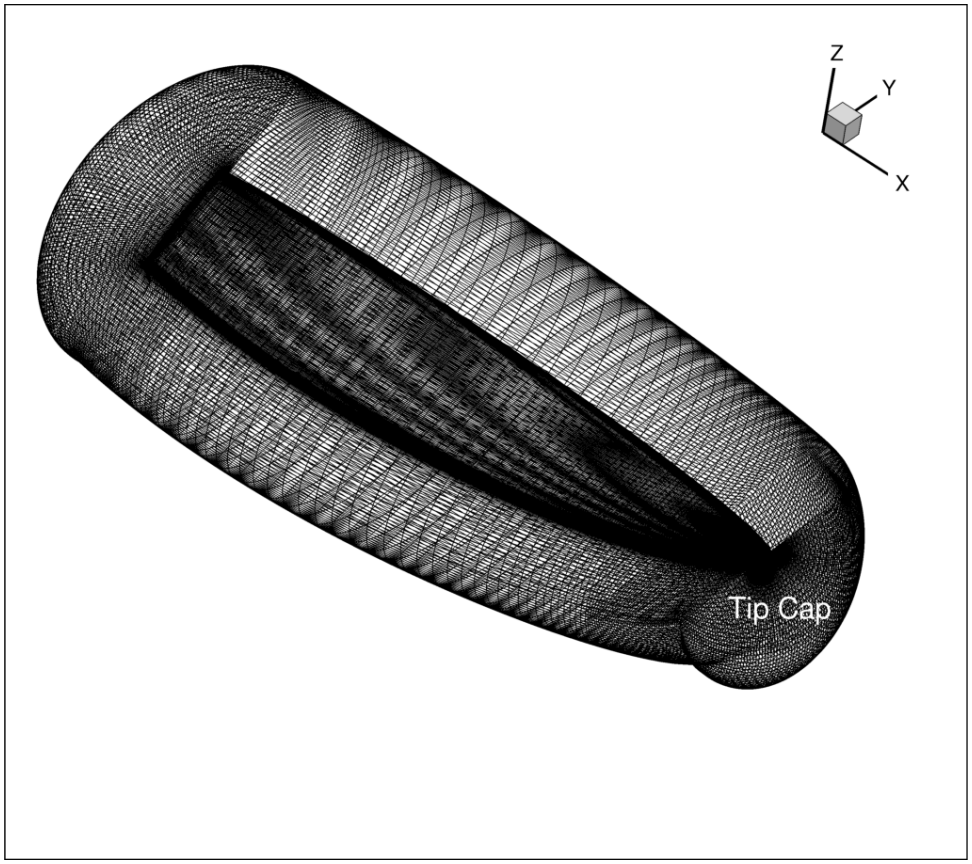

Figure 2.3: 3D blade mesh for elliptic planform

used for the rest of the flow. A 5th order accurate reconstruction scheme, Weighted Essentially Non-Oscillatory (WENO), was used for the spatial discretization scheme. A 1st order accurate time marching method, Euler Implicit was used. A time-step of a quarter of a degree was used for the earlier revolutions of the propellers. Once the solution had settled down, the last 1-2 revolutions were usually run with an eighth of a degree time-step for even better accuracy.

For the isolated propeller test cases a fine nested mesh was placed around the blades to be able to capture nearby transients. The background mesh is much coarser since fluctuations in farfield quantities are not expected. These meshes are

shown in more detail in Figure 2.4.

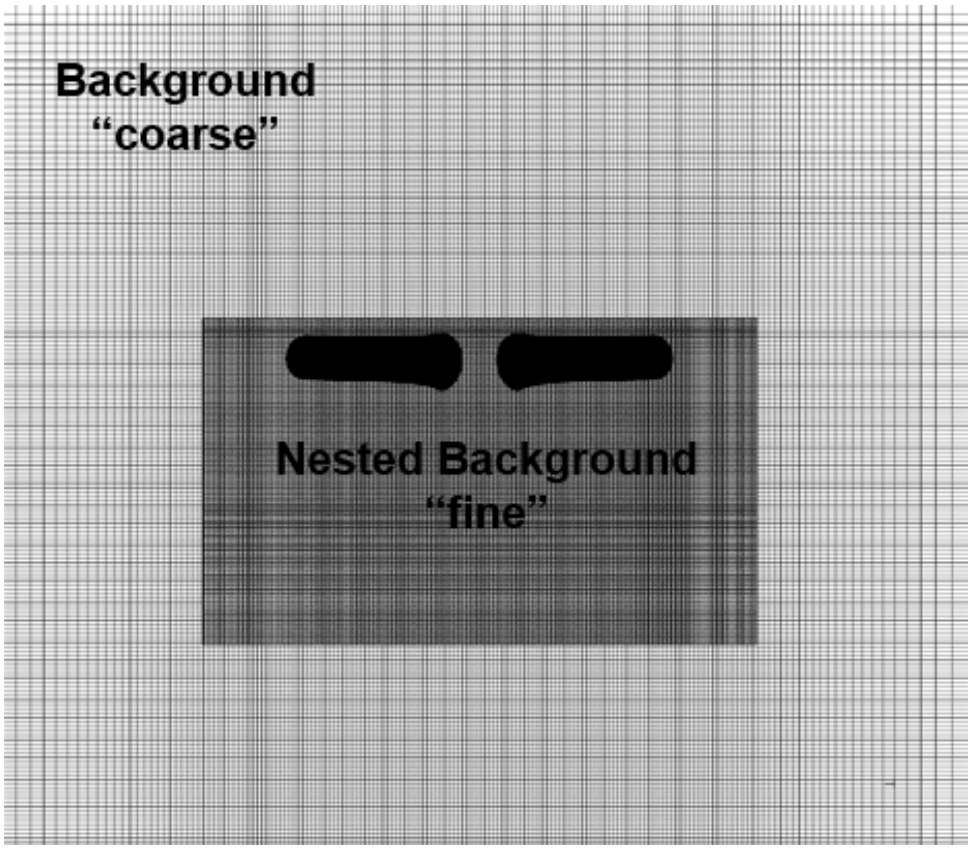

Figure 2.4: Fine nested mesh and background mesh for isolated propeller cases

The number of points for each mesh were:

Blade: 1.68 million points (each)

Nested Background: 7.8 million points

Background: 11.6 million points

The relative placement of the meshes can be seen in Figure 2.5. The outer boundaries of the background mesh are placed far enough away to reach farfield conditions. It is placed 10 rotor radii below the blades to ensure enough room for the wake to blow down and only 5 rotor radii away horizontally from the blades since we do not

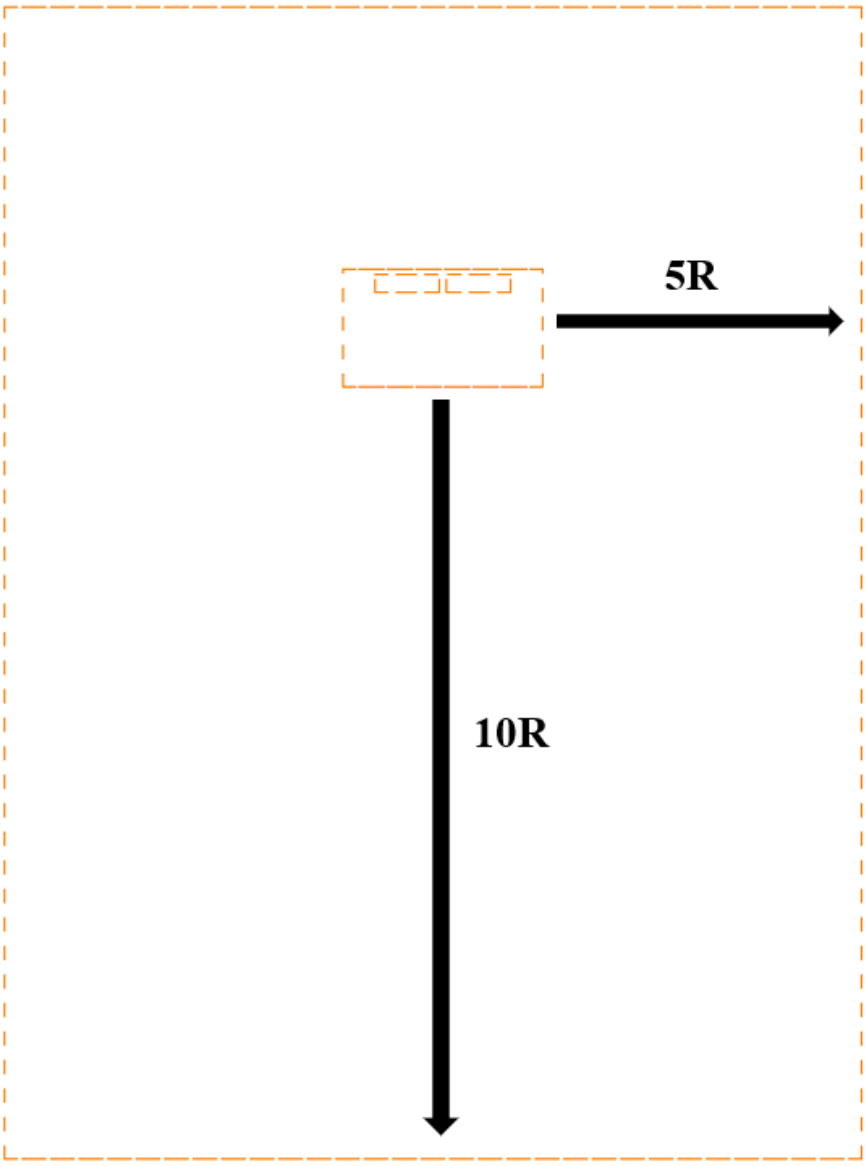

Figure 2.5: Relative mesh placement for isolated propeller cases

expect as much propogation of information in that direction. In hover when the propeller was in isolation, all the grids were allowed to rotate.

For all propeller test cases run in GARFIELD, a free-wake initialization was implemented to accelerate convergence. By prescribing a sample wake solution as the initial solution for these test cases, the time needed for the wake to form was

significantly decreased. The free-wake initialization used a sample solution to establish a wake to accelerate convergence. The free wake-initialization used was from a Harrington 2 rotor simulation. This was generically chosen and the wake was rescaled to match the radius of the propeller test cases analyzed.

Next, a plausible boom geometry was given from Aurora Flight Sciences and was added to the propeller cases. The boom geometry and its cross section are shown in Figure 2.6. The top of the boom is aerodynamically shaped, and the bottom corners were kept rigid and were not rounded.

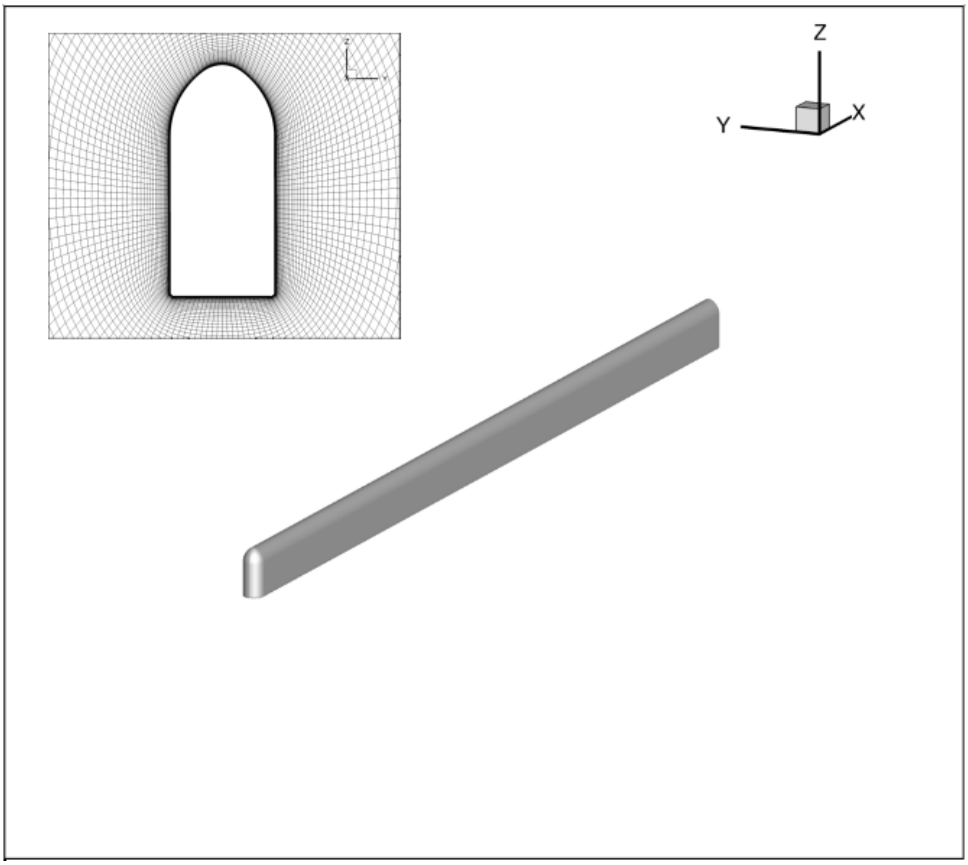

Figure 2.6: Plausible boom geometry given by Aurora Flight Sciences

The rigid corners did not cause any issues in meshing or convergence and due

to time constraints the boom geometry was not further edited. It can also be seen in the Boeing PAV aircraft that the boom underneath has rigid corners, therefore to best simulate a realistic case the corners were kept rigid. The 2D mesh and 3D mesh for the boom were created similarly to the blade mesh, by thinking of the boom cross section as an airfoil rotated upwards.

Aurora Flight Sciences was interested in placing the boom at two different vertical placements below the propeller to evaluate the resulting aeroacoustic performance. The boom geometry was 6 rotor radii (R) in length and was placed either 0.25R or 0.50R below the propeller. A "semi-infinite" boom geometry was also implemented (only 3R in length instead of 6R), such that the boom would only be below one of the blades of the propeller. The semi infinite boom geometry would simulate what the two front or two back propellers on the Aurora Flight Sciences eVTOL aircraft would experience. The propeller placement at 0.25R for the full boom and semi-infinite boom are shown in Figure 2.7.

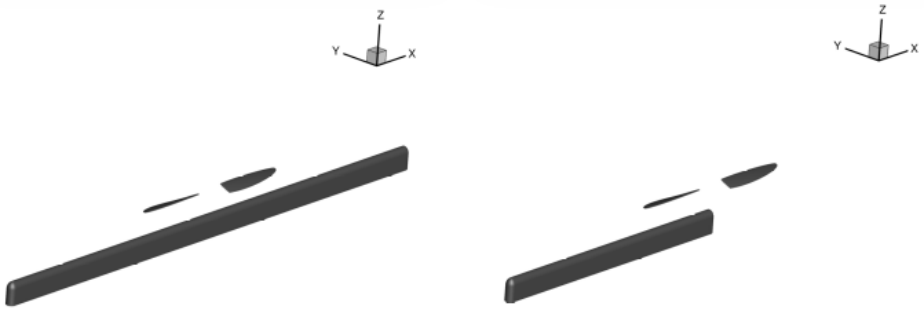

Figure 2.7: Boom placement 0.25R below propeller for full boom and semi-infinite boom

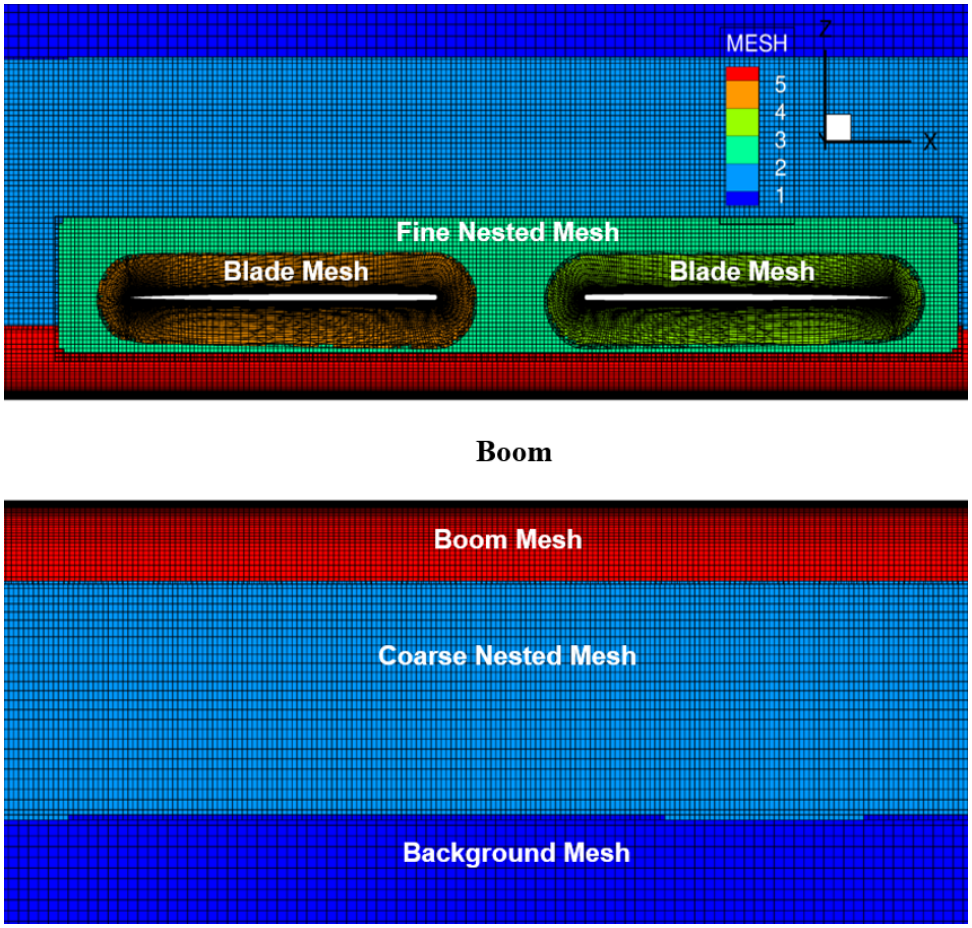

Figure 2.8: Mesh placement of propeller cases with nearby boom geometry

In order to accurately predict the interactional aerodynamics when incorporating the nearby boom geometry, additional meshes were added while being cognizant of mesh placement and overlap. A second, even finer nested mesh was placed around the blades to capture the resulting unsteady airloads. The relative mesh placement for the propeller cases including the boom geometry at 0.25R vertical placement is shown in Figure 2.8. The fine nested mesh, coarse nested mesh, and background mesh gradually become coarser so the cell sizes gradually increase and are able to capture all the complex flow phenomena around the blades and the boom. At the

0.25R distance, the boom mesh significantly overlapped the blade meshes and fine nested mesh. At the 0.50R distance there was not as much mesh overlap. The number of points for each mesh were:

Blade: 2 million points (each)

Boom: 4 million points

Fine Nested Background: 2.4 million points

Coarse Nested Background: 7.8 million points

Background: 14.3 million points

For the boom cases, all the grids could no longer rotate, since the boom was to remain stationary below the propeller. GARFIELD is able to isolate each mesh and prescribe whether it should be rotating or stationary. Therefore, the blades were allowed to rotate, but the boom and background meshes remained stationary.

Finally, for one test case implementing the boom geometry the propeller was chosen to be canted at a 10° angle. This was explored to investigate the aeroacoustic performance when the propeller was slightly angled and not parallel above the boom geometry. In Figure 2.9, the angled propellers can be seen on the Boeing PAV.

It is predicted that the propellers are canted to provide some stability to the aircraft. Thus, the cant angle was estimated as about 10°, and the initial mesh placement and setup can be seen in Figure 2.10.

However, for simplicity, the boom geometry was rotated 10° instead of having to rotate the blades and fine nested mesh. With just the boom geometry rotated, this would give the same solution as if the blades were rotated by the same amount, just

Figure 2.9: Boeing PAV propeller cant angle

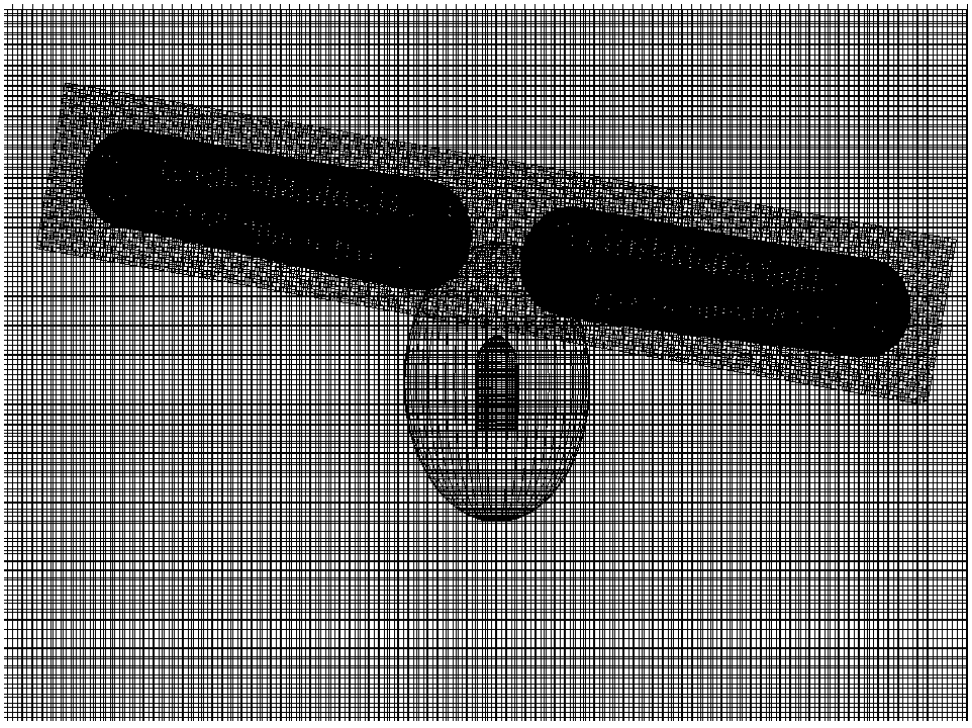

Figure 2.10: Mesh placement illustrating 10° cant angle

taking care to measure the thrust in the correct orientation. The mesh placement that was actually used in the CFD simulation with just the boom rotated is shown in Figure 2.11.

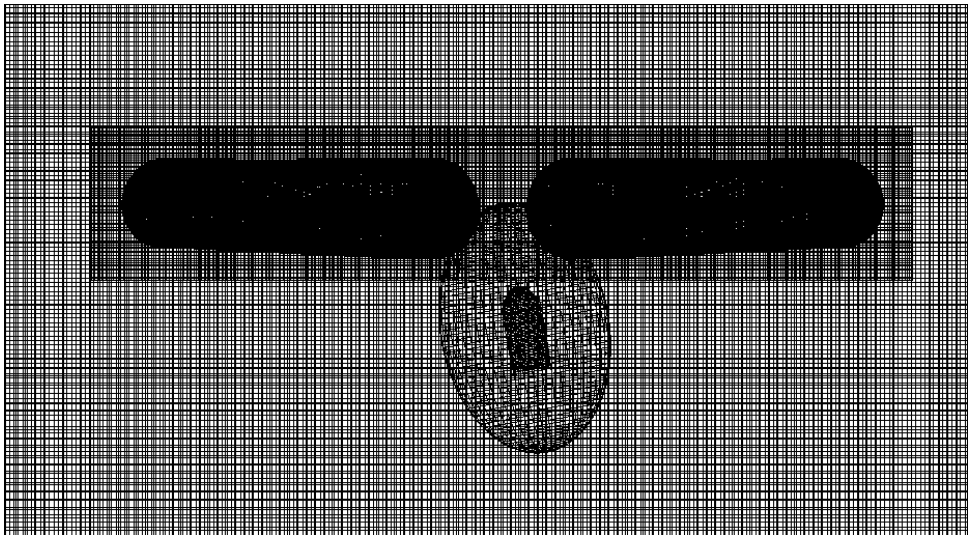

Figure 2.11: Mesh placement utilized for the cant angle propeller case, Case 18

2.2.5 GARFIELD Post Processing

Once the isolated and boom geometry propeller cases were carried out to 12 revolutions for convergence, the aerodynamic performance was evaluated by integrating the torque and thrust forces along the blade. These forces were originally in CFD units and were non-dimensionalized into the popular non-dimensional quantities of thrust and torque, C_T and C_Q. These quantities were then dimensionalized into thrust and power units by the following:

$$T = C_T \ \rho A \left(\Omega R\right)^2 \tag{2.1}$$

$$P = C_P \ \rho A \left(\Omega R\right)^3 \tag{2.2}$$

In order to trim the propeller to the appropriate design thrust, the collective or pitch angle of the blade was changed accordingly. This often took about 2 to 3 iterations of changing the collective angle in order to achieve the thrust desired. Once the

design thrust was obtained, the Figure of Merit, or hovering efficiency, used as a metric for the aerodynamic performance, was then calculated as follows:

$$FM = \frac{\frac{T^{3/2}}{\sqrt{2\rho A}}}{P} \tag{2.3}$$

The normal and chordwise forces were recorded along the blade and input into the acoustic solver. The normal and chordwise forces were evaluated at 95 spanwise locations to obtain proper representation of the variation of these forces along the blade. These forces were obtained at 36 different azimuth locations (every 10 degrees). For the isolated propeller cases in hover, both forces along the blade were the same at all azimuth locations since the forces were steady and constant in time. For the boom propeller cases the unsteady forces varied in time and were collected every 10 degrees in azimuth. To ensure the unsteady forces were properly represented, a time step discretization study was performed. These forces were written to two files for the normal and chordwise forces respectively. A deflections file was written containing the spanwise point locations where those forces were evaluated, the chord distribution of the propeller to represent the propeller's geometry and any structural information. In these test cases there were no deflections of the blade since flap, lag, and torsion were not included or considered. These three files - the normal force, chordwise force, and deflection files - were the quantities needed as inputs into the acoustics solver.

2.2.6 Blade Element Momentum Theory (BEMT)

A BEMT analysis was added to quickly assess the aerodynamic performance of propeller geometries of interest. The BEMT code was implemented in the computational aeroacoustic framework as a quick assessment of a variety of propeller cases, such that the most promising ones could be identified and further analyzed in CFD. Since one propeller revolution took about 6-8 hours using GARFIELD, it was important to eliminate propeller cases in BEMT and choose only those cases worthwhile for testing. The BEMT analysis was created in MATLAB where a chord distribution at certain radial points was defined, along with the desired operating conditions and design thrust. The BEMT analysis was based off of all fundamental equations given in *Principles of Helicopter Aerodynamics* [12].

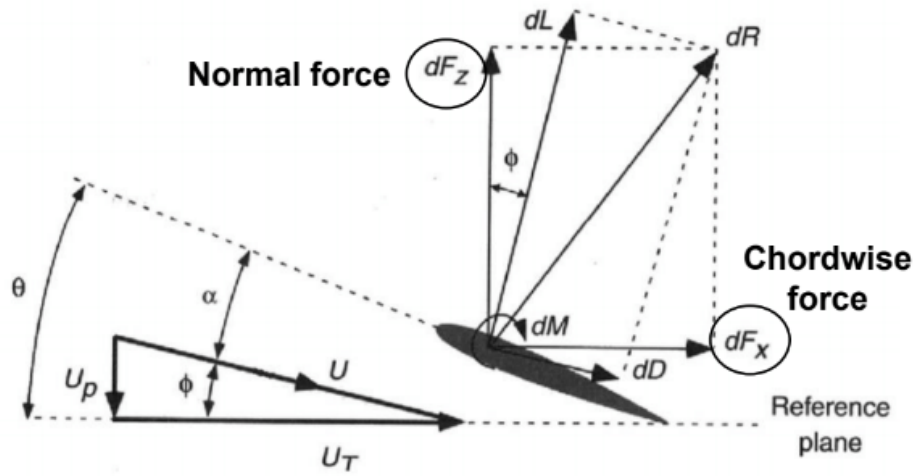

Figure 2.12: Blade Element diagram illustrating incident velocities and the aerodynamic environment

Figure 2.12 shows a typical blade element with incident velocities and the

aerodynamic forces and moments expected. In BEMT the blade is discretized into a series of N small elements of span Δr. For the propeller cases analyzed, the blade was split into 42 elements to ensure the blade was discretized enough to properly capture the aerodynamics.

In the blade element diagram the velocity U is broken up into the tangential and vertical components U_T and U_P respectively. θ is the pitch angle, α is the angle of attack, and ϕ is the inflow angle. Mathematically, BEMT equates the incremental thrust coefficients from the momentum and blade element theories:

$$\frac{\sigma C_{l\alpha}}{2}\left(\theta r^2 - \lambda r\right) = 4F\lambda^2 r \tag{2.4}$$

where σ is the rotor solidity, $C_{l\alpha}$ is the lift coefficient at the current angle of attack, θ is the pitch angle as stated above, λ is the inflow, r is the radial station along the blade, and F is the correction factor. BEMT is a lower-fidelity solver and predicts Figures of Merit much higher than that found in GARFIELD. As a lower fidelity solver, there are limitations to the model. Both root and tip losses were included in the BEMT model, illustrated by the correction factor F, to include as many approximations for complex 3D effects as possible.

The correction factor includes both the tip loss and root loss factors. The tip loss factor is introduced to account for the effects of high induced velocities produced at the blade tips by the trailed tip vortices on the rotor thrust and induced power. The root loss factor is added in to account for the loss of lift at the root of the blade. No small angle assumptions were used in the BEMT analysis. The tip loss

factor is calculated as follows with r_0 representing the initial radial station taking into account root cutout and N_b as the number of blades being considered:

$$f_{tip} = \frac{N_b}{2}\frac{1-r}{(r-r_0)\,sin\phi} \tag{2.5}$$

This can be used to calculate the correction factor due to tip loss:

$$F_{tip} = \frac{2}{\pi}cos^{-1}\left(exp\left(-f_{tip}\right)\right) \tag{2.6}$$

The root loss factor is calculated similary to the tip loss factor:

$$f_{root} = \frac{N_b}{2}\frac{r_0-r}{(r-1)\,sin\phi} \tag{2.7}$$

The correction factor due to root loss is calculated the same way as that from tip loss:

$$F_{root} = \frac{2}{\pi}cos^{-1}\left(exp\left(-f_{root}\right)\right) \tag{2.8}$$

Finally, both of these loss factors can be combined into a single correction factor function:

$$F = F_{root}F_{tip} \tag{2.9}$$

This is the correction factor used in the following equations. The inflow variation along the blade can be solved by rearranging Equation 2.4 and solving the quadratic:

$$\lambda^2 + \frac{\sigma C_{l\alpha}}{8F}\lambda - \frac{\sigma C_{l\alpha}}{8F}\theta r = 0 \tag{2.10}$$

which has the solution:

$$\lambda\left(r\right) = \frac{\sigma C_{l\alpha}}{16F}\left(\sqrt{1+\frac{32F}{\sigma C_{l\alpha}}\theta\left(r_n\right)r_n}-1\right) \tag{2.11}$$

With 42 element stations, r_n and $\theta(r_n)$ are the radius and pitch angle at the mid-span of each of the 42 stations. All aerodynamic forces and moments are found at the mid-span location of the elements. Since F is a function of the inflow, Equation 2.11 cannot be solved immediately. As a result, Equation 2.11 must be solved iteratively. The inflow is initially guessed to be uniform and equal to $\sqrt{\frac{C_T}{2}}$ from momentum theory and is updated until convergence is reached.

Once a final inflow distribution is known, the spanwise distribution of airloads can be calculated using the local angle of attack, inflow angle, and pitch angle. The BEMT code is able to read in supplied airfoil tables of lift and drag as a function of angle of attack and Mach number instead of assuming constant lift slope or constant drag. The normal force and chordwise forces, $C_n M^2$ and $C_c M^2$, are shown in the direction of the coordinate directions dFz and dFx respectively in Figure 2.12, and are collected and saved into files of the same format as that indicated for CFD for input to the acoustics solver. The deflections file is also created using the same process. These three files are input into the acoustic solver to convert the aerodynamic forces into pressure fluctuations and eventually into decibel (dB) levels to evaluate the resulting noise. To find the Figure of Merit in BEMT, the total thrust on the propeller and total power can be found by numerically integrating over the blade.

$$C_T = \sum_{n=1}^{N} \Delta C_{Tn} \tag{2.12}$$

$$C_P = \sum_{n=1}^{N} \lambda_n \Delta C_{Tn} \tag{2.13}$$

The Figure of Merit is then calculated the same way as that in CFD using the

dimensional thrust and power quantities.

Even with its limitations, the overall trends are still properly captured from BEMT to be able to identify design parameters that result in a more aerodynamically efficient propeller. Therefore, the resulting airloads obtained from the BEMT analysis were used in the acoustic solver to calculate the noise for comparison to the CFD airloads and acoustic performance for further validation of the results.

2.3 Acoustic Solver

The in-house Acoustic Code University of Maryland (ACUM) accepts the airloads calculated from CFD or BEMT and solves the inpermeable surface form of the FWH equation to obtain the resulting pressure fluctuations. The FWH equation is well known in the aeroacoustic community and relies on near-field information over a surface that encloses the sources of noise as much as possible [6]. Figure 2.13 shows the differential form of the FWH equation and what each component corresonds to.

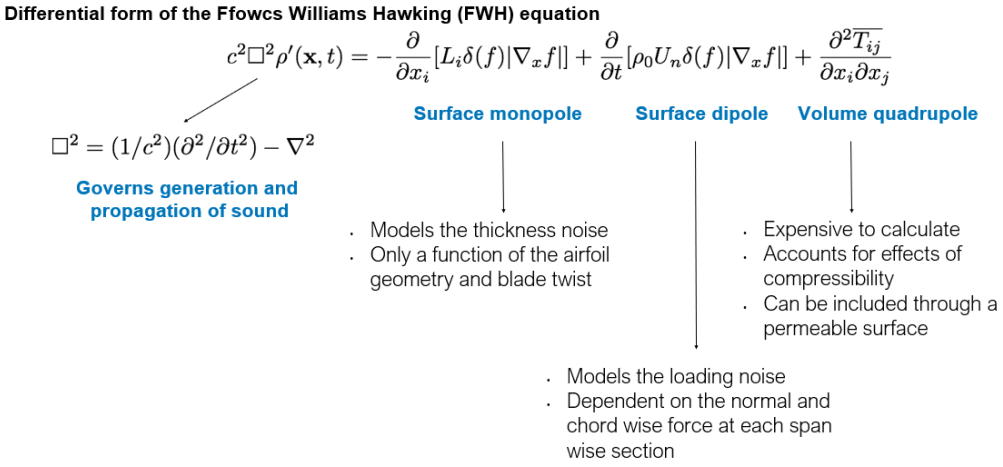

Figure 2.13: Differential form of the Ffowcs Williams and Hawkings equation

Essentially the generation and propagation of sound is governed by the surface monopole, dipole, and quadropole sources (if included) that dictate the sources of noise as discussed in Chapter 1. The pressure fluctuations found by the FWH equation were then converted into a SPL in dB given in Equation 1.1 in Chapter 1.

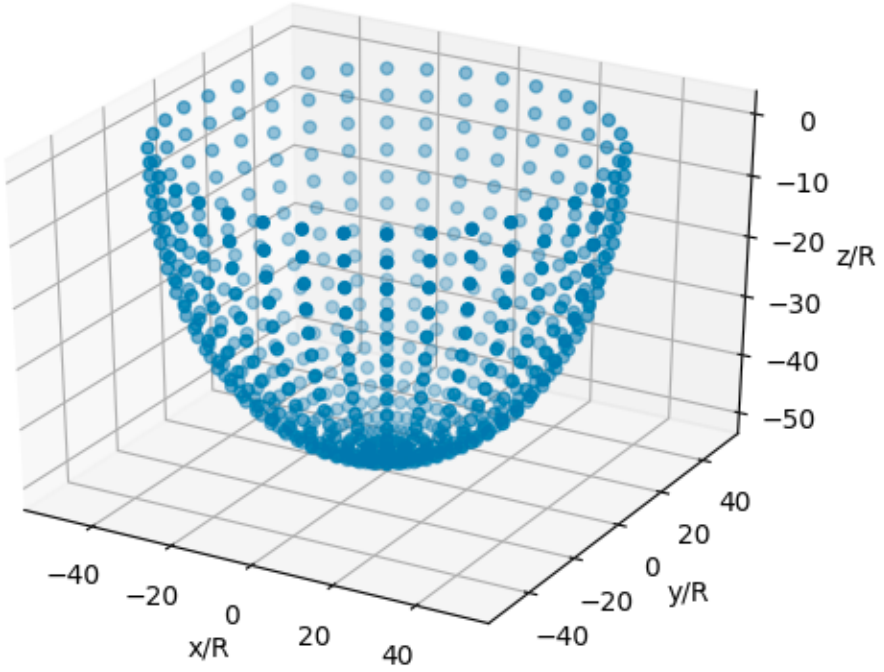

Figure 2.14: Observer locations placed in 50m hemisphere

Polar directivity plots were often generated to show the SPL in dB 360° around the rotor at observer locations 50 meters away. The observer locations were chosen at various elevation angles above and below the propellers so the observer locations formed a 50m radius sphere. In reality, most observers will be below the propellers since the eVTOL aircraft will be flying above most observers in an urban environ-

ment. Therefore, these full "sphere" polar directivity plots only often considered the bottom hemisphere, as that contained the observer locations of interest, and the highest levels of noise. The observer locations for the hemisphere are shown in Figure 2.14. They were discretized by 10° in azimuth and 5° in elevation.

For an isolated propeller in hover, the noise is only a function of elevation and not the azimuth position of the blade. This is because the airloads in hover are steady and not changing with time. Therefore, the same loads would be experienced at every 10° discretization in azimuth, and thus the same SPL would be experienced regardless of azimuth position. Therefore, once the dB levels were captured as a function of elevation angle, the maximum SPL was found for all propeller test cases to be located approximately 25° below the propeller. The maximum SPL experienced at a radius of 50 meters away from the propeller was chosen as the acoustic metric to measure the acoustic performance. Therefore, the observer location at 25° below the propeller was often chosen as the primary point of interest since it contained the maximum SPL. That observer location was analyzed in more detail for all the propeller cases where a pressure time history signal was produced to be used in an FFT analysis. As mentioned in Chapter 1, the signal was then broken up into multiple frequencies where each SPL could be summed up to give an OASPL. This OASPL corresponds to the SPL experienced at 25° below the propeller.

A sample pressure fluctuation signal is shown in Figure 2.15. The pressure time history is then broken up into multiple frequencies, shown in Figure 2.16.

The FFT analysis changes the pressure signal, originally measured in Pascals (Pa) in time, into the frequency domain. Once in the frequency domain the pressure

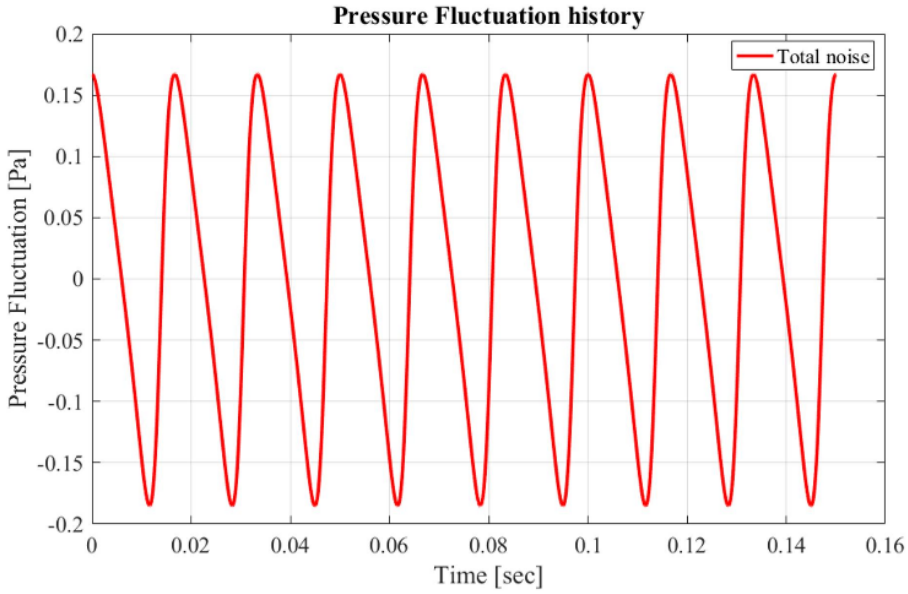

Figure 2.15: Sample pressure fluctuation signal

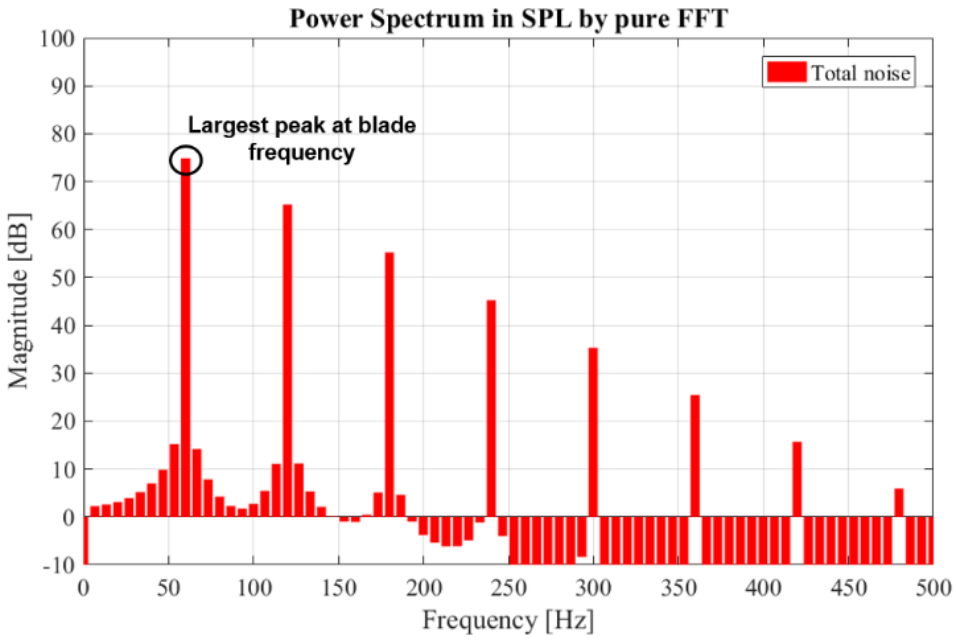

Figure 2.16: Sample pressure fluctuation signal broken up into multiple frequencies via FFT analysis

was changed from Pa to dB using Equation 1.1. The result gives Figure 2.16, with different dB levels at various frequencies. These dB levels were then changed into dBA levels in the frequency domain. This procedure started with the A weighting function, $R_A(f)$. The A weighting function is based on the fact that the A weighting is equivalent to 0 dB at 1000 Hertz (Hz). Therefore, any pressure signal at 1000 Hz will be heard at the same dB and dBA level, since a human is not sensitive one way or the other at 1000 Hz.

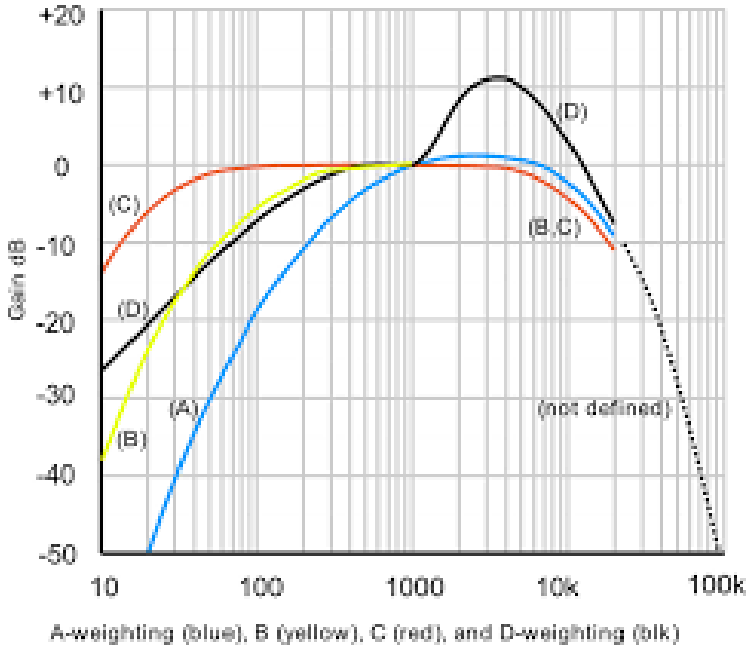

Figure 2.17: A, B, C, D weighting curves as filter functions [13]

However, it is argued that a human tends to be more sensitive at higher frequencies and thus will have a smaller A weight value resulting in higher noise. The A-weighting function, $R_A(f)$, and how its value changes at various frequencies is shown in Figure 2.17. The A-weighting function is as follows:

$$R_A(f) = \frac{(12194^2 f^4)(f^2 + 12194^2)^{-1}}{(f^2 + 20.6^2)\sqrt{(f^2 + 107.7^2)(f^2 + 737.9^2)}} \tag{2.14}$$

The actual A weighting to be added to the dB level is then calculated:

$$A\ Weight = 20\ log_{10}(R_A(f)) + 2.00 \tag{2.15}$$

Each of the dB levels at the various frequencies are then changed to dBA by adding the A weighting found above:

$$dBA = dB + A\ Weight \tag{2.16}$$

Once the dB and dBA values were collected at all the frequencies, they were summed up and put into an overall sound pressure level in both dB and dBA:

$$OASPL(dB) = 10\ log_{10} \sum 10^{dB/10} \tag{2.17}$$

$$OASPL(dBA) = 10\ log_{10} \sum 10^{dBA/10} \tag{2.18}$$

The OASPL in dB and dBA was compared across all eighteen propeller cases and were used as the metric for acoustic performance. The OASPL in dB is reported for these cases as the more popular acoustic metric, but the OASPL is also reported in dBA to account for humans not hearing all frequencies equally.

When introducing a nearby body, the SPL will not only vary as a function of elevation, but also as a function of azimuth. The resulting unsteady airloads from a nearby body will cause the airloads to vary in time. Therefore, for the propeller cases with the boom geometry, the maximum SPL was first found at a particular elevation, and then at that elevation the azimuth position where the maximum SPL occurred was chosen.

Chapter 3: Summary of CFD Propeller Cases

3.1 Preliminary BEMT Analysis Results

First, the operating conditions for various propeller cases were chosen based off of approximations of what would be expected by a single propeller on the Aurora Flight Sciences eVTOL aircraft. With guidance from Aurora Flight Sciences, the operating conditions were determined and are listed in Table 3.1.

Table 3.1: Operating Conditions for Propeller Test Cases

Radius	0.925 m
Design Thrust	1,000N
RPM	1800
Number of Blades	2
Speed of Sound	340 m/s
M_{tip}	0.5128
Airfoil	SC1095
Root Cutout	20%
C_T/σ	0.12

The radius of the blades was kept relatively small, keeping in mind the spatial constraints of the propellers near the fuselage body in the Aurora Flight Sciences eVTOL prototype aircraft. Aurora Flight Sciences mentioned the motors would be

able to operate between 1,000 and 3,000 RPM, so an RPM setting near the middle was chosen to keep the tip Mach number from being too high to raise concern. As mentioned in Chapter 2, the SC1095 airfoil was chosen arbitrarily for its popular use in vertical flight vehicles.

The blade loading, C_T/σ, was kept constant across all propeller cases to ensure they could all be fairly compared to each other. The design thrust and airfoil were kept constant in all cases as well. However, radius, RPM, number of blades, and tip Mach number were allowed to be varied to understand their impact on aeroacoustic performance. The operating conditions listed here were preliminary and were used for the baseline propeller test case. Variations in design parameters that made up the operating conditions were then explored and will be discussed in this Chapter.

After the baseline operating conditions were decided upon, a baseline propeller geometry had to be determined. In order to decide on a baseline propeller geometry, several propeller geometries were rapidly explored in BEMT. Three different planforms, rectangular, 2:1 taper, and elliptic were chosen to evaluate the benefit of taper on the aerodynamic efficiency. Two different linear twist rates, 0° and 25°, were chosen to evaluate their benefit on hover efficiency.

The results of the early BEMT analysis are shown in Table 3.2. The BEMT analysis revealed that the elliptic planform, 25° linear twisted blade was the most aerodynamically efficient. This comes as no surprise, since the elliptic planform minimized the profile power, and the twisted blade minimized the induced power to keep the inflow more constant over the blade. With the profile and induced power minimized, the elliptic linearly twisted propeller was thus most efficient with

a predicted Figure of Merit of 0.866.

Table 3.2: Preliminary BEMT Aerodynamic Results

Planform	Twist	Figure of Merit(BEMT)
Rectangular	Zero	0.721
Rectangular	25° Linear	0.811
2:1 Taper	Zero	0.745
2:1 Taper	25° Linear	0.846
Ellipse	Zero	0.782
Ellipse	25° Linear	0.866

Again, it is noted that these Figure of Merit values are higher than would actually be expected. This is because BEMT is a lower fidelity solver; however, the overall trends of the benefits of taper and twist are shown in the BEMT results and enable a choice of a plausible baseline propeller geometry.

3.2 Baseline Propeller Geometry

After preliminary analysis using BEMT, the baseline propeller geometry was chosen as an elliptic planform with linear twist. The elliptic planform was chosen due to the tapered geometry minimizing profile power, and increasing aerodynamic performance. The linear twist was chosen as a baseline since the twisted blade minimized induced power and thus also increased aerodynamic performance. The baseline propeller geometry is shown in Figure 3.1.

Figure 3.1: Elliptic planform - baseline propeller geometry

3.3 Isolated Propeller Cases (Cases 1-7, 12-17)

Once a baseline propeller configuration was decided upon, slight deviations from the baseline were considered to see their relative effects on aeroacoustic performance. An elliptic planform with zero twist was included to observe any effects of adding twist in the reduction of noise. Two different modifications of the linear twist distribution from the baseline case at 0.90R were considered to observe any benefit of bi-linear twist in the aerodynamic performance or acoustic performance. The twist distributions for cases 1-4 are shown in Figure 3.2. It is noted that at 0.75R, the twist is zero degrees for all cases. This is so the collective applied to the blade will follow the popular convention of equaling the pitch angle at 0.75R.

Cases 5-7 explore the increase in number of blades and reduction of RPM on aerodynamic and acoustic performance. Case 5 reduced the RPM setting from 1800 to 1470. This RPM setting was decided upon such that if the number of blades was

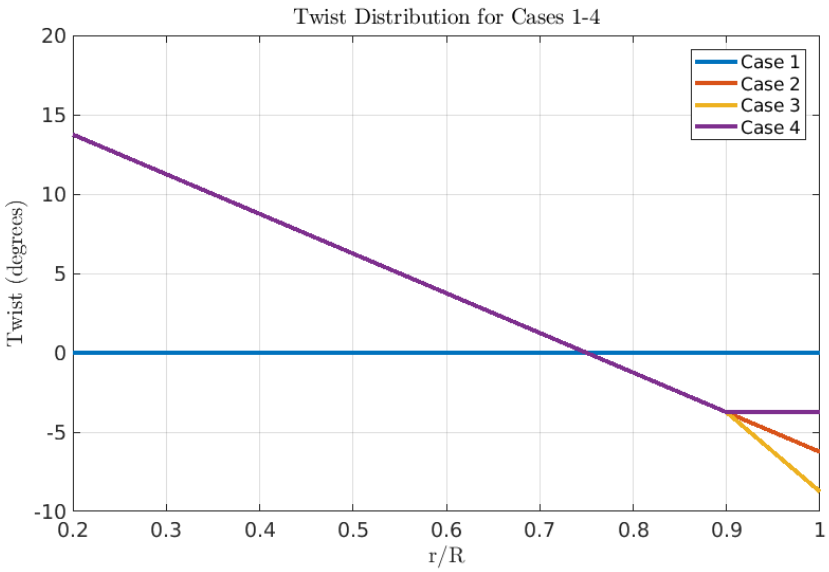

Figure 3.2: Cases 1-4 twist distribution

increased to 3 from the conventional 2 bladed rotor both the RPM and number of blades changes would keep the blade loading constant. This can be more easily seen below:

$$C_T = \frac{T}{\rho A \left(\Omega R\right)^2} = \frac{1,000}{1.2256 * \pi * 0.925^2 * \left(1800 * \frac{2}{3} * 2\pi/60 * 0.925\right)^2} \tag{3.1}$$

$$\sigma = \frac{N_b c}{\pi R} = \frac{2 * \frac{3}{2} * 0.1210}{\pi * 0.925} \tag{3.2}$$

Since the RPM was reduced to 1470, it was $\sqrt{2/3}$ that of the original RPM setting, decreasing the tip Mach number from 0.5128 to 0.4188. The solidity was increased by 3/2 from changing the number of blades from 2 to 3. Since C_T increased by 3/2 and so did the solidity, these changes cancel out and result in the same blade loading. Case 5 explored the effect of just reducing RPM by decreasing from 1800 to 1470, and then adjusting the equivalent chord to give the same blade loading. This meant that the chord was increased by a factor of 3/2. Case 6 reduced the

RPM and increased the number of blades as explained above. Case 7 then just explored the effect of increasing the number of blades, thus adjusting the equivalent chord to decrease by a factor of 3/2 to maintain the same blade loading. A table summarizing these propeller cases and the first four cases described earlier, is shown below in Table 3.3.

Table 3.3: Overview of Propeller Test Cases 1-7

Case Number	Planform	Twist	RPM	Number of Blades
1	Ellipse	Zero Twist	1800	2
2	Ellipse	Linear	1800	2
3	Ellipse	Linear Increased at 90% R	1800	2
4	Ellipse	Linear Constant at 90% R	1800	2
5	Ellipse	Linear	1470	2
6	Ellipse	Linear	1470	3
7	Ellipse	Linear	1800	3

Cases 8-11 were the propeller cases including the nearby boom geometry and will be discussed in the next section. The rest of the isolated propeller cases will be outlined here.

Cases 12 & 13 explored the effect of aft and forward sweep. The aft sweep was accomplished by starting at the 50% spanwise position (or the location with the largest chord along the blade) and sweeping the quarter chord such that with the elliptic planform the trailing edge becomes straight. This created a reasonable amount of sweep to analyze the effect of sweep on the acoustics. The forward sweep

then was accomplished by sweeping the quarter chord forward by the same amount that it was swept back for the aft swept blade. The aft swept geometry can be seen in Figure 3.3.

Figure 3.3: Case 10 aft sweep geometry

Cases 14 & 15 looked at the effect of changing planforms by implementing the rectangular and 2:1 taper geometries that were first explored in BEMT. The side by side comparison of the aft and forward sweep propeller geometries are shown in Figure 3.4. The rectangular and 2:1 taper geometries are shown in Figure 3.5.

Case 16 analyzed the effect of transition modeling versus a fully turbulent simulation to see how much the decreased drag from allowing a laminar region over the blade would decrease the noise. Case 16 was run with a free stream turbulence intensity (FSTI) of 0.10%. All other propeller test cases were run fully turbulent.

Finally, Case 17 increased the radius of the blade, thus decreasing the disk loading to evaluate its effect on aeroacoustic performance. The disk loading, T/A was chosen to be decreased by 20%, and since all of these cases were trimmed to

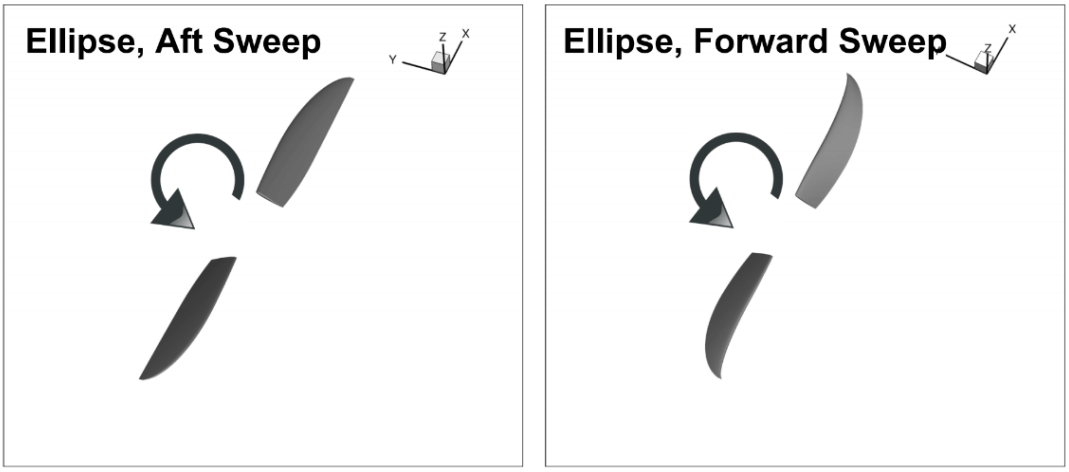

Figure 3.4: Cases 12 & 13, aft and forward sweep propeller geometries

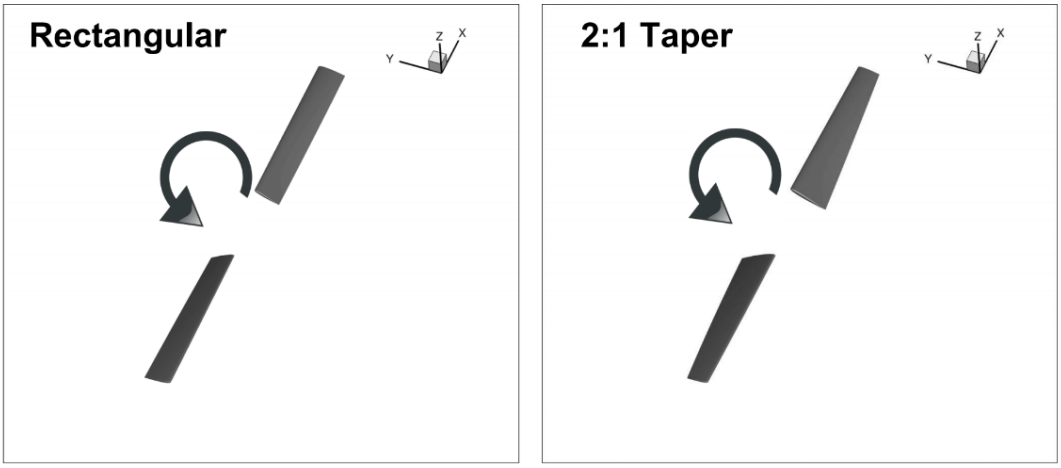

Figure 3.5: Cases 14 & 15, rectangular and 2:1 taper propeller geometries

the same thrust, this resulted in the radius being increased from 0.925 m to 1.0133 m. In order to keep the blade loading constant, the RPM and/or equivalent chord had to be adjusted. In order to avoid having a larger tip Mach number, resulting in more compressibility effects, the tip Mach number was kept constant from the baseline case. Thus in order to maintain a tip Mach number of 0.5128, the RPM was decreased to about 1643 from 1800. As a result, the equivalent chord had to be

adjusted as well to maintain a blade loading of 0.12.

$$\frac{C_T}{\sigma} = 0.12 = \frac{\frac{1{,}000}{1.225*\pi*1.0133^2*(1643*2\pi/60*1.0133)^2}}{\frac{2*c}{\pi*1.0133}} \tag{3.3}$$

Solving for the equivalent chord, the equivalent chord had to be decreased from 0.1210 m to 0.1104 m.

These were the isolated propeller cases that were analyzed to view the various design parameters that could affect the aerodynamic and acoustic performance. A summary test matrix containing all the propeller cases analyzed is presented at the end of the next section.

3.4 Propeller with Boom Cases (Cases 8-11, 18)

Aurora Flight Sciences expressed interest in implementing a boom beneath the propeller to look into the unsteady loads that would result from this situation. The unsteady loads would further influence the acoustics and in reality propellers will not operate in isolation as in Cases 1-7 & 12-17 above.

The boom geometry given by Aurora Flight Sciences and its relative placement with the propeller was shown in Chapter 2 at a vertical separation of 0.25R. The full boom geometry was 6 rotor radii long. The semi-infinite boom where the boom only extends past the propeller on one side instead of both, was 3 rotor radii long.

The test matrix for the different boom cases is in Table 3.4 with the boom location expressed as the vertical separation between the propeller and the boom in rotor radii. Two vertical separation distances were considered, 0.25R and 0.50R, to investigate the effect of the vertical placement on the aerodynamics and acoustics.

Table 3.4: Overview of Propeller Test Cases 8-11 & 18 with Boom Geometry

Case Number	Planform	Sweep	Type of Boom	Boom Location	Cant Angle
8	Ellipse	No Sweep	Full	0.25R	0°
9	Ellipse	No Sweep	Full	0.50R	0°
10	Ellipse	Aft Sweep	Full	0.25R	0°
11	Ellipse	No Sweep	Semi-Infinite	0.25R	0°
18	Ellipse	No Sweep	Full	0.25R	10°

The baseline propeller geometry was used in all the boom cases, except for Case 10. Case 10 implemented the same aft swept geometry as Case 12. The case numbers for the propeller tests were labeled in the order that they were run and analyzed. The aft swept geometry was first used in the boom case and then further explored in isolation due to the interesting aeroacoustic results. This will be discussed further in Chapters 4 and 5. Case 18 tilted the boom by an angle of 10° as discussed in Chapter 2. Therefore, in short, the boom cases contained the boom at 0.25R and 0.50R with the baseline propeller geometry, an aft swept propeller at 0.25R, a semi-infinte boom at 0.25R with the baseline geometry, and the baseline propeller geometry canted at a 10° angle with the boom at 0.25R.

All eighteen of these cases were run in GARFIELD and coupled to ACUM to give the resulting Figure of Merits and OASPL to assess aeroacoustic performance. Figure 3.6 illustrates the different design parameters considered for all the test cases analyzed in a color coded manner for easier viewing and understanding.

Case Number	Planform	Radius	Twist	RPM	N_b	Sweep	Turbulence Model	Design Parameter
1	Ellipse	0.925m	N/A	1800	2	N/A	Fully Turbulent	Twist
2	Ellipse	0.925m	Linear	1800	2	N/A	Fully Turbulent	
3	Ellipse	0.925m	Linear, increased twist rate 90%R	1800	2	N/A	Fully Turbulent	
4	Ellipse	0.925m	Linear, no twist 90%R	1800	2	N/A	Fully Turbulent	
5	Ellipse	0.925m	Linear	1470	2	N/A	Fully Turbulent	Number of Blades & RPM
6	Ellipse	0.925m	Linear	1470	3	N/A	Fully Turbulent	
7	Ellipse	0.925m	Linear	1800	3	N/A	Fully Turbulent	
8	Ellipse, Boom 0.25R	0.925m	Linear	1800	2	N/A	Fully Turbulent	Boom Geometry
9	Ellipse, Boom 0.50R	0.925m	Linear	1800	2	N/A	Fully Turbulent	
10	Ellipse, Boom 0.25R	0.925m	Linear	1800	2	Aft Sweep	Fully Turbulent	
11	Ellipse, Semi-Infinite Boom 0.25R	0.925m	Linear	1800	2	N/A	Fully Turbulent	
12	Ellipse	0.925m	Linear	1800	2	Aft Sweep	Fully Turbulent	Sweep
13	Ellipse	0.925m	Linear	1800	2	Forward Sweep	Fully Turbulent	
14	Rectangular	0.925m	Linear	1800	2	N/A	Fully Turbulent	Planform
15	2:1 Taper	0.925m	Linear	1800	2	N/A	Fully Turbulent	
16	Ellipse	0.925m	Linear	1800	2	N/A	Transition Modeling	Transition
17	Ellipse	1.0133m	Linear	1643	2	N/A	Fully Turbulent	Disk Loading
18	Ellipse, Boom 0.25R Canted 10°	0.925m	Linear	1800	2	N/A	Fully Turbulent	Boom Geometry

Figure 3.6: Complete test matrix of all the propeller cases analyzed

Chapter 4: Aerodynamic Results

4.1 Isolated Propeller Test Cases

Cases 1-4 with the ellipse planform, standard operating conditions, and the different twist distributions were run first. The finalized wake structure for Cases 1-4 is shown below in Figure 4.1.

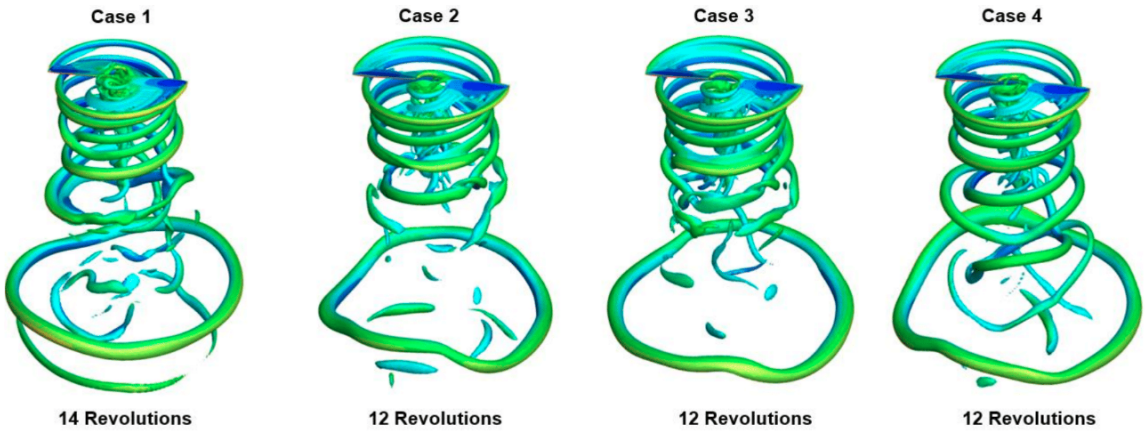

Figure 4.1: Cases 1-4 wake structure

All cases except Case 1 was run out to 12 revolutions to ensure the root vortex had completely blow down. Another way to more easily see the root vortex and if it has properly blown down is by looking at vorticity contours on a Z-X plane at a Y location of zero. The vorticity contours after 12 revolutions for Case 2, the baseline

case, are shown in Figure 4.2. The root vortex is completely blown down, thus giving a proper power prediction and evaluation of aerodynamic performance. However, since Case 1 was an untwisted blade, the root vortex was a little stronger, causing the simulation to have to be run a little longer (14 revolutions) for complete convergence. All remaining propeller cases had a twisted blade and were consistently run out to 12 revolutions to obtain convergence. The final thrust values and corresponding Figure of Merits for Cases 1-4 are reported in Table 4.1. The Figure of Merit is a hover efficiency, varying from 0 to 1, with 1 being 100% efficient. A good propeller design should yield a Figure of Merit in the range of 0.7-0.8.

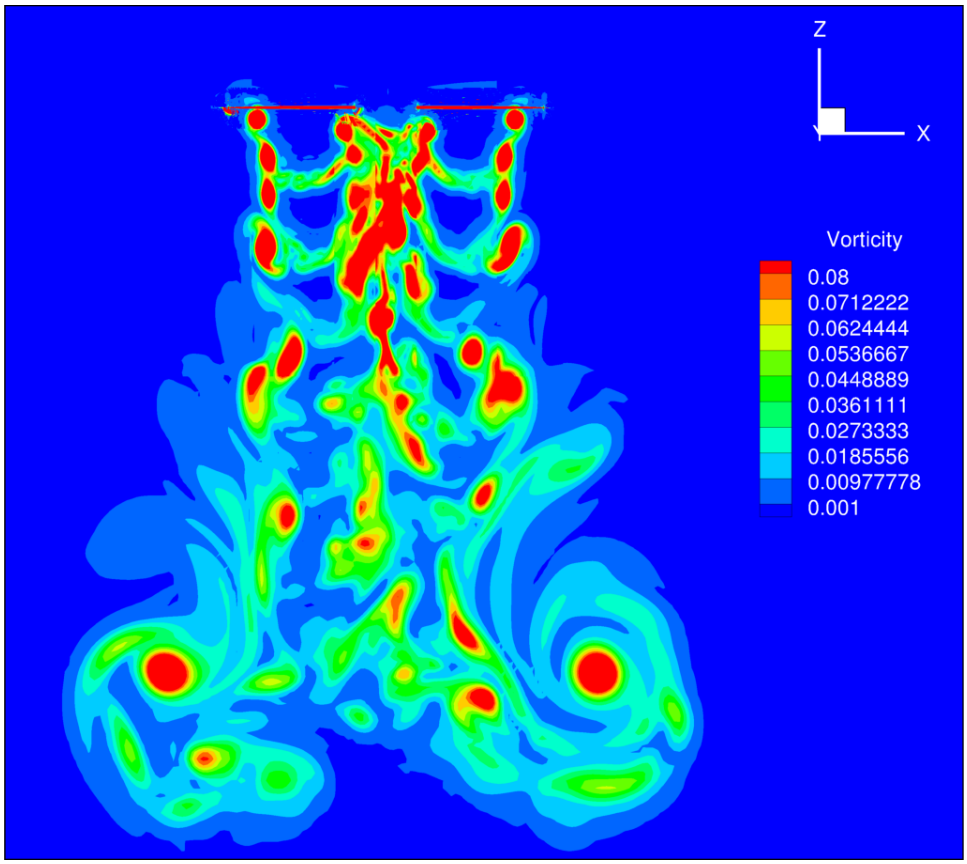

Figure 4.2: Case 2 (baseline case) vorticity contours on Z-X Plane

Table 4.1: Cases 1-4 CFD Aerodynamic Results

Case	Thrust (N)	Figure of Merit	Collective (deg.)
1	983	0.679	13.70
2	993	0.726	12.58
3	997	0.730	12.71
4	992	0.724	12.47

For the untwisted blade, the Figure of Merit was 0.679. A fairly decent improvement in Figure of Merit from Case 1 (0.679) to Case 2 (0.726) is acheived (untwisted to linear twist), which is expected. This makes sense as twist helps to minimize the induced power by having more uniform inflow over the blade. Comparing Cases 2, 3, and 4, however, it can be seen that the Figure of Merit does not fluctuate much at all. By changing the twist at the tip (0.9R), there is not a noticeable change in aerodynamic performance. By increasing the twist rate at the tip (Case 3), we get a slight improvement from 0.726 to 0.730 and by keeping the twist angle constant at the tip (Case 4), we get a slight decrease in performance from 0.726 to 0.724.

The spanwise loads $C_n M^2$ and $C_c M^2$ were scaled by $\frac{c}{R}$ so the loads could be analogous to thrust and power and easily analyzed between different propeller cases. These spanwise loads scaled by $\frac{c}{R}$ can be seen in Figure 4.3. Figure 4.3 shows the normal and chordwise forces scaled by chord for only one blade. Since all four of these cases had two blades, the loads did not need to be scaled by the number of blades. For later cases, the spanwise loads were also multiplied by the number of

blades to compare the total normal and chordwise forces between propeller cases. For example, these loads would be multiplied by two in order to show the total normal and chordwise forces. However, since Cases 1-4 all consisted of the same number of blades, this multiplication factor of two was not necessary to make aerodynamic performance comparisons at this time.

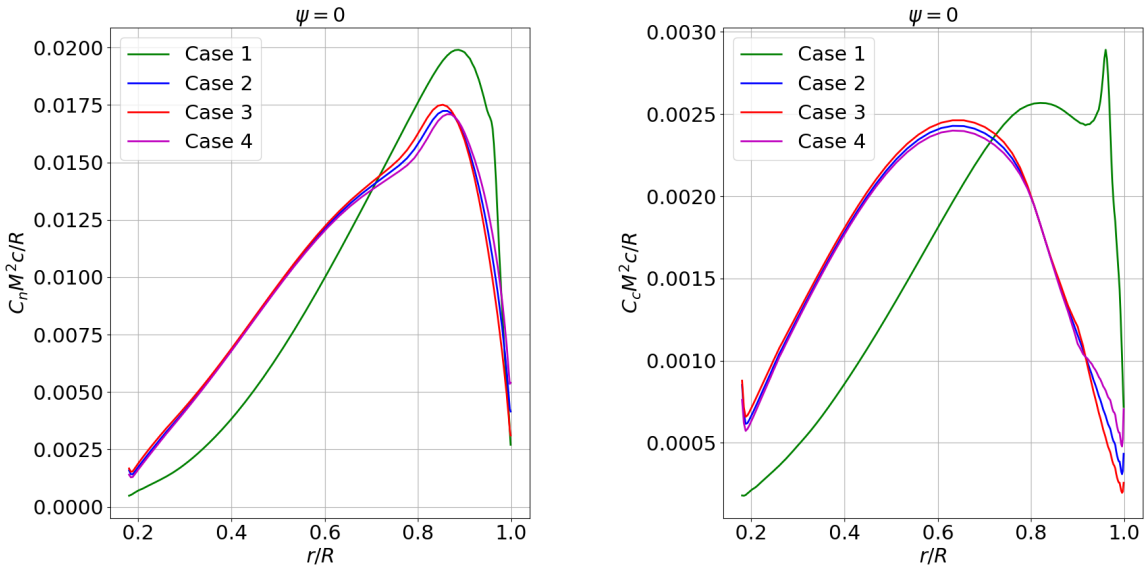

Figure 4.3: Cases 1-4 spanwise airloads at $\psi = 0°$

The untwisted blade, Case 1, shows a smaller normal force inboard compared to Cases 2-4. The subtleties by Cases 2-4 can be seen, where depending on the twist at the tip the normal force is pushed slightly further inboard or outboard. As we would expect, when the twist is increased at the tip (Case 3) a slight benefit in Figure of Merit should be obtained. Since all of these cases were trimmed to the same thrust of about 1,000 Newtons (N), the area under the curve for $C_nM^2\frac{c}{R}$ should be equal across all cases, which by inspection appears to be so. The actual

thrust acheived in these four cases is reported in Table 4.1 above and they are all within 20 N of the 1,000 N target design thrust.

These Figures of Merit were then compared to the results obtained from BEMT. These results are tabulated in Table 4.2.

Table 4.2: CFD & BEMT Aerodynamic Results Comparison

Case	BEMT Figure of Merit	CFD Figure of Merit
1	0.783	0.679
2	0.866	0.726
3	0.863	0.730
4	0.865	0.724

The substantial benefit in the aerodynamic performance from Case 1 to 2 is captured by both BEMT and CFD. BEMT gives a larger and more optimistic benefit compared to that of CFD. However, when looking at Cases 3 and 4 with the subtle changes in twist rate at 0.9R, the BEMT Figures of Merit do not match the trends given by the CFD results. When the twist rate is increased at the tip (Case 3), the Figure of Merit is ever so slightly lower than the baseline case (Case 2). For Case 4, when the twist rate is constant at the tip there is a very slight increase in hover efficiency. This is exactly the opposite of what is obtained with CFD.

However, these discrepancies between BEMT and CFD actually make sense. The subtle changes of twist at the tip of the blade will result in 3D effects that cannot be properly predicted by BEMT. As stated before, this is to be expected since BEMT is an optimistic, lower fidelity solver and cannot model the more complex 3D effects in the flow. This is why the Figure of Merits in BEMT for Cases 3 and 4 vary

only by 0.35% or 0.12% from the baseline case. The CFD spanwise loads for Cases 2, 3, and 4 are very similar to each other when looking at Figure 4.3, therefore BEMT was probably not able to capture these subtleties in the loads and thus the subtle differences in Figure of Merit. However, the same overall trends are captured when looking at BEMT and CFD. Having a linear twist distribution significantly improves the aerodynamic performance, but modifying the twist affects the Figure of Merit very little. Thus, introducing twist is worthwhile to increase the aerodynamic efficiency of the aircraft (Case 1 to Case 2), but modifying the twist rate may only be beneficial if it has a significant impact on noise. The bi-linear twist rates at 0.9R do not effect the aerodynamic performance significantly, but may potentially have an effect on the acoustic performance.

Cases 5-7 were then analyzed to explore the impact of increasing the number of blades from two to three, and reducing the RPM from 1800 to 1470. For Case 5 the RPM was reduced to 1470, thus needing to increase the chord by a factor of 3/2 to keep the blade loading constant at 0.12. For Case 6 the RPM was also reduced to 1470, but instead of increasing the chord to keep blade loading constant, the number of blades was increased from 2 to 3. Case 7 was at the nominal RPM of 1800, with three blades, thus needing to decrease the chord by a factor of 3/2 to obtain the same blade loading.

The wake structure for Cases 5-7 are shown in Figure 4.4. The change of the aspect ratio can be also be observed in Figure 4.4 by the effect of increasing or decreasing the chord. All three cases converged at 12 revolutions with the root vortex blown all the way down to obtain an accurate and proper power prediction.

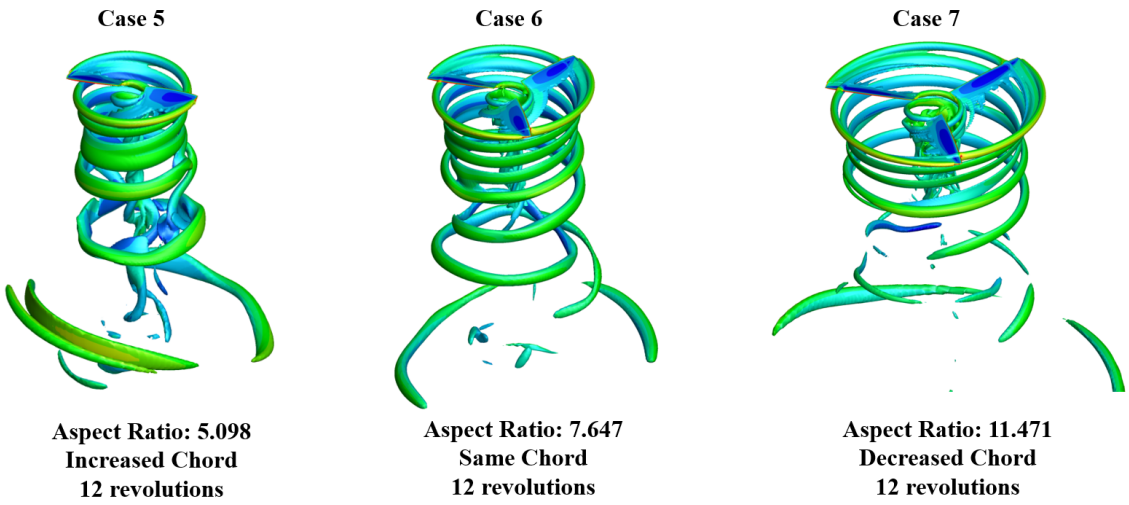

Figure 4.4: Cases 5-7 wake structure

The final thrust values and corresponding Figure of Merits for Cases 5-7 are reported below in Table 4.4. The span-wise loads for these three cases and the baseline case (Case 2) are shown in Figure 4.5. The spanwise loads $C_n M^2$ and $C_c M^2$ are again scaled by $\frac{c}{R}$. Since these cases have a different number of blades when compared to each other, this must be accounted for to appropriately compare thrust and power quantities between Cases 5-7. Therefore, Figure 4.5 shows the total normal and chordwise forces scaled by the chord and also scaled by the number of blades, N_b. All of these cases are trimmed to the same thrust, therefore the area under the curve of the $N_b C_n M^2 c/R$ graph should be equal from case to case. The thrust values from these cases are within 11 N of the desired design thrust and the areas under the curve for the normal force all do appear to be equal.

Keeping in mind that Case 2 is the baseline case (ellipse planform, nominal RPM, and linear twist), Case 5 with a reduced RPM shows a decrease in Figure of Merit from the baseline case (0.715 vs. 0.726). The lift is moved inboard in Case

Table 4.3: Cases 5-7 CFD Aerodynamic Results

Case	Thrust (N)	Figure of Merit	Collective (deg.)
5	1,005	0.715	15.20
6	1,008	0.749	14.70
7	1,011	0.748	12.50

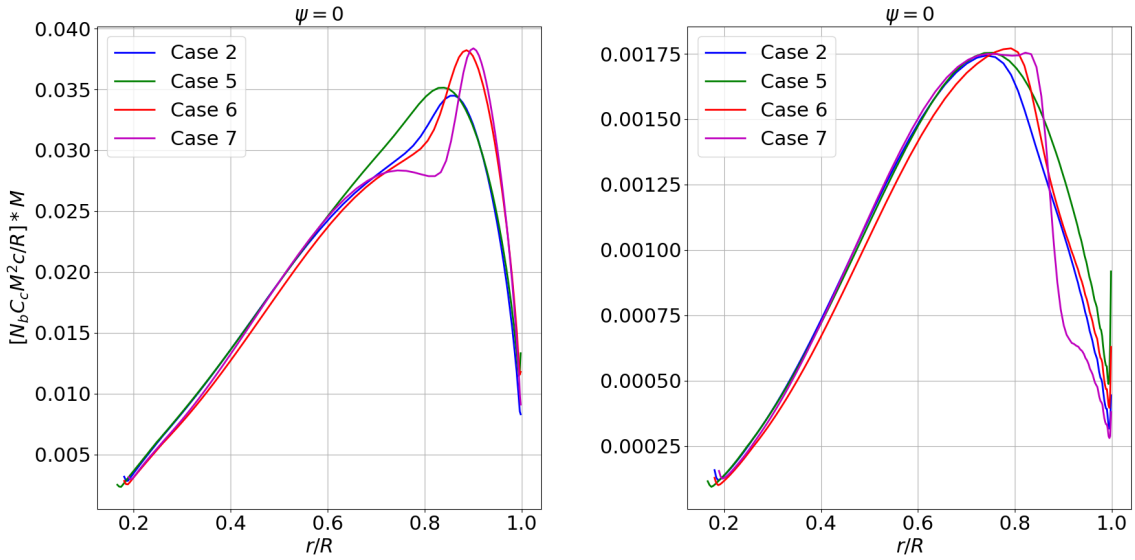

Figure 4.5: Cases 5-7 spanwise airloads at $\psi = 0°$

5, making it less efficient than the baseline case. Case 5 also has a higher in-plane loading at the tip compared to the baseline case. Since Case 5 had a lower RPM, more power was needed to acheive the same thrust. Case 6, with the lower RPM and three blades instead of two, shows an increase in Figure of Merit compared to the baseline case (0.749 vs. 0.726). Case 6 shows a noticeable decrease in chordwise loading inboard. Finally, Case 7 also shows an increase in Figure of Merit (0.748 vs. 0.726) with three blades and the nominal RPM. Both Cases 6 & 7 experience

more lift outboard near the tip, making these cases the most efficient. Most of these trends can be inferred by looking at Figure 4.5, but it is easier to see the differences in Figure of Merit trends by further scaling the chordwise force by the local Mach number. This can be seen in Figure 4.6.

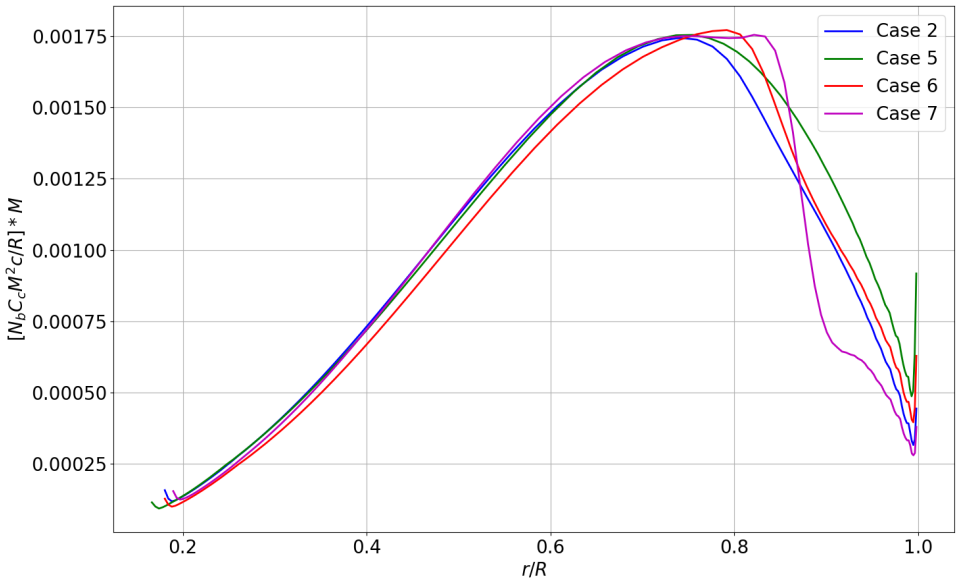

Figure 4.6: Cases 5-7 spanwise airloads at $\psi = 0°$ scaled by local Mach Number

By scaling by the local Mach number, it is easier to see the effect of RPM and the number of blades on the power between these cases and thus the Figure of Merit. The area under the curve is analagous to power and it is clear that Case 6 has the smallest area or smallest power consumption. This agrees with the fact that Case 6 contains the highest Figure of Merit, just slightly edging out Case 7 (0.749 vs. 0.748). When looking at Figure 4.5 above, it was not as clear if Case 6 or 7 had a smaller power consumption. Case 6 is slightly more efficient than Case 7, because the reduced RPM decreases the power consumption inboard, while the increased

blade count decreases the power consumption outboard. This subtlety can be seen when the chordwise force is further scaled by the Mach number.

The Figure of Merits obtained from BEMT for Cases 5-7 were compared to those obtained in CFD. The BEMT and CFD Figure of Merit results are shown in Table 4.4.

Table 4.4: Cases 5-7 CFD & BEMT Aerodynamic Results Comparison

Case	BEMT Figure of Merit	CFD Figure of Merit
5	0.856	0.715
6	0.873	0.749
7	0.858	0.748

Case 5 is once again the least efficient, when the RPM is soley reduced since it cannot acheive the same thrust as efficiently. Case 6 for BEMT shows a significant improvement over Case 7, unlike that seen in CFD, however, both BEMT and CFD predict that Case 6 is the most aerodynamically efficient. Therefore, BEMT is once again a valuable tool in predicting overall trends between propeller cases, while using CFD captures more of the subtleties between propeller cases.

Cases 8-11 used the boom geometry given by Aurora Flight Sciences and the aerodynamic results will be discussed in the next section. The rest of the isolated propeller test cases and their aerodynamic results will be presented here, with Cases 12-17.

Cases 12 & 13 investigated the effect of sweep. The amount of forward sweep was equivalent to that swept back for the aft sweep so the elliptic planform had a

straight trailing edge. In addition, a rectangular blade (Case 14) and 2:1 tapered blade (Case 15) were analyzed, to illustrate the effects of chord variation. Case 16 was the baseline propeller, except no longer run fully turbulent, to see how allowing a laminar region over the blade would decrease drag and thus increase aerodynamic performance. Finally, Case 17 increased the radius of the propeller, thus decreasing the disk loading. The Figure of Merit results for the remaining isolated propeller cases are outlined in Table 4.5.

Table 4.5: Cases 12-17 CFD Aerodynamic Results

Case	CFD Figure of Merit
12	0.730
13	0.719
14	0.711
15	0.718
16	0.744
17	0.736

The aft sweep illustrated an increase in Figure of Merit compared to the baseline case (0.730 vs. 0.726). This was as expected since the aft sweep alleviates the normal tip Mach number and pushes the lift outboard. The span-wise loads for Cases 12 and 13 as compared to the baseline case can be seen in Figure 4.7.

The forward sweep achieves the opposite of the aft sweep resulting in a lower Figure of Merit (0.719 vs. 0.726).

Cases 14 and 15 show a steady increase in Figure of Merit from the rectangular to 2:1 tapered blade. As the blade is tapered, the Figure of Merit increases slightly

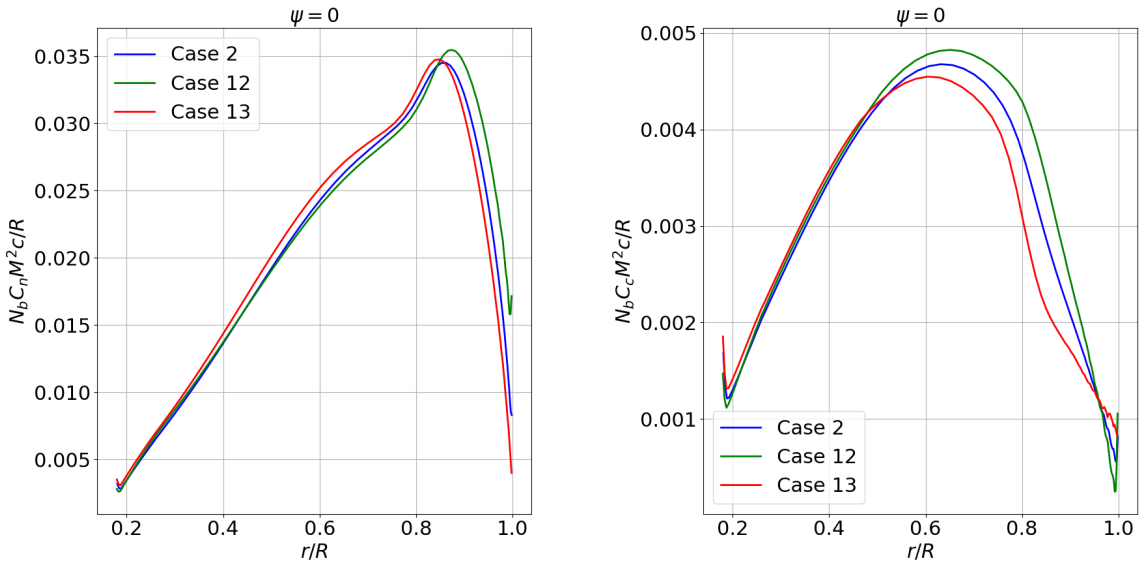

Figure 4.7: Cases 12 & 13 spanwise airloads at $\psi = 0°$

since the profile power decreases. The span-wise loads for Cases 14 and 15 compared to the baseline case are shown in Figure 4.8.

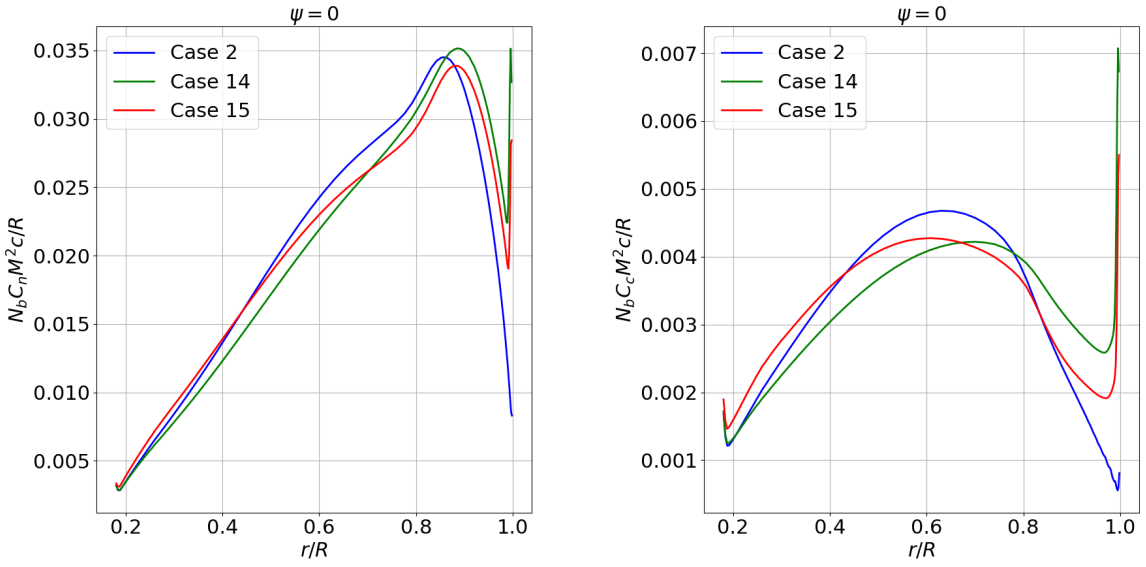

Figure 4.8: Cases 14 & 15 spanwise airloads at $\psi = 0°$

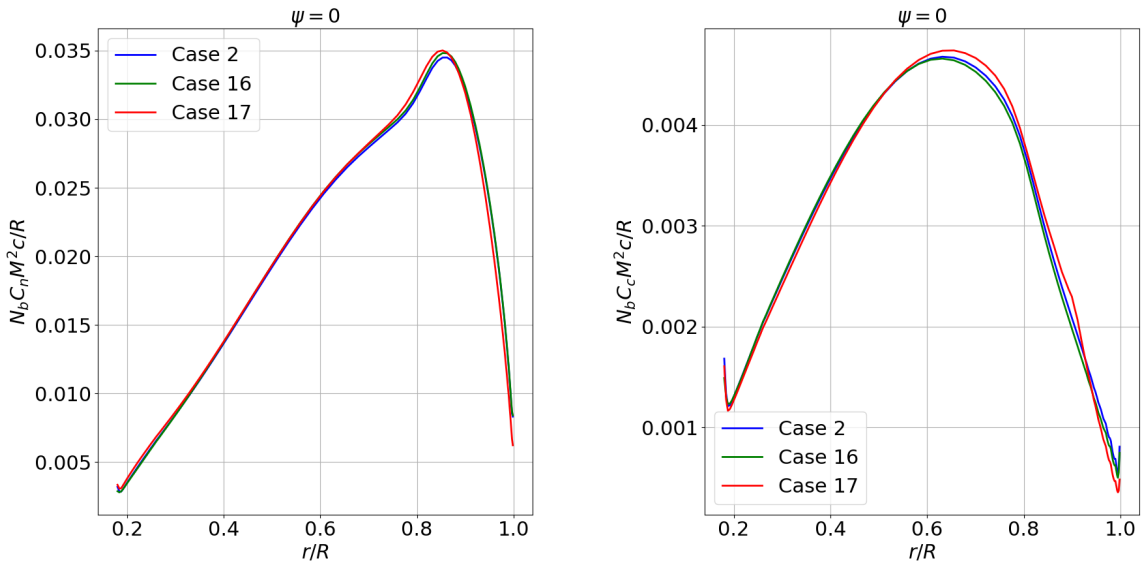

Figure 4.9: Cases 16 & 17 spanwise airloads at $\psi = 0°$

Case 16 shows a significant increase in Figure of Merit (0.744 vs. 0.726) due to the decreased drag from the transition model versus a fully turbulent case. Finally, Case 17 also shows an increase in Figure of Merit from the baseline (0.736 vs. 0.726). This makes sense since fundamentally from BEMT when disk loading is decreased, the Figure of Merit increases. The span-wise loads for Cases 16 and 17 compared to the baseline case are shown in Figure 4.9. The span-wise loads are very similar from case to case. Case 16 shows a consistent lower chordwise loading through out the length of the blade, while Case 17 shows a decrease in chordwise loading inboard, making these both more efficient than the baseline case, but with Case 16 being the most efficient.

The BEMT Figures of Merit were compared to those obtained from CFD in Table 4.6. It is noted that the BEMT Figure of Merit is not reported for Cases 12,

13, or 16, since the current BEMT model cannot be used to predict the aerodynamic performance of swept blades and does not have a transition model.

Table 4.6: Cases 12-17 CFD & BEMT Aerodynamic Results Comparison

Case	BEMT Figure of Merit	CFD Figure of Merit
12	N/A	0.730
13	N/A	0.719
14	0.797	0.711
15	0.820	0.718
16	N/A	0.744
17	0.873	0.736

For Cases 14 and 15, the BEMT and CFD Figure of Merits follow the same trend, showing a slight benefit in aerodynamic performance by tapering the blade as was first expected when choosing the baseline elliptic planform. As expressed above, Case 17 in both BEMT and CFD showed a significant increase in Figure of Merit by decreasing the disk loading. A longer blade will experience less loading and thus be more efficient.

After looking at the aerodynamic performance for the isolated propeller cases, the aerodynamic trends were all as expected when changing certain design parameters. The normal and chordwise loadings could then be fed into the acoustics code to analyze further how these various designs effect the acoustic performance. This is discussed in Chapter 5.

4.2 Propeller Test Cases with Boom Geometry

In reality, propellers do not run in isolation so a boom was placed underneath the propeller to analyze its effect on the aerodynamic performance since it would most likely result in a distortion of the wake being blown down by the propeller. Cases 8-11 & 18 included the nearby boom geometry and all boom cases were run to 12 revolutions. The wake structure for Case 8 with the boom placed 0.25R below is shown in Figure 4.10. The wake structure as predicted breaks down due to the presence of the boom. Case 10, with the aft swept propeller and the boom still placed at the 0.25R vertical distance results in no apparent difference in the wake structure. This makes sense since the boom placement is the same as Case 8, and the propeller geometry will not effect the distortion of the wake.

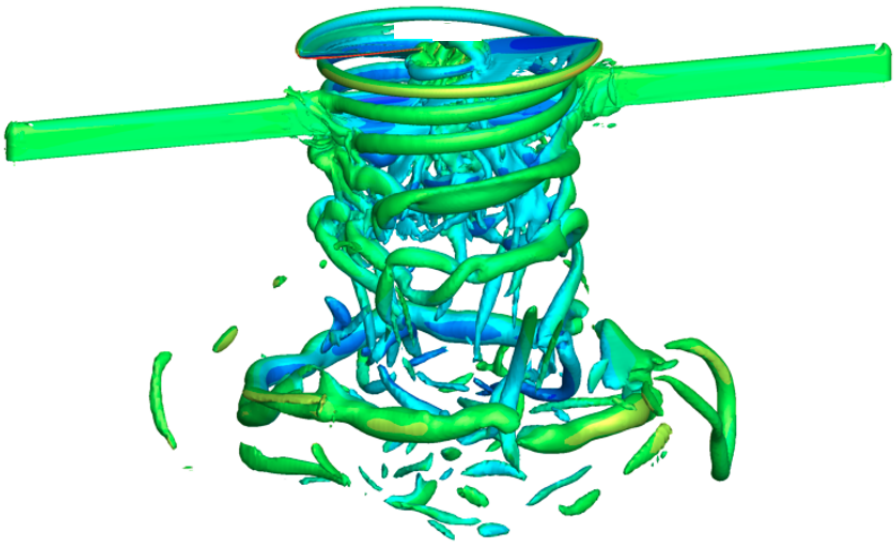

Figure 4.10: Case 8 wake structure

However, when the boom is placed further away the wake structure looks cleaner for a longer wake age than Case 8, but still eventually breaks down. The wake structure for Case 9 with the boom placed further away at 0.50R is shown in Figure 4.11. With the semi-infinite boom, the asymmetry also causes a distortion in the wake, shown in Figure 4.12.

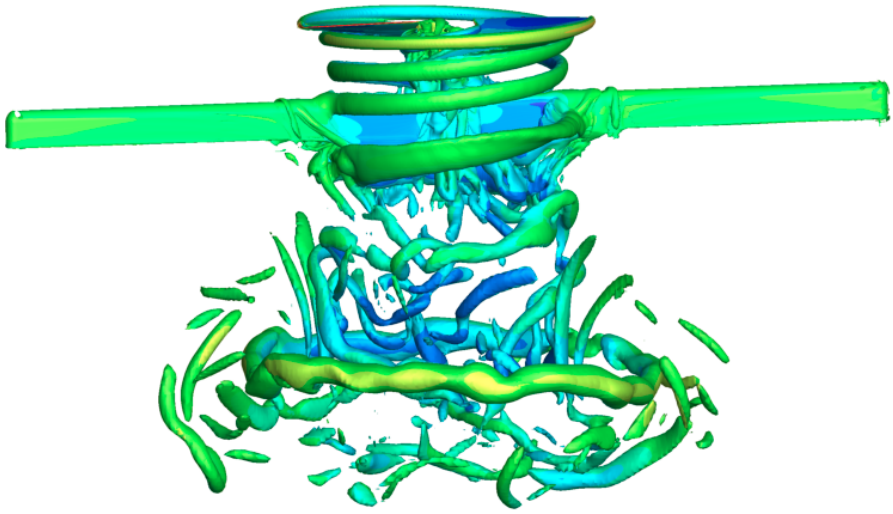

Figure 4.11: Case 9 wake structure

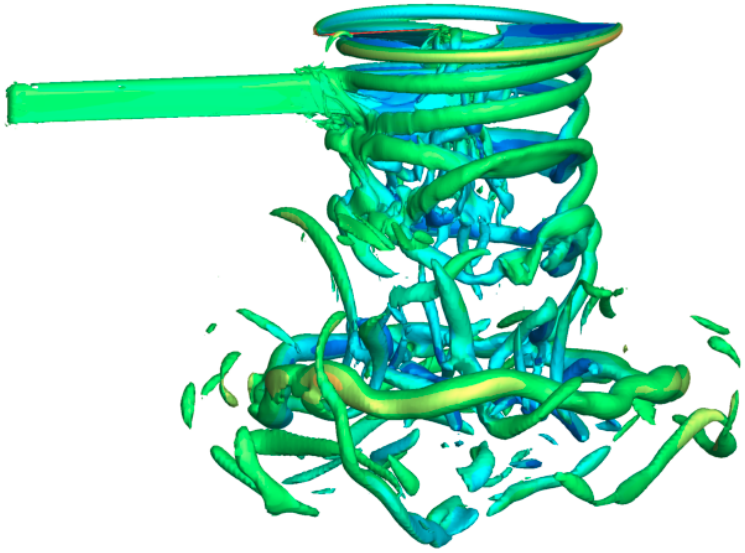

Figure 4.12: Case 11 wake structure

The span-wise loads scaled by $\frac{c}{R}$ are shown for Cases 8-11 in Figure 4.13. Slight deviations can be seen with these cases. The resulting Figures of Merit are shown in Table 4.7.

Table 4.7: Cases 8-11 CFD Aerodynamic Results

Case	Thrust (N)	Figure of Merit	Collective (deg.)
8	987	0.701	12.58
9	1,002	0.719	12.58
10	1,003	0.727	12.30
11	1,004	0.713	12.58

Interestingly, the most efficient case is Case 10 with the aft-swept propeller. Case 10 is more efficient than both Cases 9 and 11 when the boom is placed further away, or the boom is only semi-infinite. Case 10 is also more efficient than Case 8

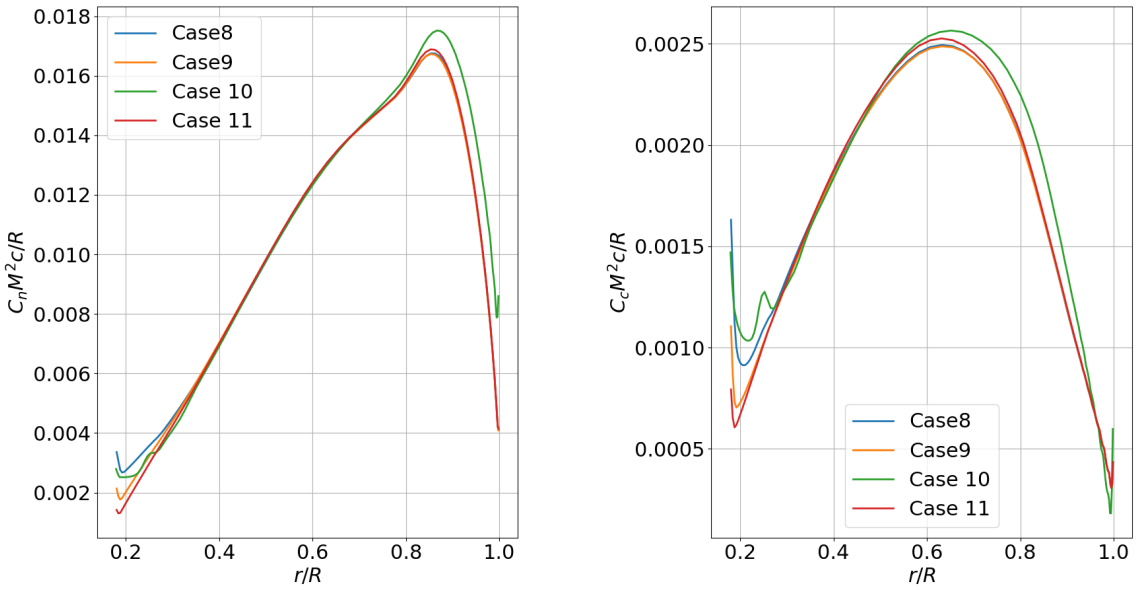

Figure 4.13: Cases 8-11 spanwise airloads at $\psi = 0°$

since the aft swept propeller causes the tip Mach number to be alleviated by the sweep causing less chordwise loading and the normal force to be pushed further outboard.

When investigating aft sweep with the isolated propeller cases it was shown that the Figure of Merit increased from the baseline case of 0.726 to 0.730. For those same reasons, the aft swept propeller implemented with the boom geometry is the most efficient of the boom cases. Case 8 with the boom placed at the same vertical distance, has a significant reduction in Figure of Merit from 0.727 of Case 10 to 0.701 - further proving the aft swept propeller superior to the baseline geometry. Case 10 is even slightly more efficient than the baseline case, Case 2, (0.727 vs. 0.726) even with the presence of the boom.

The rest of the Figure of Merit trends follow as expected as well. Case 8

is the least efficient case with the full boom closest to the propeller. Case 9 is slightly more efficient, but still less efficient than Case 2 without the boom (0.719 vs. 0.726). Looking at Cases 8 & 9, the Figure of Merit increases when the boom is placed further away. This is due to the fact that the wake structure is not as distorted from the boom's presence, allowing for less power loss. Case 11 lies in between Cases 8 and 9 since the semi-infinite boom should not be as detrimental to performance as the full boom since the wake is able to recover slightly on the side where the boom is not present. As the boom is placed further away, the propeller should become more efficient, which is true. Cases 8, 9, and 11 are all less efficient than the baseline case without any boom presence.

Therefore, it can be concluded that the further away the boom is placed the more aerodynamically efficient the propeller will be. However, implementing aft-sweep significantly stabilizes the aerodynamic performance by keeping the Figure of Merit very close to the baseline case without the boom presence. The Figure of Merit decreases from the baseline case of 0.726 to 0.701 when the boom is placed 0.25R away, which is a notable difference, but not substantial to cause concern for the aerodynamic performance of the eVTOL vehicle. This is encouraging since vehicles like the Boeing PAV seem to have the nearby boom geometry placed at the closer vertical separation of 0.25R.

In order to see how the sectional loads were changing in time, the normal and chordwise forces $C_n M^2$ and $C_c M^2$ at 0.85R were plotted vs. azimuth. This is shown in Figure 4.14.

There is significant fluctuation of the sectional loads in time, with the Case

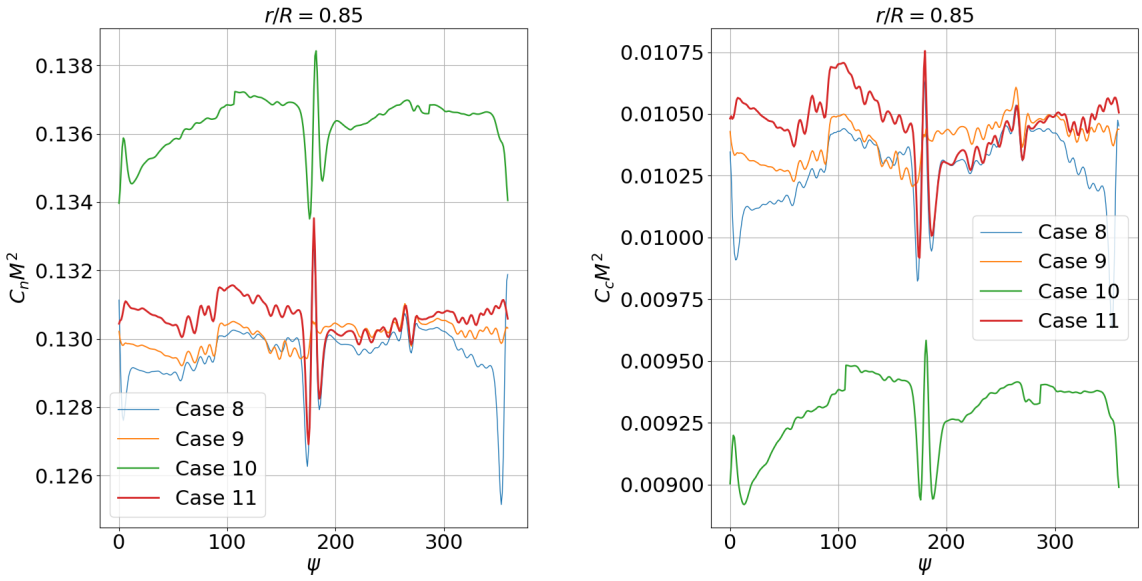

Figure 4.14: Cases 8-11 airloads time variation

10 signature being the cleanest. The largest fluctuation occurs every 180° when the propeller blade passes over the boom geometry.

The unsteadiness of the blade was also analyzed by looking at the variation of thrust in time, which can be seen in Figure 4.15. The thrust coefficient varies by only about 2% in time. This suggests that the unsteadiness from the boom is not substantial, which makes sense since the Figures of Merit for Cases 8-11 do not vary drastically when the boom is present.

The time-averaged sectional force (in the +Z direction) was computed for the boom and is shown in Figure 4.16. This was computed to analyze the downward force on the boom. The span of the boom is defined from -3R to 3R (total of 6R). The semi-infinite boom is defined from -3R to 0. It is shown that the normal force is maximum near ± 1R. This normal force, C_nM^2 along with the chordwise force,

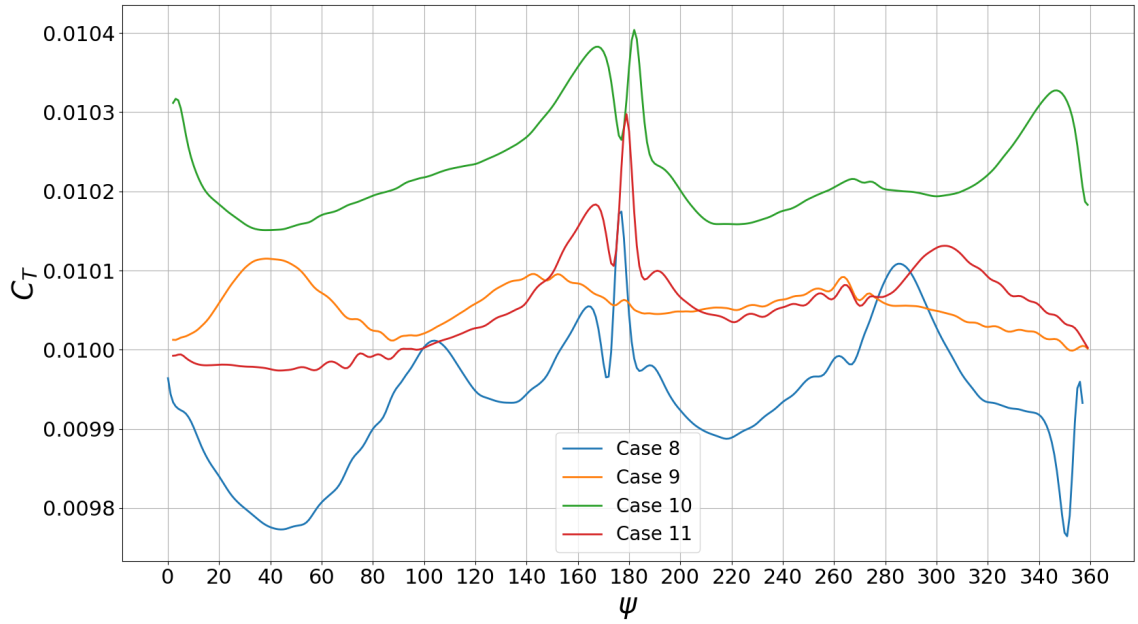

Figure 4.15: Thrust time history of boom cases

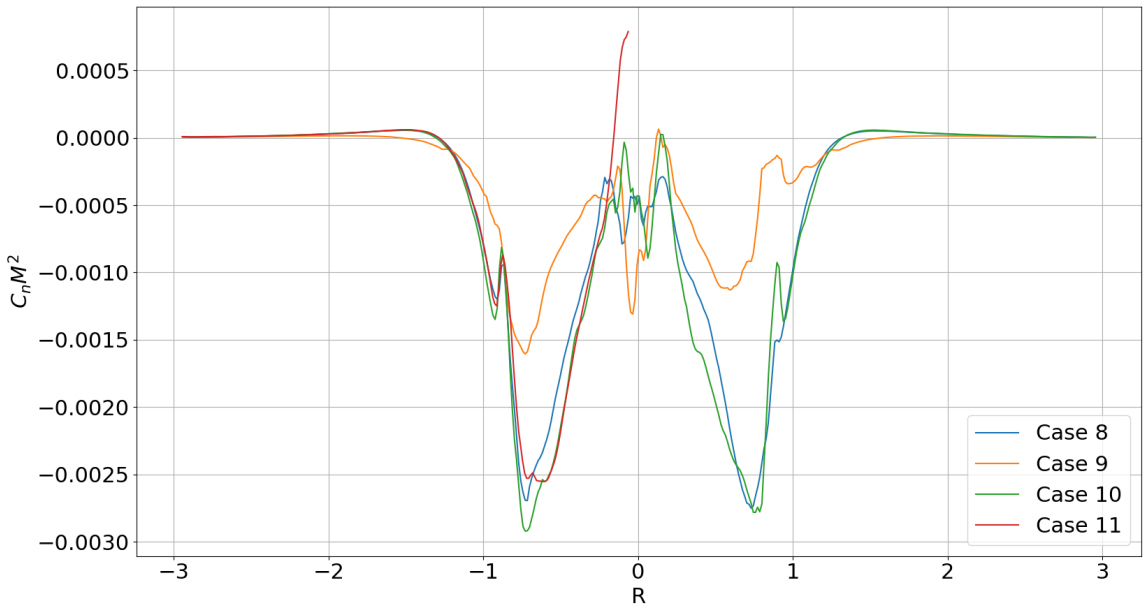

Figure 4.16: Time-averaged sectional normal force on boom

$C_c M^2$, can be used to calculate the acoustics due solely to the boom's presence and is discussed in Chapter 5.

Finally, the integrated force over the boom as a function of time was investigated. GARFIELD outputs a force in the z-direction in CFD units. This force was non-dimensionalized by the Mach number and area of the boom since it would be hard to quantify the CFD units. The integrated force over the last 1.5 revolutions is shown in Figure 4.17. The normal force is negative, indicating the downward direction, and is maximum every 180 °, which corresponds with each blade passage over the boom. It is also noted that the maximum force is fairly consistent over time for Cases 8-11.

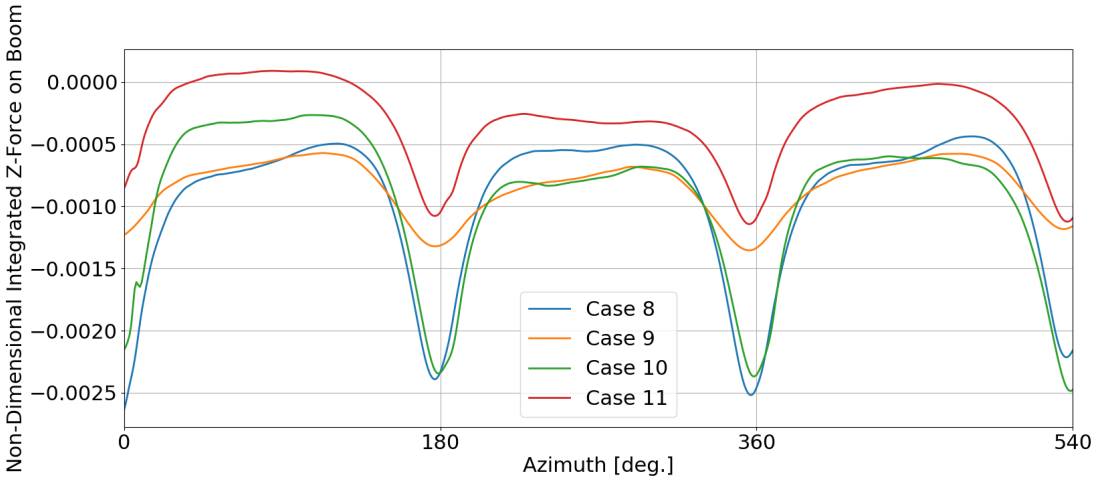

Figure 4.17: Integrated normal force on boom time history for Cases 8-11

The final boom case that was analyzed was when the boom was canted at an angle of 10°. The Boeing PAV aircraft appears to have all its propellers canted at an angle, possibly for stability purposes. This was investigated to see the aerodynamic

impacts of this cant angle. The 12 revolution solution for the canted boom case, Case 18, is shown in Figure 4.18.

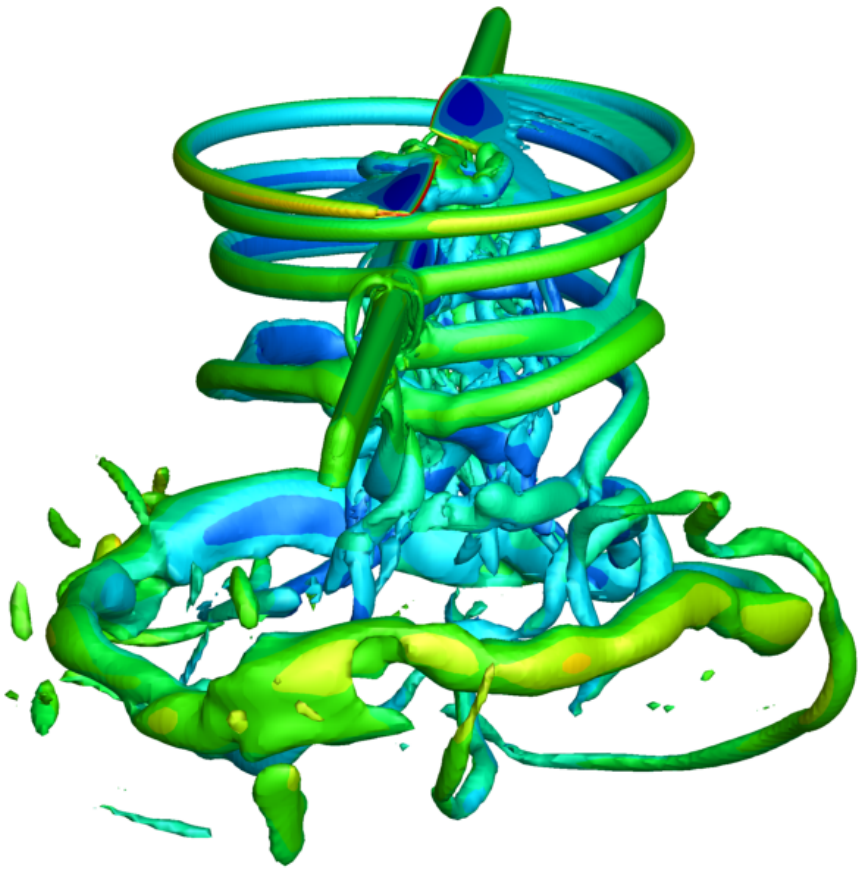

Figure 4.18: Case 18 wake structure

Since the only difference between this case and Case 8 was the cant angle of the boom, the sectional airloads of Case 18 were compared with Case 8 and is shown in Figure 4.19. It can be seen that Case 18 is ever so slightly less efficient than Case 8 due to the small increase in chordwise loading over the majority of the span of the

propeller blade.

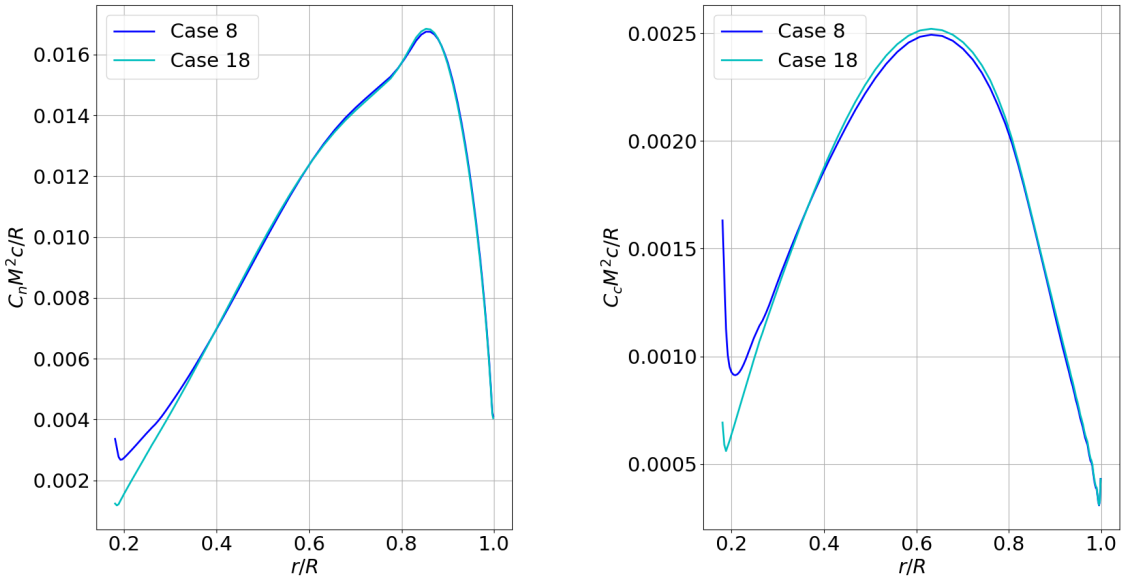

Figure 4.19: Case 8 & 18 sectional airloads

The Figure of Merit for Case 18 as compared to Case 8 is shown in Table 4.8. When the boom is canted, the Figure of Merit decreases a negligible amount from 0.701 to 0.695. This is good news since the propellers on the Boeing PAV seem to be canted for stability of the aircraft, and the cant angle seems to not have a substantial effect on the aerodynamic performance of the propeller.

Table 4.8: Cases 8 & 18 CFD Aerodynamic Results

Case	Thrust (N)	Figure of Merit	Collective (deg.)
8	987	0.701	12.58
18	985	0.695	12.58

By looking at the time-averaged sectional force (in the +Z direction) on the

boom for Cases 8 & 18, seen in Figure 4.20, the downward force on the boom is slightly larger when the boom is canted.

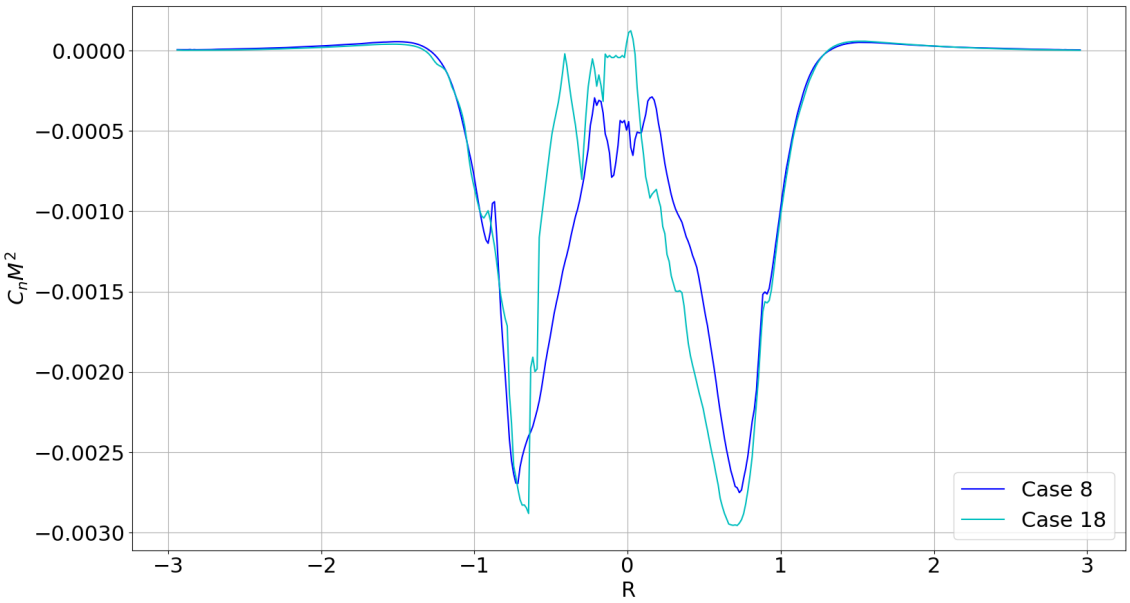

Figure 4.20: Case 8 & 18 time-averaged sectional normal force on boom

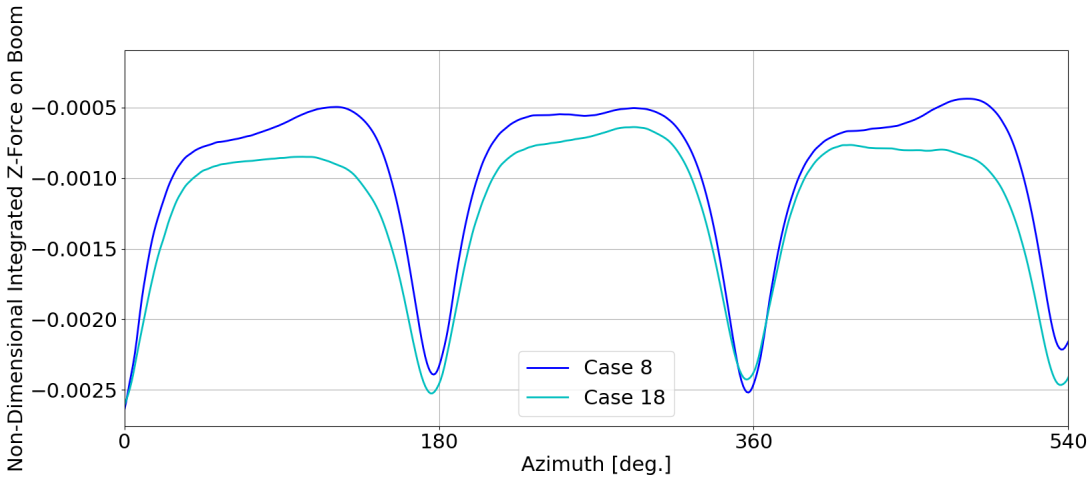

Figure 4.21: Integrated normal force on boom time history for Cases 8 & 18

Figure 4.21 shows the integrated normal force on the boom over time for Cases 8 & 18. It can be seen again that the normal force on the boom for Case 18 when the boom is canted is slightly larger than when the boom is not canted. The normal force is also maximum every 180° and the maximum force is fairly consistent over time as before with Cases 8-11.

The downward force on the boom was then factored in for the design thrust of 1,000N because in reality that downward force would result in the propeller thrust to be slightly less than 1,000N. In order to report the true aeroacoustic performance for the propeller to produce a thrust of 1,000N all boom cases were re-trimmed adjusting the collective to account for the downward force on the boom. By using the non-dimensional normal downward force on the boom, it was found that the force was contributing about 50-80 N of downward thrust, decreasing the propeller thrust by 5-8%. Once this was factored in, the resulting Figure of Merits shown in Table 4.9, illustrated a minimal difference from their original values.

Table 4.9: Cases 8-11 & 18 CFD Re-trimmed Aerodynamic Results

Case	Original Figure of Merit	Re-trimmed Figure of Merit
8	0.701	0.697
9	0.719	0.716
10	0.727	0.724
11	0.713	0.709
18	0.695	0.693

All of the previously described trends remain the same, just with the aerodynamic peformance slightly lower than what was originally reported as the propeller

was not as efficient operating at a higher collective. This also implies that the acoustic results will not vary significantly when factoring in the normal force from the boom.

While the boom presence decreases the aerodynamic performance with or without canted propellers, it does not affect the aerodynamic efficiency by a huge amount nonetheless, the resulting acoustics were analyzed to see if the boom had a large impact on the noise and if this should be of concern.

Chapter 5: Acoustic Results

5.1 Isolated Propeller Test Cases

The normal and chordwise forces, C_nM^2 and C_cM^2, were obtained by GARFIELD at 95 spanwise points along the blade, which were then input into ACUM and ultimately changed to pressure fluctuations via the FWH equation. Since BEMT was a successful method for predicting aerodynamic performance trends quickly, the airloads obtained from BEMT at 42 spanwise locations along the blade were used as quick predictions for acoustic results. Once the CFD cases had been run, the SPL in dB as a function of elevation angle was compared to that obtained by BEMT. As discussed in Chapter 2, observer locations were placed at various elevations, every 5°, at a radius of 50m. For the isolated propeller cases the acoustics will not vary in time since the sectional loads remain the same regardless of azimuth position of the blades. Since the spanwise loads were constant when varying azimuth, the elevation angle was the only contributor to the magnitude of SPL.

Figure 5.1, shows the SPL in dB as the elevation angle changes. The main concern is with the noise below the propeller (thus negative elevation angles) since this is mostly likely where an observer would be located. The dotted lines represent the BEMT acoustic results and the solid lines represent the CFD acoustic results.

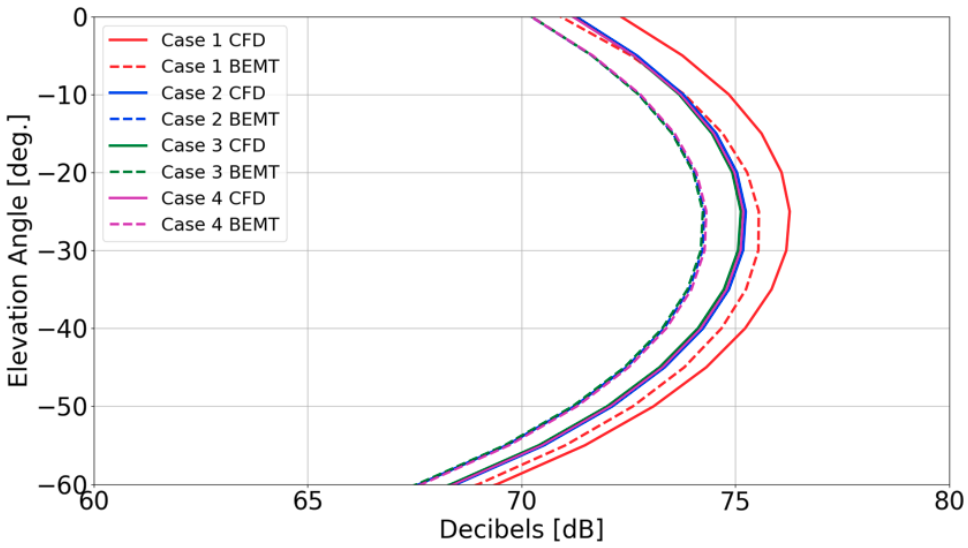

Figure 5.1: Cases 1-4 CFD & BEMT SPL as a function of elevation angle

There is a consistent 1-2 dB shift from the BEMT to CFD acoustic results. This is expected since BEMT is often optimistic, predicting smaller in-plane loads as compared to CFD. Since CFD predicts larger loading, the OASPL will be higher than that predicted by BEMT. A 1-2 dB difference between these two methods is reasonable taking into account the limitations of the BEMT model. The overall trends between Cases 1-4 were kept between BEMT and CFD. Both BEMT and CFD show that changing an untwisted blade (Case 1) to a linearly twisted blade (Case 2) gains some acoustic benefit, by decreasing the maximum SPL about 1 dB. However, Figure 5.1 shows that there is no discernable difference in the acoustic levels when the twist at the tip of the blade is modified (Cases 3 & 4 compared to Case 2). This suggests that bi-linear twist rates have a negligible impact on the noise.

Table 5.1: Cases 1-4 CFD & BEMT OASPL Results

Case	Figure of Merit	BEMT OASPL (dB)	CFD OASPL (dB)
1	0.679	75.55	76.27
2	0.726	74.27	75.24
3	0.730	74.24	75.13
4	0.724	74.32	75.19

The maximum OASPL in dB from BEMT and CFD, which is equivalent to the SPL 25° below the propeller, for Cases 1-4 are shown in Table 5.1 along with their Figure of Merit values. Out of Cases 1-4, Case 3 with the increased twist rate at the tip is the most efficient both aerodynamically and acoustically. However, it is only more efficient by 0.004 in Figure of Merit and 0.11 dB in OASPL when compared to the baseline case - both of which are considered negligible differences. A human would not be able to tell the difference of only 0.11 dB, and a hover efficiency improvement of 0.004 would not be something actually considered in designing a propeller blade.

Therefore, the bi- linear twist rates have a negligible impact on OASPL and should not be considered as a design parameter to increase the aeroacoustic performance. By simply adding twist to the blade as mentioned above the OASPL drops by about 1 dB for both BEMT and CFD. Since a propeller blade is usually always twisted, this is not a particularly valuable conclusion since this design parameter would be used in almost every propeller blade manufactured. The acoustic results for Cases 1-4 suggest that twist only be used to help the aerodynamic performance since it will not have a significant negative or positive effect on the noise.

The results for Cases 5-7 exploring RPM and number of blade changes as compared to the baseline case are in Figure 5.2 with BEMT represented as the dotted lines and CFD as the solid lines.

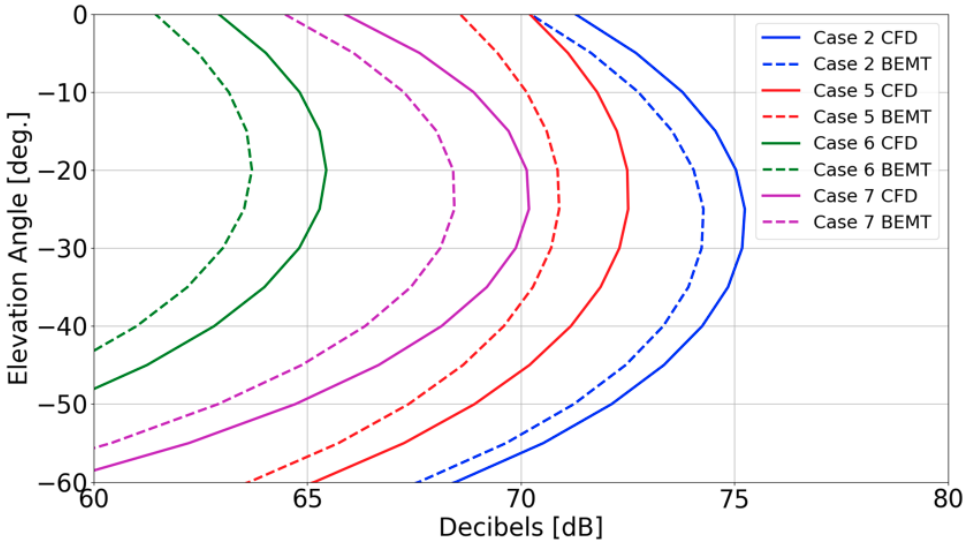

Figure 5.2: Cases 5-7 CFD & BEMT SPL as a function of elevation angle compared to the baseline case, Case 2.

Immediately it can be observed that both design parameters have a more promising impact on the noise. The quietest propeller design was Case 6, where both of these design parameters were combined by increasing the blade count and dropping the RPM. It becomes apparent that increasing the number of blades and decreasing the RPM benefits the acoustic performance much more than geometric changes like twist for Cases 1-4. The maximum OASPL in dB for Cases 5-7 are shown in Table 5.2.

Case 6 shows about a 10 dB improvement from the baseline case. Case 5, which just reduced the RPM, results in about a 3 dB improvement while Case 7, which

Table 5.2: Cases 5-7 CFD & BEMT OASPL Results

Case	Figure of Merit	BEMT OASPL (dB)	CFD OASPL (dB)
5	0.715	70.89	72.51
6	0.749	63.70	65.44
7	0.748	68.44	70.19

just increased the number of blades shows about a 5 dB improvement. Therefore, these design parameters are very useful in reducing the OASPL experienced by an observer and should be implemented when concerned with aeroacoustic performance. There is a potential of decreasing the OASPL by 10 dB when combining these design parameters. The BEMT acoustic results are again shifted down by 1-2 dB, which is consistent with the results from Cases 1-4. Case 6, which was the most aerodynamically efficient of the isolated propeller cases is the most acoustically efficient. While Case 6 and 7 only vary by 0.001 in Figure of Merit, their acoustic signatures vary by about 5 dB. This is due to the reduced RPM from Case 7 to Case 6, causing the pressure fluctuations to not happen as quickly, resulting in quieter noise. It is no surprise that the most efficient case aerodynamically, is the most efficient case acoustically. This is due to the fact that the airloads are smaller, which contribute to the smaller power consumption, higher Figure of Merit, and then smaller pressure fluctuations and decreased noise. For all of these cases it can be seen that the maximum SPL, or the OASPL occurred at an elevation 25° below the propeller.

A polar directivity plot was also created for isolated propeller Cases 12-17 and

is shown in Figure 5.3. Again, the maximum SPL occured 25° below the propeller. When comparing Cases 12-17 with the baseline case, the reduced disk loading, Case 17, has the best acoustic performance with a reduction of about 2 dB. Case 17 also resulted in an improvement of aerodynamic performance. Therefore, reduced disk loading (in this instance increased radius) should be a design parameter of interest for a slight increase in aeroacoustic performance. Spatial requirements may limit how large the radius of the propeller can be however, which is why this design parameter was investigated last. The Boeing PAV aircraft does not allow much room for the propellers to have a larger radius. If acoustics was a concern, the vehicle's design could be altered to fit a larger propeller, but a decrease of about 2 dB in OASPL may not be worth it.

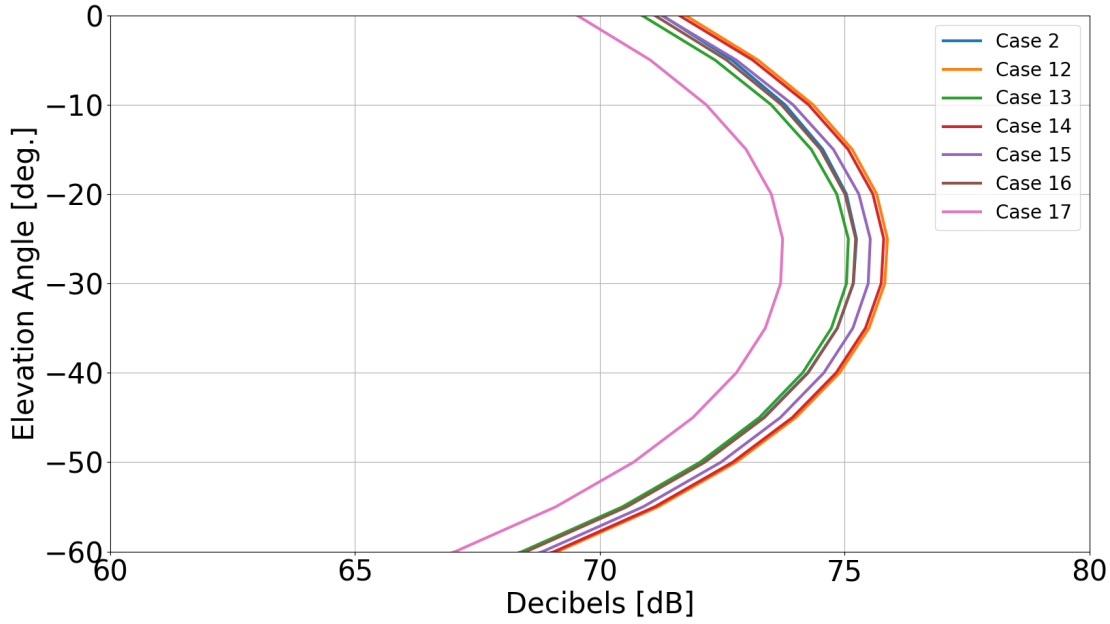

Figure 5.3: Cases 12-17 CFD SPL as a function of elevation angle compared to the baseline case, Case 2.

All other cases when compared to the baseline case resulted in small perturbations in the noise. While the aft swept propeller, Case 12, showed an improvement in aerodynamic performance, the aft sweep actually resulted in a slight increase in noise (less than 1 dB). This is most likely because of a concept called the acoustic planform. The acoustic planform is defined as the locus of points of contributing sources that arrive simultaneously to the observer [14]. In hover the acoustic planform is swept back and the aft sweep of the propeller may be more aligned with the acoustic planform. This may result in the weaker sources of noise for the aft swept propeller arriving at more nearly the same time at the observer than for the unswept blade.

The forward swept propeller had shown a decrease in aerodynamic performance, but indicates a slight benefit to the noise, since the sources of noise all arriving at the observer at the same time may be alleviated due to the forward sweep combating the acoustic planform. However, implementing a forward swept propeller does not impact the noise a significant amount, and arguably an observer won't be able to hear the difference between the forward sweep, aft sweep, or unswept blade since they are all within 1 dB of each other. This indicates that the design parameter of sweep may not be optimal to minimize noise, but can be used to make the aircraft aerodynamically more efficient.

The rectangular and 2:1 taper planforms (Cases 14 and 15), show higher OASPL's than the baseline elliptic planform as expected. The elliptic planform decreases the noise less than 1 dB from the rectangular planform, therefore, the design parameter of taper is also not promising when trying to minimize noise levels.

Finally, Case 16 shows the slightest improvement from the baseline case (difference of about 0.02 dB) when transition modeling was used. The drag was decreased by allowing laminar flow over a region of the blade, but since the sources of noise coming from drag are much smaller than the normal forces, the decrease in drag barely impacted the noise level. This suggests that the majority of the simulations run fully turbulent are adequate when predicting noise levels since transition modeling had no significant effect.

The maximum OASPL for Cases 12-17 are shown in Table 5.3 including the OASPL obtained from the BEMT results for complete comparison. There are no BEMT values reported for Cases 12, 13, or 16 because the BEMT analysis does not include a sweep parameter or transition modeling.

Table 5.3: Cases 12-17 CFD & BEMT OASPL Results

Case	Figure of Merit	BEMT OASPL (dB)	CFD OASPL (dB)
12	0.730	N/A	75.88
13	0.719	N/A	75.08
14	0.711	74.99	75.80
15	0.718	74.52	75.53
16	0.744	N/A	75.22
17	0.736	72.11	73.73

Once again the BEMT trends match the CFD trends, giving BEMT an optimistic 1 dB prediction. Therefore, it appears that reducing the disk loading is the most promising acoustic result when analyzing Cases 12-17. Taper, transition modeling, and sweep all exhibit negligible effects on the acoustic performance, decreasing

or increasing the OASPL by less than 1 dB.

Instead of solely looking at the dB levels for all these cases, a FFT analysis was used to apply A-weighting to the dB levels at various frequencies. The A-weighted OASPLs were computed to compensate for the relative loudness perceived by the human ear. Some acousticians prefer to look at the dBA levels for this reason. The A-weighted OASPL results are simply another way of looking at the same acoustic results outlined above. The acoustic time history was broken down into dB levels at different frequencies and then summed up into an OASPL in both dB and dBA. The more detailed procedure for finding the OASPL in dBA was discussed in Chapter 2. The FFT analysis for the baseline case is shown in Figure 5.4.

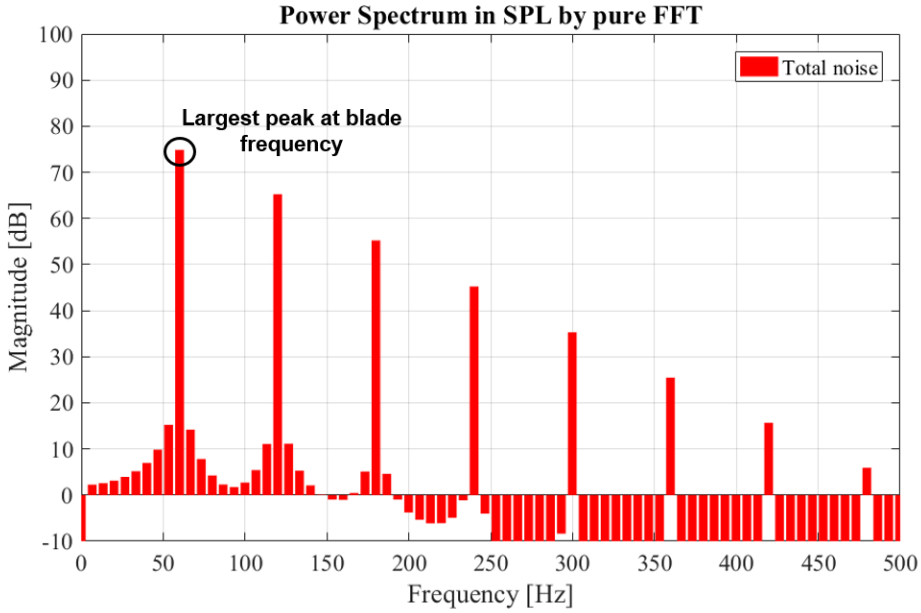

Figure 5.4: FFT analysis showing dB levels at various frequencies for the baseline propeller case

The largest peak occurs at the blade frequency of about 60 Hz, which is the

dominant frequency seen by the propeller. The dB levels slowly diminish at the higher frequencies. When the dB values are summed up, the maximum SPL at the blade frequency ends up becoming the OASPL. This is the noise level that is used to compare the propeller cases to one another, being careful to take into account the effect that higher frequencies may have on the noise levels. Since no broadband noise was included in the predictions (only tonal due to fluctuating airloads) the magnitude drops off rapidly with frequency. Since the noise was found to be mostly coming from lower frequencies for all of these propellers, the A-weighted OASPLs mostly followed the same trend as that without A-weighting.

This is more clearly shown in Figure 5.5 for Cases 1-7 with the dB and dBA values of the OASPL included.

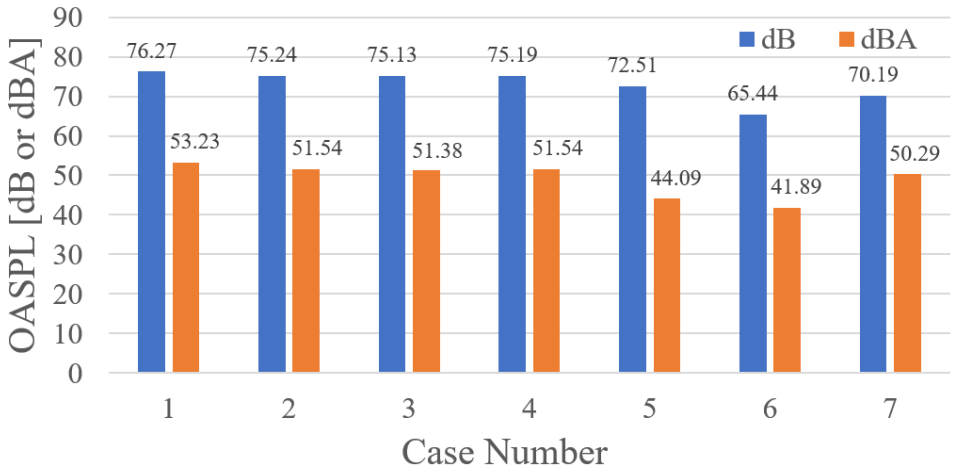

Figure 5.5: OASPL (dB & dBA) at 25° below the propeller for Cases 1-7

Case 6 still illustrates the largest impact on minimizing the noise of the aircraft by reducing RPM and increasing the number of blades when measured in both dB and dBA. This identifies both RPM and the number of blades as main drivers for

improving aeroacoustic performance. The ideal minimization in noise seems to be acheived when both of these design parameters are utilized. Cases 1-4 still show negligible differences, indicating that twist is not a design variable to help minimize noise.

The A-Weighted OASPL was also computed for Cases 12-17 and is shown in Figure 5.6. Here it is interesting to note that the dBA values do not always follow the same trends as the dB values.

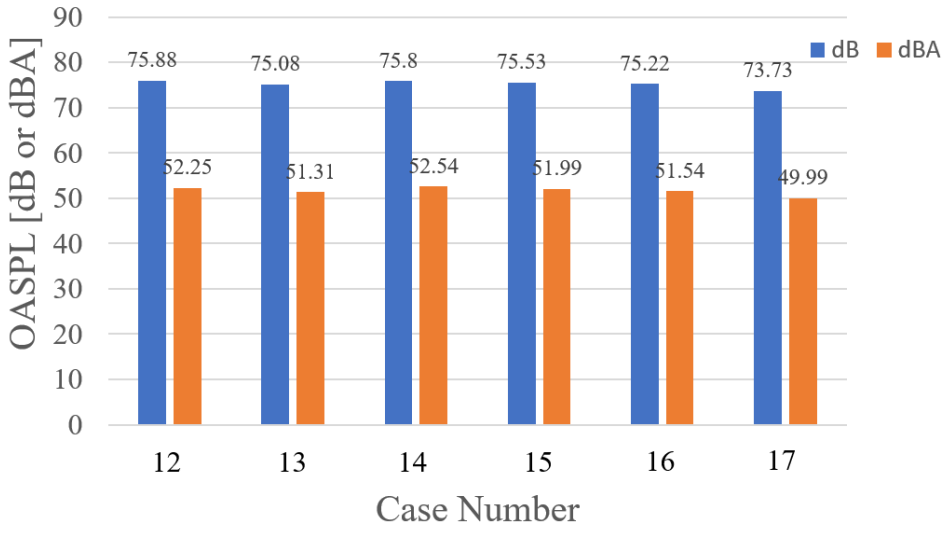

Figure 5.6: OASPL (dB & dBA) at 25° below the propeller for Cases 12-17

For example, Cases 12 and 14 show OASPL of 75.88 dB and 75.80 dB. In this instance, Case 14 has a lower OASPL, but when looking at the A-weighted OASPL, Case 14 is actually slightly higher (52.25 dBA vs. 52.54 dBA). Lower frequency content contributes to a higher A-Weight value and thus decreasing the noise by a larger amount. Therefore, cases that contain more high frequency content will appear louder than others. This means Case 14 has slightly more high frequency

content in its pressure time history signal than that of Case 12. This is precisely why acousticians like to also see dBA levels since it takes into account all frequencies seen by a pressure time history signal.

Since the same overall acoustic trends from CFD for these isolated propeller cases were captured by BEMT, it is further validation that these results are accurate. BEMT can be a valuable resource in quickly predicting aerodynamic performance and acoustic performance, but keeping in mind that both will generate generous results as compared to reality. However, capturing the overall trends is of great importance to quickly change design parameters to see the acoustic effects, while then checking the true magnitude of these trends in a higher fidelity solver such as CFD.

An investigation of the nearby boom geometery and its effects on the acoustics was performed since in reality, propellers do not operate in isolation.

5.2 Propeller Test Cases with Boom Geometry

For Cases 8-11 & 18 the OASPL was computed at different azimuth locations as well as different elevations. Each boom case was evaluated at various elevations below the rotor to see which elevation the OASPL was maximum. The results of Case 10 are shown in Figure 5.7 where the brown line corresponding to 25 degrees below the rotor shows the maximum OASPL. This is as expected because the isolated propellers maximum OASPL occured at 25 degrees below the rotor and then decreased as the elevation became more negative, which is also observed in Figure

5.7. However, with the boom present the sound level changes with azimuthal position. For the isolated propellers the lines in Figure 5.7 would be constant, but now the noise is varying in time due to the unsteady loads as a result of the boom. For Case 10, the maximum OASPL is located at 25 degrees below the rotor at an azimuth location of 340 degrees.

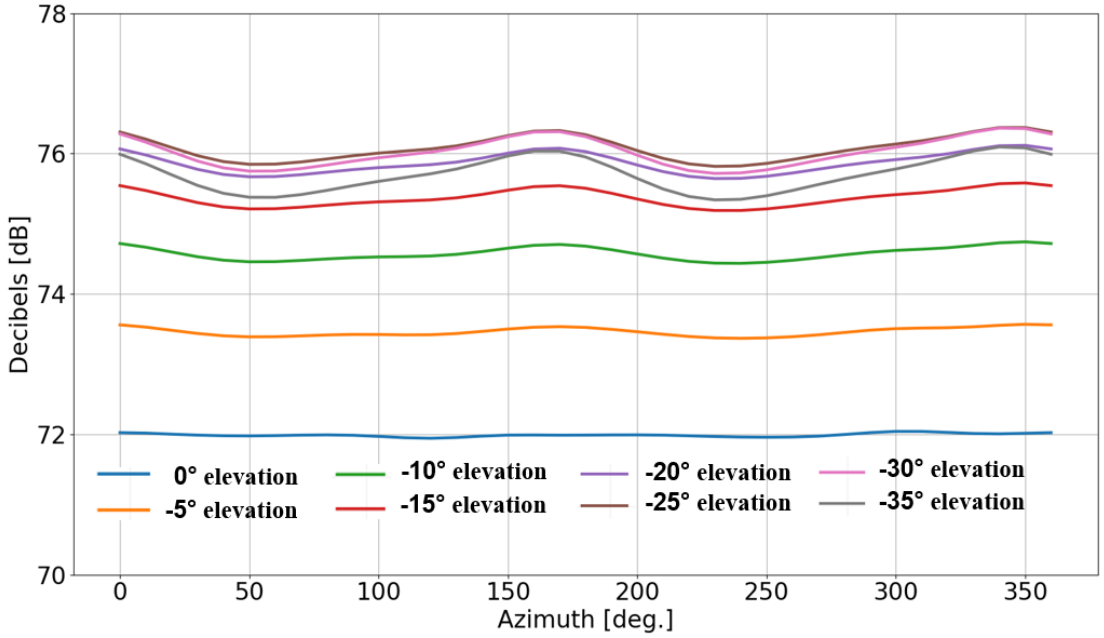

Figure 5.7: Acoustic results for Case 10 at various elevations below the propeller

To further illustrate the difference in noise from the isolated propeller cases to the boom cases, a pressure time history signal of the baseline case, Case 2, is shown against boom cases 8, 9, and 11 in Figure 5.8 for an observer 25 degrees below the propeller. The pressure fluctuations can be seen, which deviate from the isolated propeller signal, with the maximum pressure experienced higher for all the boom cases as compared to the isolated propeller. When the boom is placed further away,

Case 9, the pressure fluctations are significantly less than both Cases 8 and 11. Case 10 was not included in Figure 5.8 since a comparison was being made between the baseline propeller geometry and the type and location of the boom with the same propeller, which Case 10 implemented an aft swept propeller.

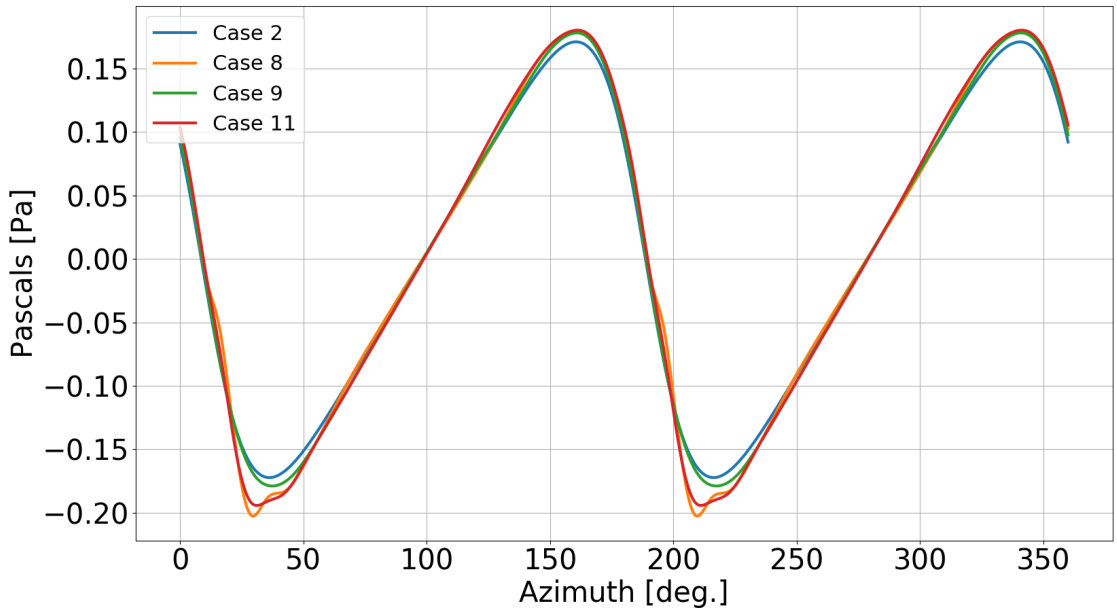

Figure 5.8: Pressure time history comparison of the baseline, isolated propeller to the boom cases

Since the maximum OASPL was found to be located 25 degrees below the propeller, Cases 8-11 & 18 were evaluated at this point of interest and the results are shown in Figure 5.9. Case 9, where the boom is placed furthest away at 0.50R, shows the least amount of variation of noise in time. This makes sense since the boom is placed farther away causing less pressure fluctuations. Case 8 experiences louder noise levels than Case 9 since the boom is placed closer creating more pressure fluctuations. Case 11 shows higher noise than both Case 8 and 9, since the

asymmetry of the semi-infinite boom causes an impulsiveness as the blade rotates over the boom and then not over the boom. The difference in pressure levels from when the blade is over the boom versus not over the boom most likely causes Case 11 to experience higher noise than even Case 9 when the full boom is placed further away. Case 10 shows the highest noise when the boom is located at 0.25R and the propeller is swept back. Finally, Case 18 shows larger pressure fluctuations than Case 11, resulting in a slightly higher noise. The canted boom must be resulting in larger differences in airloads since the boom is no longer parallel underneath the propeller.

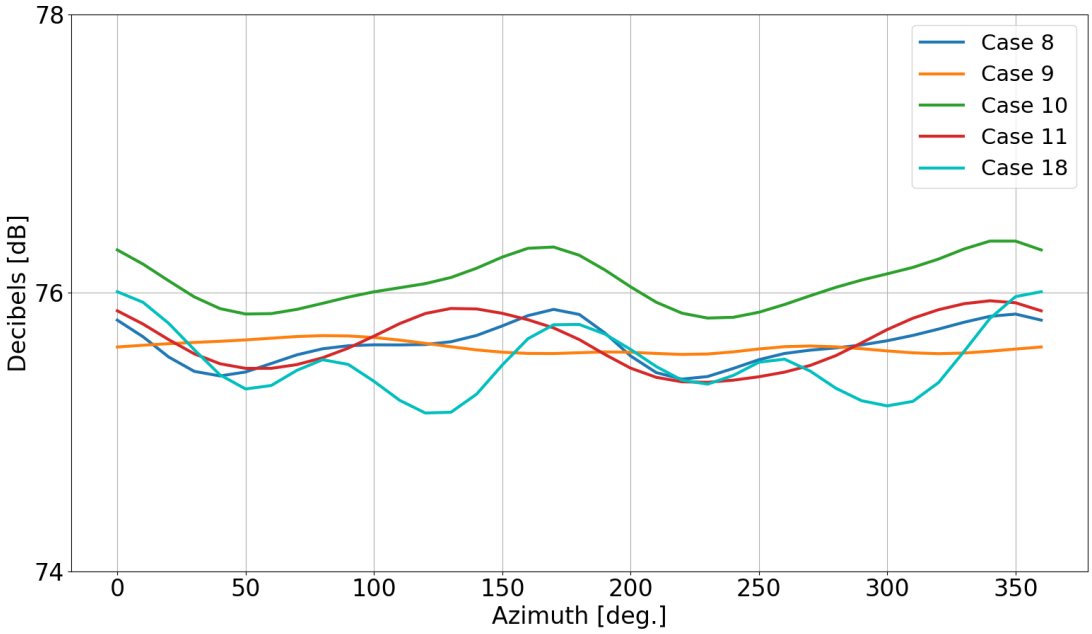

Figure 5.9: Cases 8-11 acoustic results vs. azimuth location

The maximum OASPL for these cases and the azimuth location where this occurs is shown in Table 5.4.

Table 5.4: Cases 8-11 & 18 CFD OASPL (dB & dBA) Results

Case	CFD OASPL (dB)	CFD A-Weighted OASPL (dBA)	Azimuth Location
8	75.88	53.51	170°
9	75.69	51.96	80°
10	76.37	53.24	340°
11	75.94	52.71	340°
18	76.01	54.39	360°

All boom cases result in a higher OASPL when compared to the baseline case, Case 2 of 75.24 dB. This makes sense since the unsteady loads from the boom's presence will cause more pressure fluctuations and thus more noise. The boom placement, cant angle, or type of boom did not show a significant variation in the maximum OASPL. Placing the boom further away only decreased the noise by about 0.2 dB, and the semi-infinite boom only increased the noise by about 0.06 dB, both of which would be negligible to an observer. When the boom was canted and still placed at the nominal vertical distance of 0.25R, the noise only increased by about 0.13 dB. This is good news since it appears the boom presence, type, or placement, have minimal effect on both the aerodynamics and acoustics.

In order to ensure that the unsteady loads were properly represented in time and that the OASPL was predicted as accurately as possible, a time step discretization study was performed. Originally, the loads along the blade were recorded every 10° in azimuth and this was input into the acoustic solver. Time-step variations of 5°, 2°, and 1° were also analyzed to see the effect of the time-step on the OASPL.

Figure 5.10 shows the changes in OASPL as the time-step is decreased from 10° to 1°.

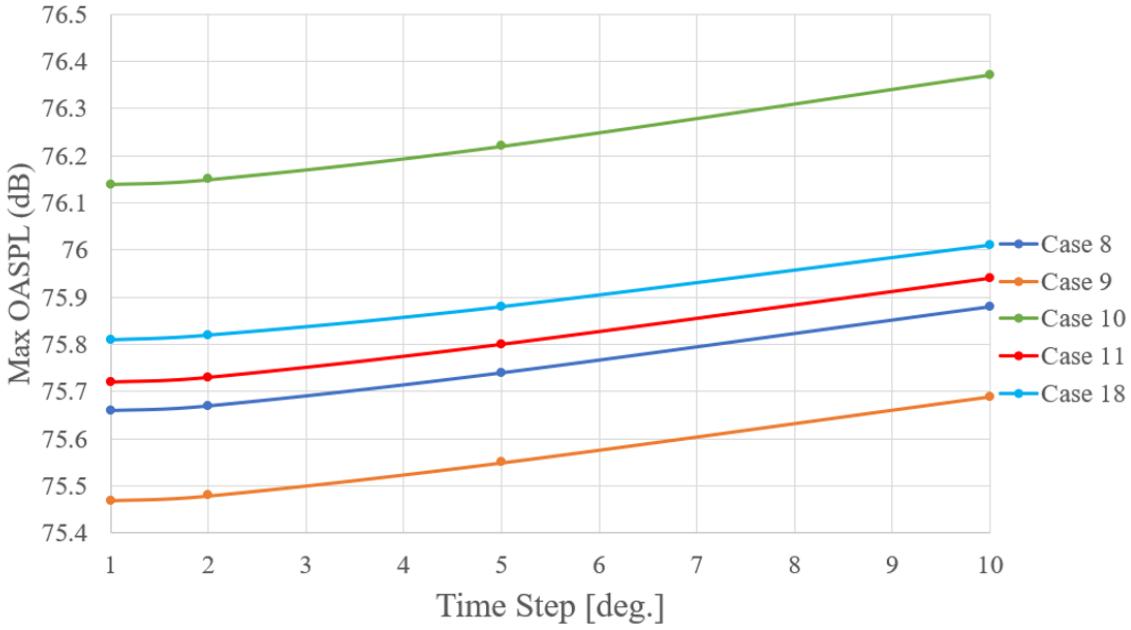

Figure 5.10: Time step discretization study for boom cases

It can be seen that the OASPL decreases as the time-step decreases, suggesting that the unsteady loads were not actually changing as much in time when the original 10° time step was used. A smaller time step was able to capture the smaller changes of the airloads in time, decreasing the OASPL by about 0.2 dB for all of the boom cases evaluated. From the 2° to 1° time step, the OASPL decreased by about 0.01 dB suggesting that the acoustic results converge when the time step is equivalent to 1°. There was not a substantial difference in the OASPL reported when using the original time step of 10°, but it is recommended to use a smaller time-step of 1° increments to acheive the most accurate results possible.

The OASPL was computed in dBA and is also reported in Table 5.4. Even though the aft-swept propeller boom case contains the largest noise, it does not result in the largest noise when A-weighting is factored in. In Figure 5.11, the decibel levels are shown at different frequencies for boom cases 8-11 at the azimuth location where the maximum OASPL was found to illustrate the trends of the A-weighting OASPL values.

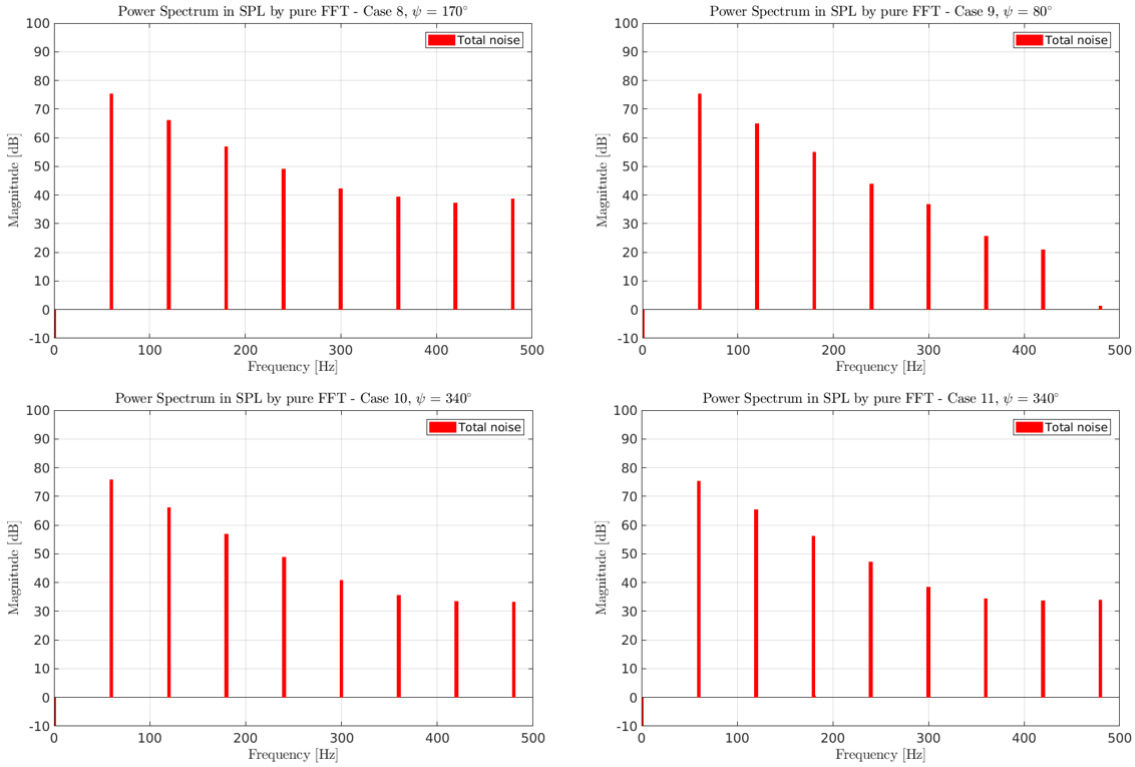

Figure 5.11: Cases 8-11 FFT analysis showing dB levels vs. frequency

Case 9 shows the least amount of noise since there are lower decibel levels at the higher frequencies. By looking at the FFT of Cases 8 and 11 it is hard to tell the difference in OASPL. This makes sense since the maximum OASPL is 75.88 dB and 75.94 dB respectively, which is a negligible difference. Case 11 has an almost 1

dBA improvement from Case 8 however. This is because Case 11 does not contain as much low frequency content which contributes more to the A-weighted OASPL. Case 18, whose FFT is not shown in Figure 5.11, has an A-weighted OASPL of 54.39 dBA, which is the highest out of all the boom cases. Even though Case 18 is not the loudest when measured in dB, it contains less low frequency content in the pressure signal, which causes the dBA value to be slightly higher than all the other cases.

Looking at Case 10, the loudest of the boom cases in dB, there is a 1 dB increase (as compared to Case 11) at the lower frequencies (60 Hz to about 360 Hz). This shows that when the OASPL is computed, the additional components at these frequencies contribute to the louder noise (in dB) computed for Case 10. This suggests that the aft-sweep of the blade actually results in an increase of noise at various frequencies contributing to the increase in OASPL. However, Case 10 is not as loud as Case 8 when looking at the A-weighted OASPL. Case 10 does not have as much high frequency content added, which does not effect the A-Weighted OASPL as much.

Therefore, the aft-swept propeller may be beneficial for the aerodynamic performance, but when it comes to the acoustics it is actually less effective if looking purely at dB. This is of no suprise since the same result was acheived for the isolated propeller cases since the aft swept propeller is a detriment to the noise due to the acoustic planform. However, if one is interested in the A-Weighted OASPL, the aft-swept propeller decreases the noise level, but only by about 0.3 dBA, which would be negligible by an observer. Since the aft-sweep only increases the OASPL by less

than 1 dB as compared to Case 8, it may be acceptable to use aft-sweep to increase aerodynamic performance and settle on the slight increase in noise depending on the specific design requirements.

These OASPL results are also shown in Figure 5.12 for an easier visual comparison of the dB and dBA levels.

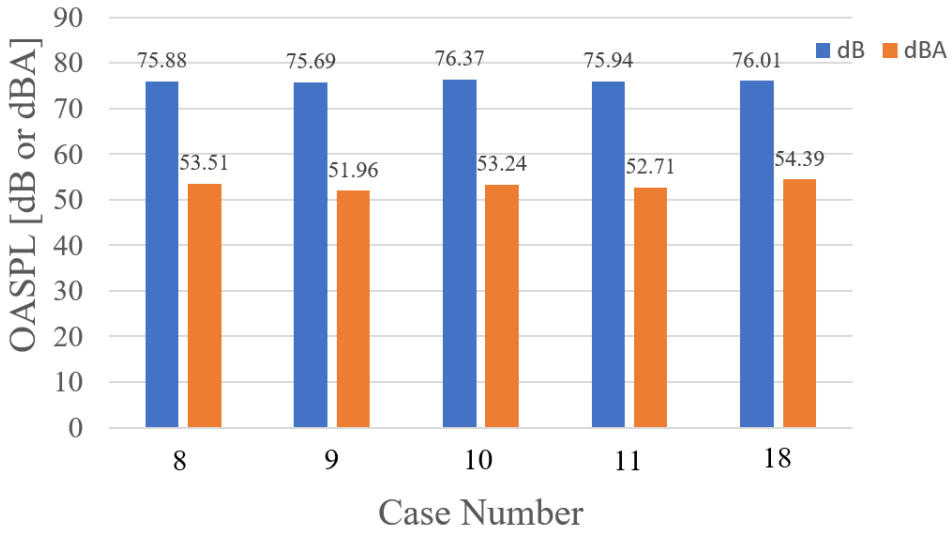

Figure 5.12: OASPL (dB & dBA) at 25° below the propeller for Cases 8-11 & 18

The aft-swept propeller contains the highest OASPL of 76.37 dB compared to the boom placed at the same distance with the baseline propeller at 75.88 dB. The boom is included in the Boeing/Aurora Flight Sciences eVTOL aircraft design, and looks to be placed 0.25R below, with the propeller canted. This means that the boom presence and propeller cant angle design results in a less than 1 dB increase in OASPL when comparing to the baseline case.

For completion, the OASPL was also computed when the boom cases were re-trimmed to factor in the downward force on the boom. The Figures of Merit

decreased slightly and in Table 5.5 it can be seen that the OASPL for each of the boom cases increased slightly by a negligible amount as expected. This shows that re-trimming the propeller resulted in a minimal aeroacoustic performance change.

Table 5.5: Cases 8-11 & 18 CFD OASPL (dB) Results Re-trimmed

Case	Original CFD OASPL (dB)	Re-trimmed CFD OASPL (dB)
8	75.88	75.90
9	75.69	75.70
10	76.37	76.39
11	75.94	75.97
18	76.01	76.05

Therefore, it is found that the boom itself, its location, or the type of boom does not significantly impact the aerodynamic or acoustic performance.

Since the loads of the boom itself were collected in GARFIELD, the acoustics of the boom itself was analyzed. Due to the unsteady loads on the boom, the SPL would be changing in time as well. However, the boom itself is not rotating, so the acoustics have to be examined for a stationary object. ACUM was built to accomodate for rotating objects, which becomes very important when factoring in the time delay of the sound waves actually reaching an observer. Two major assumptions were made when analyzing the acoustics of the boom itself: the tip Mach number and RPM of the boom were both set to as small as possible values to essentially equate to zero. In ACUM, the RPM & tip Mach number must be a number other than zero because the tip Mach number is used to find the free stream velocity and the RPM is used to find Δt, to eventually solve the FWH equation.

Both of these values cannot equal zero or the acoustic code will not be able to give values for the SPL's at various elevations. By setting the tip Mach number and RPM as close to zero as possible, the free stream velocity and rotation speed are set as close to zero as possible, which makes sense since the boom is in a hover condition and is not rotating. These assumptions were made when analyzing the same observer location elevations and the results for the boom cases are shown in Figure 5.13 below. It is noted in Chapter 6 that future work should be done to better analyze acoustics of stationary objects.

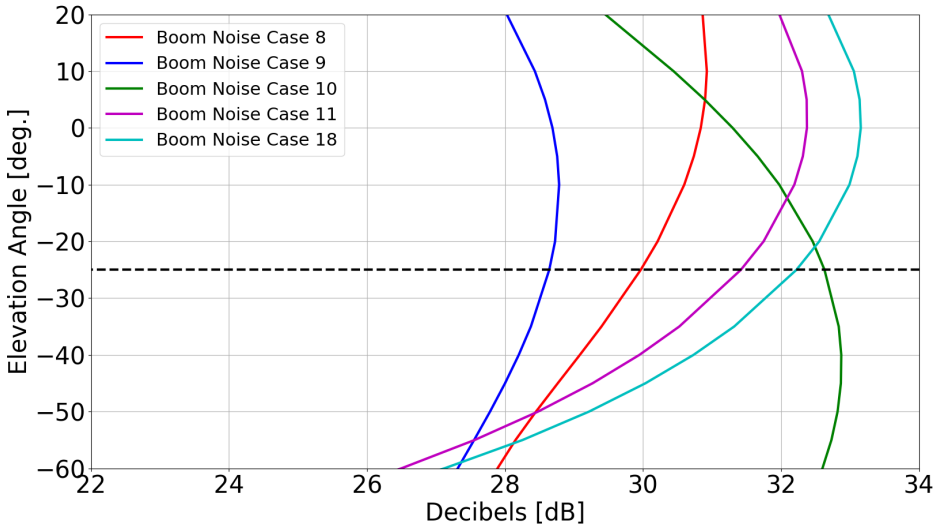

Figure 5.13: dB levels from the boom geometry itself as a function of elevation angle

The maximum SPL occurs at different elevations when analyzing the boom acoustics, but the 25° below the propeller is the primary point of interest. In order to understand how much noise the boom itself is contributing to an observer at that elevation of interest, the maximum SPL was measured at 25° below the propeller. These results are shown in Table 5.6 below.

Table 5.6: Cases 8-11 & 18 CFD SPL Results at -25° Elevation for Boom

Case 8	Case 9	Case 10	Case 11	Case 18
29.97 dB	28.64 dB	32.63 dB	31.42 dB	32.23 dB

The boom itself, when placed at the nominal vertical distance of 0.25R, contributes about 30 dB of noise. This makes sense since about 30 dB is equivalent to a quiet room setting or a whisper. It is quiet enough that the boom itself does not make much difference in the noise levels, but the boom still has some component added to the acoustics. When the boom is placed further away, the SPL decreases to 28.64 dB. Case 10 with the aft swept propeller contains the highest SPL of 32.63 dB. Case 11 contains a higher SPL than Case 8 and Case 9 of 31.42 dB, due most likely to the asymmetry of the boom, similarly to when the thickness and loading noise were analyzed solely from the propeller. Case 18 results in a SPL of 32.23 dB, only quieter than Case 10 with the aft propeller. All of these trends from the acoustics of the boom itself, match the trends when looking at the acoustics only from the propeller for these cases.

An FFT analysis was performed on the boom itself to see the results in the frequency domain. Figures 5.14 and 5.15 show the distribution of dB levels at various frequencies that make up the pressure time history signals of the forces experienced by the booms themselves. Case 8 shows more high frequency content than Case 9, thus making it louder, but Case 10 shows the most high frequency content, which makes sense since Case 10 was the loudest. However, it is noted that there is minimal high frequency content when looking at the boom itself for all of these cases.

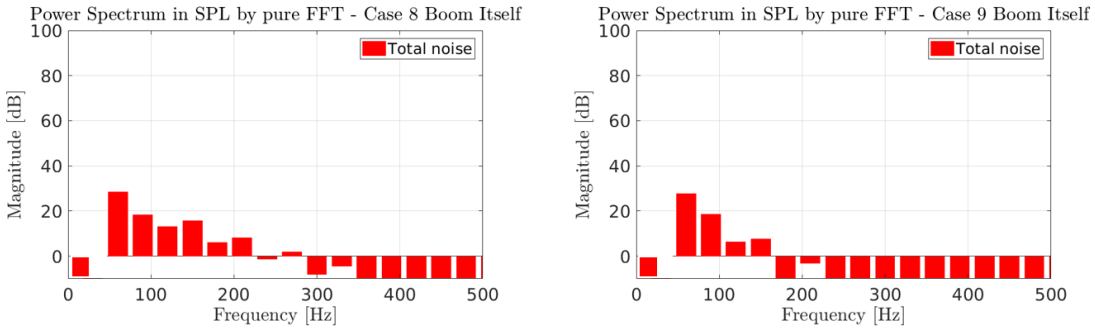

Figure 5.14: FFT results of Cases 8 and 9 of the boom itself

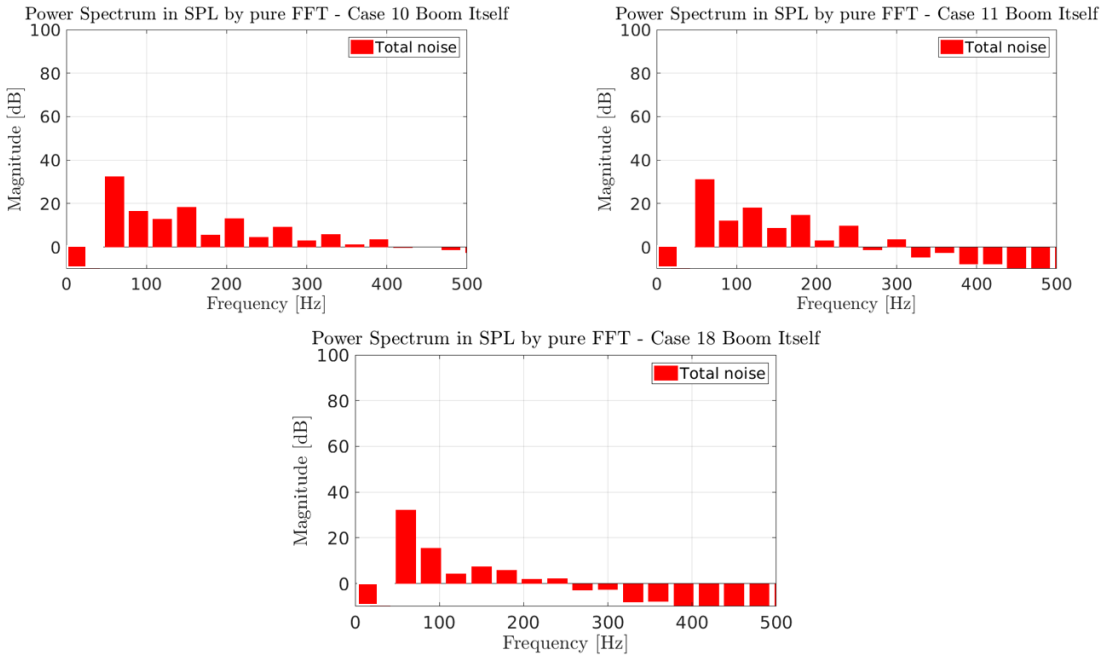

Figure 5.15: FFT results of Cases 10, 11, and 18 of the boom itself

Since 30 dB is low to the human ear, the boom's presence is even further proved to not be of a concern to the aeroacoustic performance of the eVTOL aircraft. It is more likely that an observer will hear the abundance of other louder noises in an urban environment than the noise coming from the boom itself added to the propeller noise.

Chapter 6: Conclusions and Future Work

6.1 Aeroacoustic Peformance of the Isolated Propeller

Between BEMT and CFD there were a lot of results to digest and analyze. A performance summary is shown in Figure 6.1 for the isolated propeller cases. This shows the trends captured by BEMT were similar to those achieved by CFD.

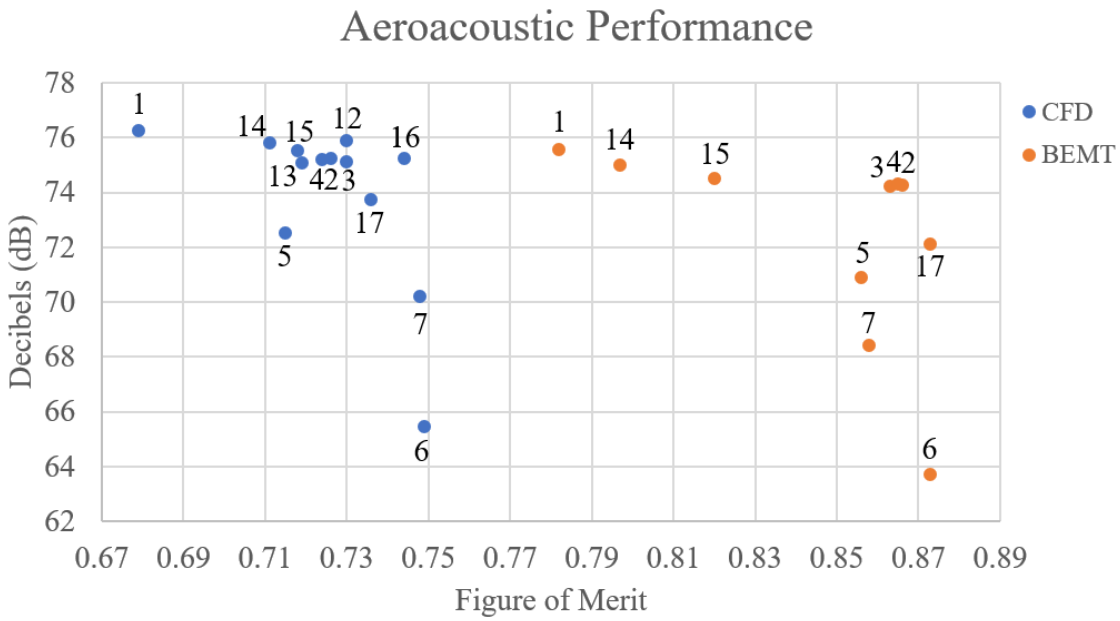

Figure 6.1: BEMT & CFD performance summary of the isolated propeller cases, Cases 1-7 & 12-17

It can be concluded that the ellipse planform provided an increase in Figure

of Merit as expected since a tapered blade will generally always have a beneficial effect on hover performance. When comparing the different twists with the ellipse planform it was unsurprisingly shown that changing the twist at the tip did not significantly affect the aerodynamic performance. When increasing the number of blades the Figure of Merit increased. With a higher blade count and a decrease in RPM, the Figure of Merit was further increased which was expected since the tip Mach number would be significantly less and result in lower power consumption. However, when the RPM was reduced, but the blade count was kept at two, the Figure of Merit decreased from the baseline case. When adding aft sweep, the propeller became more efficient while the forward sweep had the opposite effect. Transition modeling and decreased disk loading significantly increased the Figure of Merit.

Therefore, when purely looking at the aerodynamic performance for the isolated propeller, Case 6 (lower RPM and increased blade count) demonstrated the best hover performance in both BEMT and CFD analyses.

As far as the acoustics, the trends often agreed with the aerodynamic performance as seen in Figure 6.1. It is also noted that in general the best aerodynamic performance leads to the best acoustic performance. For the isolated propeller cases, Case 6, with three blades and at the lower RPM setting, was the most aerodynamically efficient and also proved to be the most acoustically efficient in both BEMT and CFD analyses. It is clearly shown that the acoustic performance is highly dependent on blade count and RPM, which both decrease the airloads thus decreasing noise levels. It was also shown that changing geometric parameters such as chord, twist,

radius, and sweep did not have a substantial impact on the acoustic performance, often only varying 1-2 dB between designs.

6.2 Aeroacoustic Performance of the Boom Cases

A performance summary is shown in Figure 6.2 for the boom cases. The aerodynamic performance was definitely affected when the boom was located underneath the propeller. Placing the boom further away (from 0.25R to 0.50R) resulted in an increase of Figure of Merit and should be placed as far away from the propeller as the eVTOL vehicle design allows.

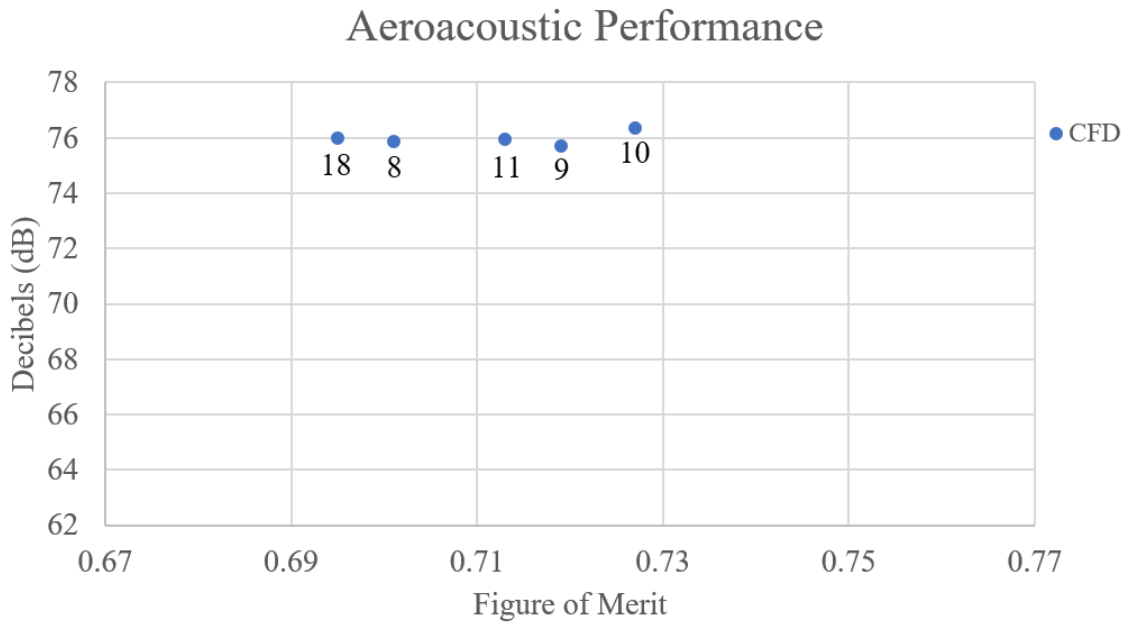

Figure 6.2: CFD performance summary of boom cases, Cases 8-11 & 18

The semi-infinite boom was not as detrimental to aerodynamic performance as the full boom at 0.25R, and the most efficient case was introducing aft-sweep to the

propeller. When the boom was canted at an angle, the Figure of Merit decreased very slightly compared to when the boom was placed parallel below the propeller.

However, when analyzing the propeller cases with a boom present, the noise levels did not vary much based on the vertical placement of the boom. Even when the boom was semi-infinite the noise increased by a negligible amount. The aft swept propeller increased aerodynamic performance, but it actually caused the loudest noise of the boom cases when looking at dB rather than dBA. With the boom canted, the noise increased by a negligible amount as well, all boom cases increasing the OASPL by less than 1.13 dB.

6.3 Conclusions

A successful computational aeroacoustic framework was created and implemented for various propeller configurations. Preliminary test cases were identified using BEMT and select propeller cases were chosen to be solved using CFD in the in-house, widely tested and trusted GARFIELD solver. Aerodynamic forces were taken from both BEMT and CFD to be evaluated in the FWH equation. Observer locations in a 50 meter radius hemisphere below the propeller were chosen and the sources of noise were computed as pressure fluctuations at each of these points. The OASPL was calculated using an FFT analysis to break down the dB levels into various frequencies to then be summed together. An A-weighting analysis was included to attempt to report noise levels that compensate for the relative loudness perceived by the human ear.

Various isolated propeller cases were run varying chord, twist, RPM, number of blades, sweep, radius, and transition modeling. A plausible boom geometry was then placed underneath the propeller at various distances to investigate the effect of nearby geometries and unsteady airloads on the noise. The propeller was then canted at an angle to observe its effects on the aeroacoustic performance. The primary conclusions drawn from this thesis are:

1. Design parameters such as twist and chord variation did not show a significant impact on the acoustic performance, even though a tapered, twisted blade improved the aerodynamic performance.

2. Design parameters such as RPM and number of blades were identified as the main drivers of imporving aeroacoustic performance. When these design parameters were used together the OASPL was decreased by about 10 dB.

3. Aft sweep significantly improves the aerodynamic performance, but increases OASPL due to its likely alignment with the acoustic planform. Forward sweep decreases aerodynamic performance, but offers less than 1 dB alleviation in the noise. Therefore, sweep is not a recommended design parameter to improve aeroacoustic performance.

4. Transition modeling significantly affected the aerodynamic performance of the propeller, but had a negligible impact on the acoustics due to the relatively small decrease in total noise from the reduction in drag noise.

5. Decreased disk loading or an increased radius propeller improved the aerodynamic performance and had a larger impact on the acoustic performance when compared to all other design parameters except for RPM and number of blades.

With a decrease of 2 dB, decreased disk loading has potential to improve the acoustic performance, but not as much as reducing the RPM or increasing the number of blades.

6. From the performance summary plot for the isolated propeller cases, an optimization technique can be derived using the BEMT results as a baseline of the predicted aeroacoustic performance. These preliminary results allow for thousands of test cases to be run, possibly applying a correction factor to predict the results that would be obtained by CFD. This would significantly minimize the amount of propeller cases needed to be run in CFD and would significantly reduce the amount of time analyzing various test cases in the preliminary design phase of these eVTOL vehicles.

7. A nearby boom geometry did not significantly impact the aerodynamic or acoustic performance. The aerodynamic performance increased the further away the boom was placed as expected. The asymmetry of the semi-infinite boom caused larger pressure fluctations and was louder than both full boom distances tested. However, the boom's presence, type of boom, and distance had negligible impacts on the acoustics to an observer (less than 1dB).

8. When the propellers were canted at an angle of 10°, the aeroacoustic performance decreased by a negligible amount. This can be a design chosen to provide more stability to the aircraft, as long as the slight decrease in Figure of Merit and slight increase in OASPL are acceptable.

6.4 Future Work

While this thesis provides a basis for analyzing propeller configurations and designs to understand how to optimize aeroacoustic performance, there is still much more to be investigated. RPM and the number of blades were the two major design parameters found to have the largest impact on noise and should be investigated further in the future. Further increasing the blade count from three blades and further reducing the RPM may result in an even more aeroacoustically efficient propeller. It would be useful to predict how the aeroacoustic performance increases when the number of blades increase, whether it is a linear or quadratic relationship. There may also be a limit to how high the number of blades can go before the acoustic or aerodynamic benefits level out. Therefore, in order to optimize the amount of noise being produced it is recommended to investigate propeller configurations with further increases in blade count that operate at a lower RPM.

Along these same lines, it is recommended to derive a specific optimization technique from the performance summary plot of the isolated propeller cases to be able to analyze thousands of test cases for aeroacoustic performance optimization. This would allow for quicker, more immediate feedback on the aeroacoustic performance of these propellers simply implementing a correction factor to predict the results that would be obtained by CFD. As stated above, this would significantly cut down on the time and computer resources needed in the preliminary design phases of these eVTOL vehicles. This thesis lays down the ground work in order to be able to derive further optimization techniques.

Even though the acoustics were analyzed from the boom itself, a non-rotating object, two key assumptions had to be made in order to make this possible. It is recommended to dive deeper into the acoustic code, ACUM, to be able to analyze stationary objects as well as rotating objects.

While the acoustics were analyzed for both the propellers themselves and the boom itself, it would be useful to have an acoustic analysis that accounts for both systems and computes the OASPL experienced by an observer due to both bodies together. The sources of noise may add or cancel and would be interesting to investigate. This would also be a step closer to analyzing the true aeroacoustics since objects on an eVTOL aircraft do not operate in isolation.

Since the boom and propeller were the only objects analyzed it is also reccommended to add in a plausible fuselage, and pusher propeller to integrate a full vehicle into the aeroacoustic framework. This would even further give the true aeroacoustics expected for an urban air-taxi transport vehicle.

All of these simulations were analyzed in hover, and it is recommended to further investigate the aeroacoustic performance of an eVTOL aircraft in forward flight. These vehicles will be operating in forward flight for longer than they operate in hover, so it is also important to see which design parameters affect the noise in forward flight. Additionally, analyzing the aeroacoustic performance during descent would be interesting as well. As an eVTOL vehicle approaches its destination while it is descending, it would be important to quantify OASPL's an observer would experience. An ideal scenario would be to identify design parameters that positively affect the aeroacoustic performance in hover, descent, and forward flight to optimize

the performance in multiple flight conditions.

Finally, it is recommended that experimental results be obtained or performed for an eVTOL aircraft in order to compare to the computational results analyzed in this thesis. A wind tunnel test or flight test would provide crucial experimental data to help further validate the computational results and would be very valuable in the preliminary design of these eVTOL vehicles.

This thesis proves that with the given tools above a computational aeroacoustic framework can be created to identify design parameters that affect aeroacoustic performance, which is of high interest to the urban-air taxi vertical flight community. There is still much more research to be done for an ideal optimization, but this thesis provides the groundwork for further investigation.

Bibliography

[1] Swartz, I. Kenneth, *Charging Forward, New eVTOL Concepts Advance* Vertiflite, July/August 2017.

[2] *Bell Nexus* Electric VTOL News, by the Vertical Flight Society, 2019.

[3] Loeffler, John *Boeing's Self-Flying Air Taxi Completes First Test Flight* January, 2019.

[4] *Fast-Forwarding to a Future of On-Demand Urban Air Transportation* Uber Elevate Whitepaper, October 27, 2016.

[5] Marte, E. Jack, and Kurtz, W. Donald, *A Review of Aerodynamic Noise From Propellers, Rotors, and Lift Fans* Jet Propulsion Laboratory, January 1970.

[6] Morgans A.S., Karabasov S.A, Dowling A.P., and Hynes T.P., *Transonic Helicopter Noise* AIAA Journal, Vol. 43, No.7 (2005), pp. 1512-1524.

[7] Brentner, S. Kenneth, Zolbayar, Bolor-Erdene, and Jaworski, F. Thomas, *An Investigation of Noise from Electric, Low-Tip-Speed Aircraft Propellers* American Helicopter Society, San Francisco, CA, January 16-19, 2018.

[8] Hubbard, H. Harvey, *Aeroacoustics of Flight Vehicles: Theory and Practice* Vol. 1 (1991), Chapters 1-2.

[9] Vogeley, A. W., *Sound Level Measurements of a Light Airplane Modified to Reduce Noise Reaching the Ground* NACA Report 926, Langley Field, VA, February 1948.

[10] Petrucci, Mike, *Lockheed YO-3A Quiet Star: The Original Stealth Aircraft of the Vietnam War* August, 2014.

[11] Jude, Dylan and Baeder, James *Extending a Three-Dimensional GPU RANS Solver for Unsteady Grid Motion and Free-Wake Coupling* AIAA Scitech, 2016.

[12] Leishman, J. G., *Principles of Helicopter Aerodynamics* Cambridge University Press, New York, NY, 2000, Chapter 3.

[13] Houser, S. Dorian et al., *A Review of the History, Development and Application of Auditory Weighting Functions in Humans and Marine Mammals* The Journal of the Acoustical Society of America, March 2, 2017.

[14] Gallman, M. Judith, *The Validation and Application of a Rotor Acoustic Prediction Computer Program* U.S. Army Aeroflightdynamics Directorate, NASA Ames Research Center, Moffett Field, California, June 4, 1990.